Electrochemistry Under Confinement:
Controlling Dynamics in Nanochannels via Tunable Mass Transport

Marissa Wood

A dissertation
submitted in partial fulfillment of the
requirements for the degree of

Doctor of Philosophy

University of Washington
2014

Reading Committee:
Bo Zhang, Chair
Daniel R. Gamelin
Christine K. Luscombe

Program Authorized to Offer Degree:
Chemistry

University of Washington

Abstract

Electrochemistry Under Confinement:
Controlling Dynamics in Nanochannels via Tunable Mass Transport

Marissa Wood

Chair of the Supervisory Committee:
Associate Professor Bo Zhang
Department of Chemistry

This dissertation explores the intersection of electrochemistry and transport dynamics under confinement using electroanalytical techniques to both probe and control transport behavior. We first present a unique wireless method for *in situ* control of single metal nanowire growth in a silica nanochannel template. Growth is initiated by direct chemical reduction of metal precursor ions and proceeds until the channel diameter is blocked. Further deposition occurs by a bipolar electrochemical mechanism, in which oxidation at one end of the wire is directly coupled to reduction at the other. The deposition rate can be precisely controlled without a direct electrical connection by applying an electric field during the growth process, offering an unprecedented level of synthetic tunability.

Next, we report a comprehensive study of anomalous size- and material-dependent selectivity observed in the transport of polystyrene and silica nanoparticles through a silica nanochannel as detected by resistive-pulse sensing. We investigated several possible contributing factors, including basic driving forces and more subtle nanoscale effects, finding that selectivity occurs outside the channel and may be a result of dynamical charge effects related to interfacial structure or particle polarizability. Our results suggest that nanoscale effects can have a dramatic impact on more macroscale transport behavior when the size of the analyte approaches the size of the channel, which has important implications for both understanding and designing nanoporous systems.

We then discuss two new methods for the fabrication of individual gold nanoelectrodes based on reported nanowire synthesis techniques (nanoskiving and lithographically patterned nanowire electrodeposition (LPNE)) and conclude by summarizing efforts to prepare uniform gold nanowire arrays for use in electrochemical sensing and imaging studies.

This work reflects the complicated interplay of driving forces inherent in nanoscale systems and demonstrates the exciting potential for harnessing them in a concerted manner to precisely control transport dynamics. Gaining a better understanding of these interactions and determining the relative roles of intrinsic material properties and experimental factors will not only provide the framework necessary to investigate and interpret other fundamental nanoscale processes, but will also enable the design and synthesis of nanomaterials with more tailored and customizable properties for use in catalysis, sensing, and energy applications.

Acknowledgments

There are many people who have helped and supported me throughout this journey. I would first like to thank my advisor, Bo Zhang, for allowing me to work in his lab and pursue my own research ideas, and my committee members for their input and guidance. I am grateful for all of my friends and colleagues in the UW Chemistry Department who have supported me in countless ways and have greatly enriched my graduate school experience. I would also like to thank my family and friends for their constant support and encouragement—my dad for his example in this field and his continual pursuit of knowledge, and especially my brother, Brandon, for his many insightful discussions and for believing in my research when no one else did. Finally, thank you to NPR and the hosts of KUOW for entertaining me and keeping me company during many long nights in the lab.

Contents

List of Figures

List of Tables

CHAPTER 1

Introduction

> *"Indeed, it is the great beauty of our science, Chemistry, that advancement in it, whether in a degree great or small, instead of exhausting the subjects of research, opens the doors to further and more abundant knowledge, overflowing with beauty and utility, to those who will be at the easy personal pains of undertaking its experimental investigation."*
>
> — Michael Faraday, *Researches in Electricity*, (1834)

THE PAST two centuries have seen remarkable advances in the understanding of chemical and electrical processes, facilitating widespread industrialization and rapid technological innovation. As a result, electrochemistry has emerged as an important area of interdisciplinary investigation, exploring the relationship between chemical reactions and the flow of electricity. This connection was first articulated by Michael Faraday in the first half of the 19th century. Since then, significant progress has led to the development of batteries, fuel cells, and electroplating techniques, demonstrating the phenomenal utility of chemical and electrical energy interconversion.

Recently, there has been a renewed interest in electrochemistry, fueled by the current comprehensive focus on nanoscale discovery, synthesis, and characterization. Electrochemical characterization techniques are particularly well-suited for studying nanoscale phenomena, as they provide valuable information about surface structure, reaction kinetics, thermodynamics, and analyte properties. The success of these techniques for nanoscale analysis can be primarily attributed to improvements in fabrication and instrumentation. In particular, the development of micro- and nanoscale electrodes (known as ultramicroelectrodes, UMEs) has dramatically increased the temporal and spatial resolution of electrochemical measurements, broadening the scope, capabilities, and applications of electrochemical investigations.

Several versatile characterization techniques have enabled the use of these small probes for a diverse range of studies. For example, scanning electrochemical microscopy (SECM) monitors the current between a metal tip and a substrate as it is scanned over the surface, while cyclic voltammetry and amperometry measure the current at an electrode as the potential is either held constant or cycled. All three provide detailed information about the surrounding environment. Consequently, UMEs have been employed as localized probes for the precise analysis of surface reactivity and topography,[1–4] electron-transfer kinetics,[5–8] and catalytic properties.[9–14] Likewise, carbon fiber UMEs have been employed to investigate the kinetics and spatial activity of neurotransmitter release in neuronal cells,[4,15–18] and nanoelectrodes and nanoelectrode arrays have been integrated into sensors and devices for the detection of a wide variety of analytes, including biomolecules,[19–21] drug molecules,[22] and metal contaminants.[23] In addition, electrodes with diameters under 10 nm (sometimes referred to as nanodes) have been used for more fundamental studies on unique interfacial double layer effects.[7,24–28]

Other electroanalytical techniques rely on the measurement of the ionic current through a small nanopore rather than the faradaic current at an electrode surface. Scanning ion-conductance microscopy (SICM) records the ion conductance through a pore in a probe tip, enabling the characterization of sample morphology.[29] The non-destructive nature of this technique allows it to be used with living cells and other biological samples.[30–32] Resistive-pulse sensing (based on the Coulter counter principle) detects analytes as they pass through a channel by measuring corresponding decreases in the ionic current through the channel and has been used to detect and characterize nanoparticles, biomolecules, and viruses on the basis of size[33–37] and charge.[33,38–42] This widely-used method requires no labeling and provides accurate information about each individual particle rather than ensemble averages. In addition to these electrochemical sensing and characterization applications, nanoscale electrochemistry has also been leveraged to achieve controlled fabrication of metal nanowires by electrochemical deposition[43–46] or direct electrochemical reduction[47–50] of metal precursor ions in nanotemplates.

As electrochemical measurements become more spatially confined, transport behavior becomes increasingly important. This is evidenced by the many unusual and counterintuitive transport phenomena that have been reported in nanochannels.[51–53] For example, selective transport of cations and enhanced ion and water transport rates have been observed in carbon nanotubes and other molecular-scale nanochannels.[54–60] Similarly, overlap of charged electrical double layers (localized regions of ion accumulation near the walls) in the interior of these tiny channels can lead to selective transport of counterions under an electric field, resulting in ion depletion and enrichment regions on opposite sides of the channel.[61] This effect, known as concentration polarization, has been used to preconcentrate analytes in order to achieve lower detection limits,[62–66] and similar selective ion transport effects have been exploited for applications such as molecular gating,[67,68] nanoscale diodes,[69,70] and nanofluidic transistors.[71–73] The interplay between electrokinetic and hydrodynamic phenomena has also been shown to dramatically change the transport mobility of particles in nanochannels.[74,75] Similarly, interfacial interactions between analytes, solvent molecules, electrolyte ions, and nanochannel walls are capable of influencing transport behavior through a variety of mechanisms, including friction forces,[76,77] electrostatic factors,[33,34,78,79] chemical attractions,[75,80–82] and hydrophobic interactions.[83–87]

Since electrochemistry and transport mechanics are interdependent, particularly at these small length scales, combining the knowledge from these two fields generates a powerful set of tools that can be adjusted and tuned to cooperatively control nanoscale properties and behavior. The impressive capabilities and widespread applications of nanoscale electrochemistry ensure the continued importance and relevance of this field in the future and reflect the potential for considerable progress in many different areas of nanofabrication, characterization, and analysis. In the remainder of the introduction we will discuss basic principles and characterization techniques pertaining to nanoscale electrochemistry before exploring fundamental concepts governing micro- and nanofluidic transport.

1.1 Fundamentals of Nanoscale Electrochemistry

This section presents fundamental principles of electrochemical behavior and measurement, highlighting the advantages of using UMEs for electrochemical analysis and describing typical electrochemical characterization techniques. We begin our discussion with an overview of the electrical double layer.

1.1.1 Electrical Double Layer

Electrochemical measurements are often affected by the presence of an electrical double layer at charged solid/liquid interfaces. Therefore, a description of the electrical double layer and its basic structure is given here. Most surfaces acquire a net surface charge in solution due to ionization of surface groups or specifically adsorbed ions on the surface. When a charged surface is in contact with an electrolyte solution, the adjacent ions will arrange themselves so as to screen the charge and maintain global electroneutrality. This thin layer of counterions and coions distributed near the surface is called the electrical double layer (EDL) and acts as a capacitor. There have been several different models of the EDL proposed over the years, each varying in complexity, from a simple capacitor with a single layer of counterions at the surface (Helmholtz model) to a more diffuse model of counterions and coions (Gouy-Chapman model), to a combination of the two that takes into account the solvation shells of the ions (Gouy-Chapman-Stern model). Although more sophisticated mathematical models have been suggested, the brief mathematical description of the EDL potential given below is based on this last model, which is a relatively good predictor of EDL behavior. A diagram of the EDL formed at a negatively charged surface is shown in Figure 1-1.

The first layer consists of solvent molecules and, occasionally, anions that are specifically adsorbed to the surface. The imaginary plane intersecting the center of these ions parallel to the surface is known as the inner Helmholtz plane. The next layer contains counterions that

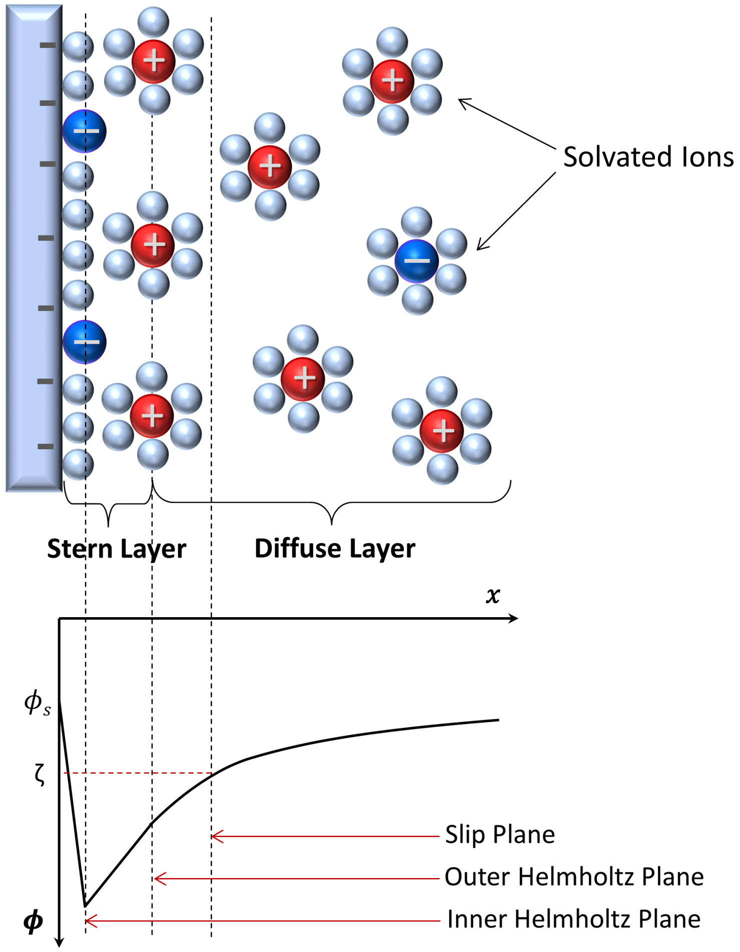

FIGURE 1-1: a) Diagram of the electrical double layer near a negatively charged surface of potential ϕ_s. The first layer consists of specifically adsorbed anions and solvent molecules, and the imaginary plane crossing through their centers is known as the inner Helmholtz plane. The next layer contains solvated counterions, with the closest distance between the center of a solvated ion and the surface defined as the outer Helmholtz plane. The area between these two planes is known as the Stern layer, and the region beyond this consists of counterions and coions that extend into the bulk solution and neutralize the remainder of the charge (diffuse layer). Ions in the Stern layer are effectively attached to the surface and will move along with it in solution, whereas those outside this layer will not. The boundary between these two regions is defined as the slip plane, and the potential at this plane is known as the zeta potential ζ, which can be experimentally measured. b) Potential distribution in the different regions according to the Gouy-Chapman-Stern model. Figure based on Ref. 52.

are partially and fully solvated, with an outer boundary (the outer Helmholtz plane) defined by the minimum possible distance of approach between the center of a fully hydrated ion and the surface. This region closest to the surface, between the inner and outer Helmholtz planes, is known as the Stern layer, and the interactions in this zone are strong enough to effectively bind the ions to the surface, preventing them from moving independently in solution. The potential in this area decreases linearly with increasing distance from the surface. The region outside the Stern layer is known as the diffuse layer and contains counterions and coions that extend into the bulk solution until the charge is neutralized. These ions have weaker electrostatic interactions with the surface and are able to move separately in solution. Therefore, the structure in this region is based on the balance between electrostatic interactions and thermal diffusion.[52,88] The potential decay throughout the diffuse layer is described well by the Gouy-Chapman model and is given by the Poisson-Boltzmann equation, which takes into account the ion distribution represented by the Boltzmann distribution and the electric potential gradient defined by the Poisson equation:[52]

$$\nabla^2 \psi = \frac{d^2\phi}{dz^2} = \frac{e}{\varepsilon_0 \varepsilon} \sum_i n_i^\infty z_i \exp\left(-\frac{z_i e \phi(z)}{k_B T}\right) \tag{1.1}$$

where e is the charge of an electron, ε_0 is the permittivity of free space, ε is the dielectric constant of the solvent, n_i^∞ is the bulk concentration of the ion, z_i is the valency of the ion, k_B is the Boltzmann constant, and T is the absolute temperature. For a symmetrical electrolyte, this equation simplifies to:[88]

$$\frac{d^2\phi}{dz^2} = -\left(\frac{8k_B T n^\infty}{\varepsilon_0 \varepsilon}\right)^{1/2} \sin h\left(\frac{ze\phi}{2k_B T}\right) \tag{1.2}$$

The interface between the immobile Stern layer and the mobile diffuse layer is known as the slip plane, and the potential at this plane is referred to as the zeta potential ζ. The characteristic thickness of the EDL is called the Debye length λ_D and represents the electrostatic screening length. While it will differ depending on the properties of the electrolyte, it can be determined from the following equation:[61]

$$\lambda_D = \sqrt{\frac{\varepsilon_0 \varepsilon k_B T}{e^2 \sum_{i=1}^{2} z_i^2 n_i^\infty}} \tag{1.3}$$

For aqueous solutions containing a symmetrical 1:1 electrolyte, it can be simplified further:[89]

$$\lambda_D(nm) = 0.3M^{-1} \tag{1.4}$$

where M is the ionic strength. Therefore, the Debye length decreases as the electrolyte concentration increases, and in aqueous solutions it is generally only a few nanometers thick.

The electrical double layer is extremely important in predicting and interpreting both electrochemical and mass transport behavior in aqueous solutions. In fact, there are several transport phenomena, known collectively as electrokinetic effects, that arise from EDL properties and involve the movement of charged species near charged interfaces.[61] These effects become increasingly significant in micro- and nanochannels due to the increased surface-area-to-volume ratio. The four main effects include electroosmosis, electrophoresis, streaming potential, and sedimentation potential. The first two involve movement in response to an electric field and are the most relevant for our discussions here, while the second two describe the opposite—generation of an electric field due to movement. Each of these will be commented on in more detail in the section on transport dynamics.

1.1.2 Unique Characteristics of UMEs

This section describes some of the unique properties of UMEs that make them valuable and versatile tools for electroanalysis. We begin our discussion by considering a typical experimental setup for collecting electrochemical data. Traditional electrochemical measurements are carried out using a three-electrode cell consisting of a working electrode (where the reaction of interest takes place), a reference electrode, and a counter electrode. The potential of the working electrode is measured relative to a reference electrode of known potential, while the counter electrode passes the current needed to balance the electrochemical processes occurring at the working electrode. Using the counter electrode to balance this current rather than the reference electrode prevents the potential of the reference electrode from changing. An electrolyte is usually added to the solution to carry the charge and prevent electromigration of other ionized species. The system is typically controlled using an instrument known as a potentiostat, which also records the resulting current. The potentiostat functions by applying current to the working electrode in the amount necessary to achieve the desired set potential between the working electrode and the reference electrode, and it is this current that is measured, representing the electrochemical reaction rate.[88]

However, if the working electrode is a UME, a two-electrode cell consisting only of a working electrode and a reference electrode can be used instead, significantly simplifying the setup. The reason for this is twofold. First, the small electroactive surface area results in a very small current at the working electrode, meaning that the corresponding current passing through the reference electrode is small enough to prevent any significant potential change, eliminating the need for a counter electrode. Second, as a result of these small current values, the potential drop (iR drop) across the solution is negligible. Consequently, experiments can be performed in solutions of low conductivity or nonaqueous solvents, increasing the measurement versatility.[88,90]

Another benefit of using UMEs is related to the double layer charging time, given by R_sC_{DL}, where R_s is the solution resistance and C_{DL} is the double layer capacitance. The double layer capacitance decreases as the electrode size is reduced, thereby lowering the dou-

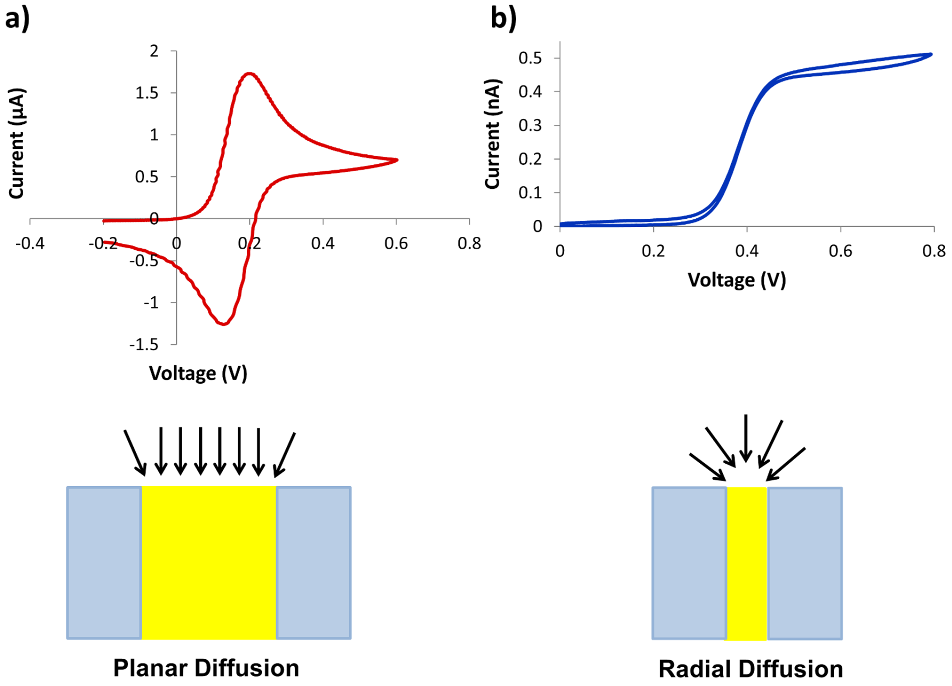

FIGURE 1-2: Comparison of the diffusion profiles and corresponding cyclic voltammograms for a conventional 1-mm-diameter gold electrode (a) and a 216-nm-diameter gold UME (b). While diffusion to a conventional electrode is mostly planar, diffusion to a UME is radial, resulting in faster mass transport. Consequently, the current reaches a steady-state value, giving a sigmoidal-shaped voltammogram rather than the traditional peak-shaped voltammogram. CVs were taken in 1 mM ferrocenemethanol in 0.1 M KCl at a scan rate of 50 mV/s (a) and 5 mM ferrocene in 0.1 M TBAPF$_6$ at a scan rate of 20 mV/s (b).

ble layer charging time. This allows the measurement of electrochemical reactions on ultrafast time scales. Indeed several groups have used nanoelectrodes to investigate fast electron transfer kinetics and detect transient intermediate species.[5,6,91–94]

One of the primary advantages of using UMEs for electrochemical measurements is the significantly enhanced mass transport of redox species to the electrode surface due to radial diffusion. The diffusion profiles for a conventional millimeter-sized electrode and a UME are compared in Figure 1-2. For the conventional electrode, diffusion is planar, with radial diffusion at the edges contributing only a small amount to the total. Conversely, diffusion to a UME is dominated by radial diffusion. Consequently, the concentration of redox species at the surface is never depleted because it is easily replenished by drawing from the surrounding solution radially in all directions. As a result, mass transport to and from the electrode surface is faster, and the current reaches a diffusion-limited steady-state value that is independent of time. This behavior enables the measurement of reaction kinetics and EDL effects on faster time scales.

Finally, due to their small size, UMEs only require small solution volumes for analysis and can be used to detect very low numbers of molecules. Decreasing the electroactive surface area lowers the background charging current, raising the signal-to-noise ratio to an acceptable level for the measurement of very small currents. This is beneficial for applications in a wide range of fields, including single-molecule detection experiments and electrochemical sensors.

1.1.3 Characterization Techniques

Although there are many techniques to measure and evaluate electrochemical reactions, they can be divided into two main categories: potentiometric and voltammetric methods. Potentiometric methods measure the potential between a working electrode and a reference electrode, often as the current is held constant, and these techniques are particularly good for investigating background processes. Conversely, voltammetric methods measure the current at the working electrode as the potential is controlled, providing information about the identity and concentration of redox species in solution as well as their characteristic redox potentials.[88,90]

Voltammetry

Voltammetry involves changing the applied potential according to a particular pattern (i.e. linearly, stepped, or pulsed) at a constant rate while measuring the corresponding current. In cyclic voltammetry, one of the most common techniques, the potential is increased linearly at a constant rate until it reaches a certain value and then decreased back to the starting potential, with current plotted as a function of potential. Figure 1-2a shows a typical cyclic voltammogram (CV) of a 1-mm-diameter gold electrode in a solution of 1 mM ferrocenemethanol in 0.1 M KCl. At the appropriate potential, the redox molecules at the electrode surface are oxidized or reduced, leading to an increase in faradaic current that produces a peak. The peak current i_p for a reversible redox process is given by the Randles-Sevcik equation:[88]

$$i_p = 0.4463 \left(\frac{F^3}{RT} \right)^{1/2} n^{3/2} A D^{1/2} C^* \nu^{1/2} \tag{1.5}$$

where F is Faraday's constant, R is the universal gas constant, T is the absolute temperature, n is the number of electrons transferred per redox molecule, A is the electrode area, D is the diffusion coefficient of the redox species, C^* is the bulk concentration of the redox species, and ν is the scan rate. Therefore, since the current response is dependent on the electroactive surface area, this technique can be used to characterize the geometry of the electrode. Likewise, the magnitude of the peak current can also be used to calculate the concentration or diffusion coefficient of the redox species, while the potential of the peak gives information about the identity and thermodynamic favorability of a reaction.

The shape of the CV is dependent on the diffusion of the redox species to the electrode surface and changes significantly when UMEs are used. As discussed previously, diffusion to a UME is radial, which increases the mass transport of redox species to the electrode surface and results in steady-state behavior. Consequently, the resulting CV is sigmoidal-shaped like the one shown in Figure 1-2 for a 216-nm-diameter gold nanoelectrode in 5 mM ferrocene. The steady-state limiting current i_{ss} at an ultramicroelectrode is given by[88]

$$i_{ss} = 4nFDC^{*}r \tag{1.6}$$

where r is the electrode radius.

Cyclic voltammetry is incredibly useful for characterizing both the redox species in solution and the electrode geometry and accounts for much of the electrochemical characterization performed in this dissertation.

Chronoamperometry

Important information can also be gained from studying how the current varies with time at a constant potential. This technique, known as chronoamperometry, is particularly useful for measuring time-dependent processes, such as exocytosis of vesicle contents from neuronal cells,[4,15–18,95] catalytic events resulting from nanoparticles hitting an electrode surface,[11–14] or detection and characterization of nanoparticles passing through a nanopore by resistive-pulse sensing.[33,96–98] One advantage of chronoamperometry is that the potential can be held at a value specific to the redox potential of the analyte, helping to eliminate unwanted redox reactions from other species in solution, as may occur with cyclic voltammetry.

Chronocoulometry

In a related technique called chronocoulometry, the integrated current, or amount of charge passed, is measured as a function of time. This offers certain benefits, including less signal noise due to the integration, as well as the ability to distinguish between charging current and the current due to redox reactions of electroactive species.[88]

1.2 Transport Dynamics at the Nanoscale

Microfluidic and nanofluidic systems often involve the combination of multiple transport modes, presenting a substantial challenge for predicting transport behavior. However, the interplay between these forces and the transport limitations imposed at small length scales gives rise to interesting phenomena that can be manipulated to provide precise control over solution/solute dynamics and reaction rates. In this section, we present a general overview of the important concepts and equations governing fluid mechanics on the micro- and nanoscale.

1.2.1 Equations Governing Transport

We begin our discussion by considering the three central equations that describe micro- and nanofluidic transport of charged species in nanochannels: the Nernst-Planck equation for the transport of charged species, the Navier-Stokes equation for fluid flow, and the Poisson equation for the potential distribution in the channel. Each is discussed briefly below.

Nernst-Planck Equation

The Nernst-Planck equation describes the transport of charged species through a channel under the influence of an electric potential, with the flux per area J_i of ion i given by[52]

$$J_i = -D_i \nabla c_i - \frac{z_i F}{RT} D_i c_i \nabla \phi \pm v_c c_i \tag{1.7}$$

where D_i is the diffusion coefficient of the redox species, c_i is the concentration of the redox species, z_i is the valency of the ion, F is Faraday's constant, R is the universal gas constant, T is the absolute temperature, ϕ is the electric potential, and v_c is the convective velocity field. This equation is simply the sum of the flux contributions from three different sources: diffusion due to a chemical gradient (Fick's first law), electric potential, and convection (solvent flow due to pressure, electric or magnetic fields, stirring, etc.).

Navier-Stokes Equations

The Navier-Stokes equations are derived from the conservation of momentum and describe incompressible fluid flow in nanochannels as follows:[52]

$$\nabla v_c = 0 \tag{1.8}$$

$$-\nabla p - F_b \sum_{i=1}^{2} z_i c_i \nabla \phi - F_b \sum_{i=1}^{2} z_i c_i \nabla \varphi + \eta \nabla^2 v_c = 0 \tag{1.9}$$

where p is the external pressure, F_b is the body force, φ is the streaming potential, and η is the viscosity of the solution. Equation 1.8 is the continuity equation related to the conservation of mass, mathematically expressing that the volumetric rate at which mass enters the channel is equal to the rate at which it exits. Equation 1.9 is a statement of the total forces acting on the fluid in both directions. The first three terms are forces due to the pressure gradient, polarization of the electrical double layer (caused by the concentration gradient), and the streaming potential (resulting in electroosmotic flow). These three terms are balanced by the fourth term, which has the opposite sign and represents the viscous drag force in the reverse direction. This equation can therefore be used to calculate the v_c term in the Nernst-Planck equation above.

Poisson Equation

The Poisson equation describes the electric potential distribution in the nanochannel:[52]

$$\nabla^2 \phi = -\frac{F}{\varepsilon_0 \varepsilon} \sum_{i=1}^{2} z_i c_i \tag{1.10}$$

Although the general forms for each of these equations have been given, a complete combined solution is challenging and is beyond the scope of this dissertation. However, the relevant transport mechanisms and effects related to these three descriptions as well as the pertinent equations derived from them will be introduced in the following sections.

1.2.2 Transport Mechanisms

Transport of ions and other charged solutes in aqueous solutions can occur by three main mechanisms, each associated with a unique driving force. Diffusion, convection, and migration are movements of the solute in response to a concentration gradient, solvent flow, or electric potential, respectively. While diffusion and convection affect all solutes, irrespective of size or composition, migration affects only charged solutes. Convection is unique because it relies on the movement of the solvent to carry the solute along, while the other two methods of transport involve the solute traveling through the solvent. Due to this distinction, convection is uniquely dependent on the geometry of the channel occupied by the fluid, while the other two modes of transport are, on the simplest level, independent of this relationship. Before examining each mechanism in detail, we will first briefly consider basic principles and properties of fluid flow that are relevant for our discussion, focusing on flow through cylindrical channels since this geometry was used in the work presented here.

Fluid Flow and the Stokes Equation

Fluid flow patterns can be characterized by the ratio of inertial forces to viscous forces. The relative importance of these two forces is given by the Reynolds number R_e:[90]

$$R_e = \frac{\rho v L}{\eta} \tag{1.11}$$

where ρ is the fluid density, v is the fluid velocity, L is the characteristic length scale of the flow (i.e. channel diameter for flow in a cylindrical channel), and η is the dynamic viscosity of the solvent. Flow situations with identical Reynolds numbers will have similar flow patterns even if they are on completely different length scales, making it a useful predictive value. When $R_e \ll 1$, viscous effects are dominant, and incompressible fluid flow in a cylindrical channel is fully laminar, comprising a series of concentric fluid layers that slide past one another at different velocities. Consequently, the velocity profile is parabolic (shown in

Figure 1-3, with the fastest flow in the center of the channel and no flow at the walls due to friction. At $R_e \gg 1$, inertial effects are dominant, leading to turbulent flow, which displays behavior that is much more difficult to predict. However, in general, Reynolds numbers less than 1500 signify relatively laminar flow, while numbers above 2500 indicate turbulent flow, and values between 1500 and 2500 correspond to transitional flow behavior.[90,99]

The stable flow occurring at the lower extreme of $R_e = 0$ (when no inertial forces are present) is known as Stokes flow or creeping flow. Under these conditions, the inertial forces in the Navier-Stokes equation can be ignored, enabling a substantial simplification known as the Stokes equation:[100]

$$\nabla p = \frac{pL}{v}\nabla v = \eta \nabla v \tag{1.12}$$

The Stokes equation can be solved exactly for many different channel geometries and can be applied to flow in microfluidic and nanofluidic channels, since Reynolds numbers are typically small (<1) in these situations.

1.2.3 Diffusion

Molecular diffusion is caused by the random forces exerted on a particle or ion by the surrounding liquid molecules (under Brownian motion). As a result, a particle will tend to move from an area of higher concentration to an area of lower concentration, with the driving force provided by the resulting entropy increase.[61,101] Diffusion is often described in terms of concentration gradients, with the diffusive flux J (the number of particles moving through a cross-sectional area per unit time) defined by Fick's first law:[61,88]

$$J = -D\frac{dc}{dx} \tag{1.13}$$

where c is the concentration of the species. The diffusion coefficient can be described as a proportionality constant representing the size and frequency of the displacement resulting from collisions with neighboring fluid molecules. It will therefore strongly depend on the size, shape, and molecular weight of the diffusing species, as well as the properties of the solvent and the temperature of the system. The value of D is related to the root-mean-square displacement $\langle x \rangle$ at time t by[88]

$$\langle x \rangle = (2Dt)^{1/2} \tag{1.14}$$

This equation can be used to estimate how far a species in solution will diffuse in a certain period of time if the diffusion coefficient is known, or it can be used to calculate the diffusion coefficient by measuring the distance it has traveled after a period of time. The values of most molecular diffusion coefficients are determined experimentally. However, when the diffusing species is much larger (like a particle), it can be approximated as a small sphere moving through a viscous fluid, and its diffusion coefficient can be calculated exactly. At low Reynolds numbers when flow can be described as Stokes flow, the force f acting on the sphere under the influence of only viscous drag is given by[101]

$$f = 6\pi\eta Rv \tag{1.15}$$

where η is the fluid viscosity, R is the radius of the sphere, and v is the fluid velocity. The forces acting on the sphere under diffusion are a combination of the random forces exerted on the particle from the fluid molecules, $F(t)$, and the drag force calculated above. Newton's second law can therefore be written as follows:[61]

$$6\pi\eta Rv + F(t) = m\frac{dv}{dt} \tag{1.16}$$

where m is the mass of the sphere and $\frac{dv}{dt}$ represents the acceleration.

Solving for $v(t)$ and then the variance of the displacement $\frac{dx^2}{dt}$ and substituting Equation 1.14 for $\langle x \rangle$ gives the equation for the diffusion coefficient D of a sphere:

$$D = \langle v^2 \rangle \frac{m}{6\pi\eta R} \tag{1.17}$$

where $\langle v^2 \rangle$ is the mean velocity, which can be calculated from the relationship between kinetic energy and absolute temperature T given below:

$$\frac{1}{2}m\langle v^2 \rangle = \frac{1}{2}k_B T \tag{1.18}$$

where k_B is the Boltzmann constant. Therefore, solving for $\langle v^2 \rangle$ gives

$$\langle v^2 \rangle = \frac{k_B T}{m} \tag{1.19}$$

This value can then be substituted back into Equation 1.17 to give the Stokes-Einstein expression for the diffusion coefficient of a sphere, which is dependent on the temperature, solution viscosity, and particle radius:[61]

$$D = \frac{k_B T}{6\pi\eta R} \tag{1.20}$$

As this expression shows, the diffusion coefficient is larger for smaller particles.

1.2.4 Convection

Convection is the movement of the solvent due to an external force such as pressure, an electric field, mechanical motion, etc.[52] This section will focus on two of the most common causes of solvent flow in nanochannels: pressure and electroosmosis.

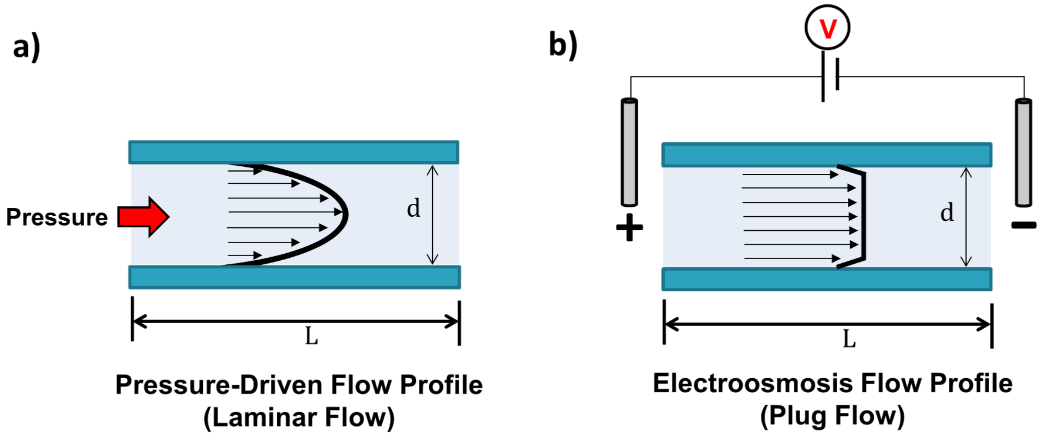

FIGURE 1-3: Comparison of the fluid flow profiles for pressure-driven (a) and electroosmotic-driven (b) flow inside a nanochannel of diameter d and length L with a negative surface charge.

Pressure

Pressure-driven flow through a cylindrical channel is known as Poiseuille flow and displays the characteristic parabolic velocity profile shown in Figure 1-3a. The fluid velocity as a function of distance away from the center of the channel $v(r)$ can be solved for exactly using the Stokes equation described above, assuming that the velocity is zero at the channel walls (the no slip boundary condition):[61,61,90]

$$v(r) = -\frac{\Delta P}{4\eta}\left(R^2 - r^2\right) \tag{1.21}$$

where ΔP is the pressure gradient across the channel, η is the solution viscosity, and R is the channel radius. The average velocity v_{avg} is calculated to be:

$$v_{avg} = \frac{\Delta P R^2}{8\eta} \tag{1.22}$$

The maximum velocity v_{max} occurs in the center of the channel and is two times higher than v_{avg}. The volumetric flow rate Q can be determined by multiplying v_{avg} by the cross-sectional area of the channel and is given by

$$Q = \frac{\Delta P \pi R^4}{8\eta} \tag{1.23}$$

Therefore, the resistance to flow increases dramatically as the diameter of the channel decreases, requiring much higher applied pressures to achieve the same velocity, which has important implications in the design of micro- and nanofluidic systems. The time it takes for the parabolic flow to develop in the channel is defined as the entrance length $L_{entrance}$ and can be estimated as follows:[61]

$$L_{entrance} = D_h \frac{0.6}{1 + 0.035R_e} + 0.056R_e \tag{1.24}$$

where D_h is the hydraulic diameter and R_e is the Reynolds number. As a result of the low Reynolds numbers typically encountered in micro- and nanochannels, the entrance length is negligible, and the flow can be considered as fully developed laminar flow right at the channel entrance.[61]

Due to the parabolic nature of the velocity profile, pressure-driven flow can be used to separate solutes of different sizes in a technique known as hydrodynamic chromatography.[102–104] This method is based on the increased probability of larger particles coming into contact with the fluid in the center of the channel where the flow is fastest. They will therefore travel faster along the length of the channel than smaller particles, allowing the two sizes to be separated over time.

Electroosmosis

Electroosmosis is one of the primary electrokinetic effects mentioned above and was first discovered in 1809 by F.F. Reuss, who noticed that water moved through porous clay under the application of an electric field due to the acquisition of surface charge on the clay particles in contact with the solution.[105] The diffuse layer of the EDL contains a net charge that can move under the influence of an electric field. This movement drags the surrounding solution with it due to viscous interactions, causing the flow of the entire fluid volume and all species contained therein in the same direction, regardless of charge.[52] This produces a flow profile known as plug flow (shown in Figure 1-3), in which the velocity profile is constant throughout the channel cross-section except in the EDL region near the wall, where it quickly decreases to zero. One major advantage of electroosmotic flow is that outside the EDL region, the uniform velocity means there is no shear in the flow, which prevents dispersion. Therefore, electroosmosis is often used as the major mode of transport in many separation techniques because it avoids band broadening and increases resolution relative to pressure-driven flow.[105]

In the limit of small EDL thicknesses, the Navier-Stokes and Poisson-Boltzmann equations can be significantly simplified to give the electroosmotic velocity v_{eo} :[52]

$$v_{eo} = \frac{\varepsilon_0 \varepsilon \zeta_w E}{\eta} \tag{1.25}$$

where ε_o is the permittivity of free space, ε is the dielectric constant of the solvent, ζ_w is the zeta potential at the wall, η is the viscosity of the solvent, and E is the magnitude of the electric field. The electroosmotic mobility μ_{eo} is the ratio of the average electroosmotic velocity to the electric field and is given by[52]

$$\mu_{eo} = \frac{\varepsilon_0 \varepsilon \zeta_w}{\eta} \tag{1.26}$$

In very small nanochannels at low ionic strength, EDLs from the channel walls can overlap, preventing the electric potential from reaching zero in the center of the channel. In this case, the velocity profile is much more complicated and follows the electric potential, with the electroosmotic velocity given by[52]

$$v_{eo} = \frac{\varepsilon_0 \varepsilon \zeta_w E}{\eta} \left(1 - \frac{\phi(z)}{\zeta_w} \right) \tag{1.27}$$

where $\phi(z)$ is the potential distribution between two parallel plates.

Streaming Potential and Sedimentation Potential

Streaming potential, another electrokinetic effect, originates from the flow of an electrolyte solution over a charged surface (i.e. motion of the mobile ions in the double layer) and is often driven by pressure. This motion produces a current known as the streaming current. Consequently, ions build up at the downstream end, creating an electric field which triggers a reverse electroosmotic flow in the opposite direction (conduction current). This backwards current reduces the net flow in the forward direction, increasing the apparent viscosity of the liquid. This is known as the electroviscous effect.[52, 106]

The counterpart to streaming potential is sedimentation potential. While not caused by pressure, it is a related electrokinetic effect that occurs when charged particles, rather than the fluid, are pulled through a liquid by gravity or centrifugation. This movement disturbs the equilibrium structure of the EDL around each particle and causes ions in the diffuse layer to lag behind, producing an electric potential difference that hinders the motion of the particles.[101]

1.2.5 Migration

Migration is the movement of a charged species through a fluid due to the presence of an electric field. The last electrokinetic effect mentioned earlier, electrophoresis, falls under this category and will be discussed here.

Electrophoresis

Electrophoresis is the movement of a solute relative to the stationary surrounding fluid and is caused by the EDL formed at the interface of the particle and the solution. The electrolyte screens the solute charge, making it effectively neutral in solution. However, the diffuse mobile layer of the EDL has a net charge and will respond to the electric field, causing the fluid around the solute to move by electroosmosis. Since the charge of the EDL is by necessity opposite of the solute charge, this fluid motion will be in the reverse direction from the direction that the solute would move in the electric field if it was not screened. Given that the bulk fluid is kept stationary by the viscosity of the solution, the solute is pushed backwards in response to this electroosmotic fluid flow (and consequently in the same direction it would move with no screening).[52] Electrophoresis is frequently used to analyze and separate DNA and other charged species as they travel through pores in a gel or membrane.[40,83,107] The solute will experience drag as it moves through the fluid and will be accelerated in an electric field only until the electrical force is balanced by the viscous drag force as shown below:[90,100]

$$qE = 6\pi\eta r v_{ep} \tag{1.28}$$

where q is the surface charge of the particle, v_{ep} is the electrophoretic velocity, and r is the solute radius. When the EDL is thin compared to the molecular radius, the electrophoretic velocity is analogous to the electroosmotic velocity described above and is given by[52]

$$v_{ep} = \frac{\varepsilon_0 \varepsilon \zeta_p E}{\eta} \tag{1.29}$$

where ζ_p is the zeta potential of the particle. Similarly, the electrophoretic mobility μ_{ep} is simply the ratio of the average electrophoretic velocity to the applied electric field:[52]

$$\mu_{ep} = \frac{\varepsilon_0 \varepsilon \zeta_p}{\eta} \tag{1.30}$$

For very small molecules or particles, where the thickness of the EDL is greater than the radius of the molecule, the electrophoretic velocity becomes

$$\mu_{ep} = \frac{2\varepsilon_0 \varepsilon \zeta_p}{3\eta} \tag{1.31}$$

Combination of Electophoresis and Electroosmosis

It is important to mention that although electroosmosis causes solvent flow, it also drags along any species in solution, thereby indirectly triggering solute movement as well. Often electroosmosis and electrophoresis occur simultaneously. The total velocity due to the electric field is then simply the sum of the velocities from these two effects:[33]

$$v_{tot} = v_{ep} + v_{eo} = \frac{\varepsilon_0 \varepsilon}{\eta} \left(\zeta_p - \zeta_w\right) E \tag{1.32}$$

The direction of v_{eo} will always be opposite from v_{ep}, necessitating the introduction of a negative sign in the equation above. The final direction of transport is determined by the comparative magnitudes of the zeta potentials of the solute and the channel wall. If the zeta potential of the solute is greater than that of the wall, electrophoresis will dominate, and vice-versa.

Dielectrophoresis

Dielectrophoresis is another related effect that describes the movement of a polarizable particle in response to a nonuniform electric field. The time-averaged dielectrophoretic force F_{DEP} is given by[90,108]

$$F_{DEP} = 2\pi\varepsilon_0\varepsilon R^3 CM\left(\nabla E^2\right) \tag{1.33}$$

where R is the particle radius, E is the electric field, and CM is the Clausius-Mossotti factor, which is related to the effective polarizability of the particle and is defined as[108]

$$CM = \left(\frac{\varepsilon_p - \varepsilon_m}{\varepsilon_p + 2\varepsilon_m}\right) \tag{1.34}$$

where ε_p and ε_m are the complex permittivities of the particle and the solution, respectively.

The polarizability of the particle is dependent on frequency, enabling particle separation using AC fields of different frequencies.[99,108] Electrophoresis, electroosmosis, and dielectrophoresis have all been used to manipulate and separate a wide range of analytes, including nanoparticles, biomolecules, and cells.[51,86,99,108,109]

1.3 Brief Outline of Dissertation

The research presented here investigates the intersection of electrochemistry and transport behavior in solutions under confinement.

Chapters 2 & 3 describe two projects focused on better understanding and controlling transport dynamics in silica nanochannels using electrochemical techniques. A detailed description of the silica nanochannel fabrication method is included in the appendix. Chapter 2 briefly reviews the field of bipolar electrochemistry and summarizes traditional nanoelectrode fabrication methods. The majority of this chapter describes a unique method for wireless, *in situ* control of single metal nanowire growth in a silica nanochannel using an applied electric field to tune the deposition rate. Solutions of a metal ion precursor and a reducing agent are initially placed on either side of a channel and allowed to mix inside, with ion transport controlled by the applied electric field. Deposition occurs first by direct chemical reduction until the channel diameter is blocked, after which it continues by a bipolar mechanism, with coupled oxidation and reduction reactions occurring at opposite ends of the growing wire. The deposition rate can be modified during the growth process by altering the applied electric field, offering precise control over the synthesis.

Chapter 3 reports a comprehensive study of material-dependent size selectivity observed in the transport of silica and polystyrene nanoparticles through silica nanochannels detected by resistive-pulse sensing. We examine the roles of basic driving forces as well as subtler charge effects, finding that dynamical charge-related properties and processes could be playing a significant role in size selectivity. Importantly, this suggests that nanoscale phenomena can affect mesoscale transport behavior when the particle diameter approaches the size of the channel diameter, which could have significant implications for many other natural and synthetic nanoporous transport systems.

Chapter 4 discusses two original methods for gold nanoelectrode fabrication based on previously reported nanowire synthesis techniques (nanoskiving and lithographically patterned nanowire electrodeposition (LPNE)) and examines the benefits and difficulties associated with using these techniques to prepare nanoelectrodes with controllable and reproducible dimensions.

Chapter 5 covers the synthesis of nanowire arrays based on previously established methods for use in electrochemical sensing studies and compares the challenges and success rates achieved using different methods and materials. We show that electroless deposition produces the most uniform and reproducible arrays and that controlling mass transport is key to obtaining uniform deposition. We conclude with a brief summary of the observations and conclusions drawn from this work.

Chapter 2

Dynamic *In Situ* Control of Single Metal Nanowire Growth

In this chapter, we describe a method for achieving dynamic *in situ* control over single metal nanowire growth in a silica nanochannel template. This work relies on a bipolar electrochemical mechanism to achieve sustained growth. Therefore, we first introduce the fundamentals of bipolar electrochemistry, followed by a brief overview of traditional single nanoelectrode fabrication methods in order to place this work in a broader context and highlight the advances achieved in this chapter and Chapters 4 & 5. It should be emphasized, however, that the main purpose of the project discussed in this chapter is to demonstrate that an electric field can be used to wirelessly control mass transport in a nanochannel, enabling precise tuning of the deposition rate during the growth process. While we demonstrate that the resulting nanowire can be used as a nanoelectrode, the focus is really on developing a general method for metal nanowire fabrication and has other applications outside of traditional nanoelectrode use, whereas the projects reported in Chapters 4 & 5 were developed with the specific intent to prepare gold nanoelectrodes.

2.1 Bipolar Electrochemistry

Bipolar electrochemistry exploits the interfacial potential difference that develops between a conductive material and the surrounding electrolyte solution in the presence of an electric field. This potential difference varies along the length of the material according to the effective electric field strength in solution but is highest at either end, creating a bipolar electrode with anodic and cathodic regions at opposite poles. Oxidation reactions at the anodic end are therefore coupled to reduction reactions at the cathodic end.[110] One of the main advantages of bipolar electrochemistry arises from the fact that no electrical connection to the material is required, making it effectively wireless. Therefore, it is particularly useful for nanofabrication

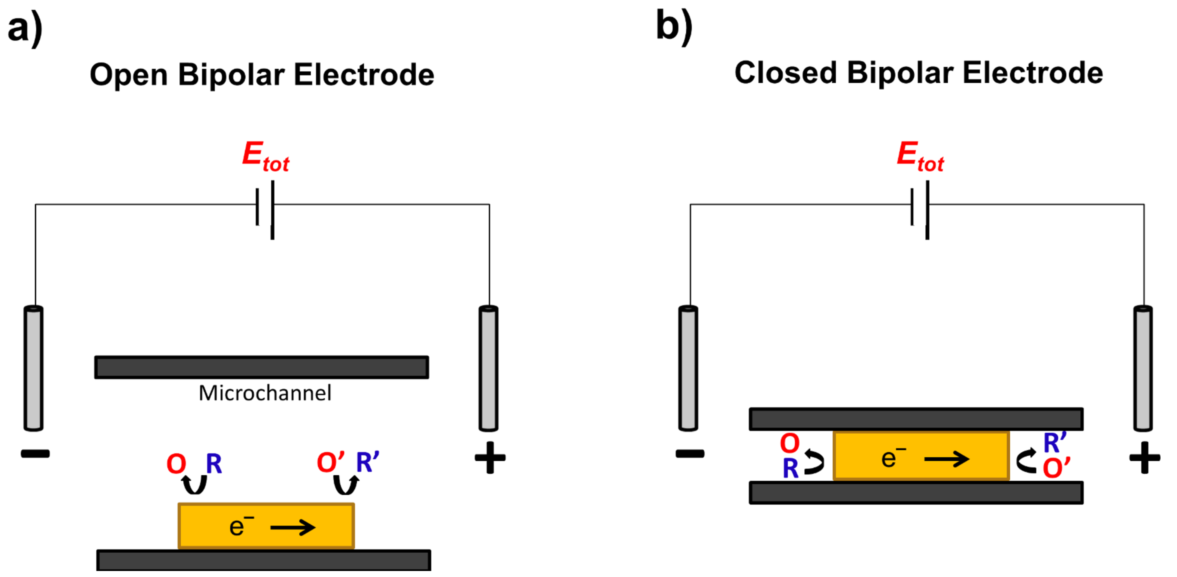

FIGURE 2-1: Comparison of open and closed bipolar systems. In an open system (a), the electrode is surrounded by electrolyte solution, and the total current through the system is a combination of faradaic and ionic current, making it difficult to obtain quantitative electrochemical information. Conversely, in a closed system (b) the electrode is insulated, meaning that the faradaic current through the electrode is the only current source. This allows the measured current to be directly and quantitatively correlated to electrochemical reactions occurring at the electrode surface.

and other situations for which making electrical contact to the substrate is challenging.[110–112] Although there has been a recent resurgence of interest in bipolar electrochemistry, it was first introduced in the 1960s, when Fleischmann, Goodridge, Wright, and coworkers observed electrochemical reactions occurring at the surface of conductive particles when a voltage was applied across the solution using two driving electrodes.[113–116] These electrochemical systems, known as fluid bed electrodes, have since found use in an assortment of applications, including photoelectrochemistry,[117] batteries,[118] and fuel cell technology.[119,120]

Many new bipolar applications have been demonstrated recently, including wireless control over the potential of a nanoelectrode array,[121] selective metal deposition,[122–126] propulsion of small bipolar materials by bubbles produced by the coupled reactions or regeneration of the material itself,[127,128] separation of charged species,[129] sensors,[130,131] and preparation and screening of electrocatalytsts.[132–134]

Most of these examples use an open bipolar electrode setup (shown in Figure 2-1a), in which the electrode material is completely surrounded by the electrolyte solution. In this system, it is difficult to quantitatively measure the reaction rate at the bipolar electrode since the total observed current is a combination of the faradaic current carried through the electrode and the ionic current carried through the solution.[110,135] In addition, the total potential required to drive the redox reactions at either end of the electrode is usually quite high (ranging from 20V[135] up to tens of kV[110]), although the exact value depends on the particular electroactive species in solution as well as the ratio of the electrode length to the channel length.

Our group has recently focused on studying closed bipolar electrode systems (shown in Figure 2-1b), in which the electrode is insulated and the two solutions in contact with the anodic and cathodic ends are physically separated. This effectively creates two separate electrochemical cells connected in series and eliminates the ionic current pathway described above. Consequently, the observed current can be solely attributed to the faradaic reactions occurring at either end of the wire, providing a direct measure of electrochemical reaction rates. Moreover, the potential required to drive these reactions is much smaller than for open bipolar electrode systems (usually less than 1V). Our fundamental studies on bipolar electrochemistry have led to several important conclusions,[136, 137] which can be summarized as follows:

1. The current measured in a closed bipolar electrochemical setup quantitatively reflects the faradaic reactions occurring at the limiting pole of the bipolar electrode.

2. If the voltage needed to drive the reaction at the complementary pole is too high, the reaction kinetics will be slowed down, producing a broadened CV response compared to that obtained with a traditional electrochemical setup. This can complicate the use of bipolar electrodes for quantitative measurements.

3. The voltage requirement mentioned in (2) can be effectively reduced by either:

    - Increasing the area of the complementary pole.
    - Increasing the redox concentration at the complementary pole.

    Assuming that the area or redox concentration at the complementary pole is large enough, a bipolar electrode can be used in the same way as a traditional electrode.

4. The relationship between the maximum steady-state limiting currents at the anodic and cathodic poles of a bipolar electrode (i_{ss}^{a} and i_{ss}^{c}) and the half-wave potential of the corresponding CV ($E_{1/2}$, the potential when the current is half of its steady-state value) is given by the following equation:[136]

    $$E_{1/2} = \left(E_a^{\circ'} - E_c^{\circ'}\right) - \frac{RT}{F} ln\left(-2\left(\frac{i_{ss}^{c}}{i_{ss}^{a}}\right) - 1\right) \tag{2.1}$$

    where $E_a^{\circ'}$ and $E_c^{\circ'}$ are the formal potentials for the reactions occurring at the anodic and cathodic poles, respectively, and the cathodic current is defined as negative.

The work contained in this chapter builds off of these fundamental observations, using a bipolar electrochemical mechanism to overcome traditional challenges in nanofabrication and achieve unique dynamic control over metal deposition rates.

2.2 Overview of Nanoelectrode Fabrication Techniques

As mentioned in the introduction, much of the recent progress in electrochemistry can be attributed to the development of ultramicroelectrodes, which have enabled dramatic improvements in spatial and temporal analysis. Nanoscale band electrodes were first reported in the mid-1980s by multiple groups.[24,138,139] While UMEs of many different geometries can be prepared,[140] including band,[24,138,139,141,142] nanopore,[143–146] ring-disk,[147–150] and hemisphere electrodes,[151,152] disk electrodes have emerged as one of the most widely used due to their well-defined structure and relative ease of fabrication. Although numerous fabrication methods have been employed, the majority involve encasing a metal wire or carbon fiber in an insulating material before polishing the tip to expose the metal electrode.[153–155,155] These nanoscale wires or fibers can be created using several different techniques, including laser-assisted pulling of a microwire sealed in a glass capillary,[6,156–160] etching of a microwire in NaCN or $CaCl_2$ solution,[5,144,156,161] photolithography,[162–164] or electroless deposition[165] and can be subsequently insulated using glass[5,144,154,156,166] or electrophoretic paint.[5,167,168] However, there are several common challenges to achieving reproducible electrode fabrication, including forming a complete seal between the insulating layer and the metal electrode to prevent leakage of ionic current, and polishing difficulties, which can result in broken tips or larger-than-expected electrode diameters due to the tapered shape of many of the wires. Thus, despite these advances there is still room for significant improvement.

Gold nanoelectrodes are particularly desirable due to their chemical stability and straightforward, well-established surface functionalization methods, which make them especially advantageous for electrochemical sensor applications[20,21,23,95,148,169–172] and catalytic studies,[20,173,174] as the surface can be modified with nanoparticles, enzymes, DNA, or target molecules to impart specificity or facilitate single-particle detection and analysis. However, the low melting point of gold makes it very challenging to use traditional laser-assisted pulling methods (such as those mentioned above) to fabricate these electrodes, instead necessitating the use of deposition,[19,50,165] etching,[144] evaporation techniques[175,176] or photolithography.[172,177,178] Nonetheless, it remains difficult to produce single, electrically insulated nanowires using these approaches. In this dissertation, we focus on overcoming these limitations to develop new, simple, controllable, and reproducible methods for the fabrication of gold nanoelectrodes with tailored geometry and dimensions.

2.3 Dynamic *In Situ* Control of Single Metal Nanowire Growth

Note: This portion of the chapter is reproduced with permission from ACS Nano, submitted for publication. Unpublished work copyright 2014 American Chemical Society.

2.3.1 Introduction

Metal nanowires have garnered considerable research attention due to their impressive versatility, with unique electrical, optical, and catalytic properties that make them well-suited for applications in nanoelectronics,[179–183] optics,[184–187] sensing,[19,21,23,170] and electrochemistry.[13,20,92,188] Since these properties are determined by the structure and crystallinity of the wire, controlled fabrication is critical for customization. While numerous synthesis techniques have been employed,[176,177,189–191] template-confined deposition[192–194] has emerged as one of the most popular due to two major advantages—it allows the morphology and location of metal growth to be precisely tailored by the template architecture, and it imposes transport limitations that help regulate growth kinetics.

Template-confined deposition is typically carried out using either electrochemical or electroless techniques. In electrochemical deposition,[44–46,195–197] metal ions are reduced at a conductive surface on the template by an applied potential, which can be adjusted to tune growth rate and crystallinity. While this straightforward control enables high-quality unidirectional growth, it requires a direct electrical connection to the template, which is often difficult to establish on the nanoscale. Conversely, electroless deposition[47,48,50,198] occurs by direct chemical reduction and does not require an electrical connection or an applied potential, resulting in a considerably simpler setup that is more conducive to nanoscale fabrication. However, it often requires preactivation of the surface by several additional steps, and the growth rate and direction are less controllable. Ideally, the benefits of both electrochemical and electroless deposition could be combined to yield a simple setup that requires no direct electrical connection or surface preactivation but maintains the control afforded by an externally applied potential.

Indeed, many recent reports have made exciting progress toward combining these advantages. For example, Drndic and coworkers[74] demonstrated the fabrication of a single gold nanoparticle inside a silicon nitride pore by chemical reduction, with the mixing of precursor solutions regulated by an applied electric field. However, this process is self-limiting, preventing further growth after the short pore length is blocked. Nanoparticles and nanowires have also been fabricated on a variety of conductive surfaces by using a supportive metal substrate with the appropriate redox potential to drive the reduction of metal ions in solution.[49,199,200] In addition, several studies have deposited metal in between conductive microparticles or at the end of carbon micro-/nanotubes by a wireless method known as bipolar electrodeposition, in which an applied electric field, rather than a direct electrical connection, is used to drive one-dimensional metal growth.[123,125,126,201–203] This approach requires a conductive starting substrate, which develops locally anodic and cathodic regions that facilitate coupled oxidation and reduction reactions. However, these substrates are difficult to fabricate and immobilize on the nanoscale, and the absence of a template eliminates the beneficial morphological and growth rate control that results from physical confinement. Furthermore, this method necessitates the application of very high potentials (usually tens of kV), and the measured current cannot be used to directly monitor the reduction reaction since it is a combination of both faradaic and ionic current.

In order to bypass the necessity for an initial conductive starting substrate while maintaining the advantages of a template, a few reports have used an innovative two-step process in which direct chemical reduction is first employed to create metallic anchor segments in the pores of an array that can act as substrates for subsequent bipolar wire growth. This additional growth is driven by the difference between the redox potentials of the two precursor solutions rather than an applied electric field.[204–207] However, this method does not produce electrically insulated wires, which are critical for many electrical and electrochemical applications. Moreover, the wires are frequently grown in arrays rather than individually. Although wires can be released from a templated array, manipulating single, free-standing wires for use in devices is extremely challenging.

Most importantly, the deposition rate in a template-confined system is determined by how fast the redox species reach the surface of the growing wire, and in the above examples this rate can only be controlled by changing the identities or concentrations of the redox species, which alters both the electrochemical driving force and the transport kinetics (due to changes in chemical potential). These parameters must be optimized for each experimental system and are set before the reaction begins. Consequently, they cannot be easily adjusted during the growth phase, even though deposition is a dynamic process, with local concentrations in constant flux as reagents are consumed and transport distances change with the shifting deposition site.

Here we present a bipolar electrochemical method for *in situ* control of single metal nanowire growth, showing that the deposition rate can be dynamically adjusted by applying an independently tunable electric field of less than 1 V during the growth process. We demonstrate this enhanced control by depositing a single gold nanowire in a silica nanochannel template using a two-step chemical/bipolar electrochemical reduction mechanism while simultaneously monitoring both the current-time trace and optical microscope video of the growth process in real time. This method is highly reproducible and requires no direct electrical connection, and scanning electron microscope (SEM) images show that the resulting wire is solid throughout its length. The use of a silica nanochannel template results in a single nanowire rather than a nanowire array. This allows us to accurately correlate electrical and optical observations with wire growth and regulate deposition without complications from ensemble effects. It also enables the insulated wire to be used as a bipolar nanoelectrode or to be easily manipulated and positioned for use in other applications that require isolated wires. Additionally, compared to the planar diffusion that occurs in an array configuration, radial diffusion to a single channel opening offers a fundamental transport advantage, aiding growth kinetics by increasing mass transport and avoiding quick depletion of the metal ions at the nanowire surface.

2.3.2 Results and Discussion

Overview of Deposition Process

A diagram of our setup is shown in Figure 2-2. A cylindrical-shaped silica nanochannel was fabricated at the end of a glass micropipette according to our previously published method[208] and employed as a template for metal deposition. Most nanochannels used in this work were between 200-400 nm in diameter and 20-50 μm in length. The nanochannel was filled with 50 mM gold (III) chloride ($HAuCl_4$) in 0.1 M potassium chloride (KCl) and placed inside an empty solution chamber. A Ag/AgCl electrode was inserted into the supporting pipette of the nanochannel and another was inserted into the solution chamber. The whole ensemble was positioned under an upright microscope in order to visually observe wire growth while simultaneously monitoring the resulting current. An initial potential of -0.6 V was applied to the working electrode (defined as the electrode in the $AuCl_4^-$ solution), and a solution of 50 mM sodium borohydride ($NaBH_4$) in ethanol was introduced into the solution chamber to initiate the reaction. Ethanol was chosen instead of water because $NaBH_4$ reacts with different solvents to varying degrees, and the decomposition of $NaBH_4$ in ethanol is much slower than it is in water.

Gold growth proceeds in two stages: initial chemical reduction that generates gold particles until the channel is blocked, followed by bipolar electrochemical deposition that furthers the growth of the nanowire. Externally connecting the $AuCl_4^-$ and BH_4^- redox solutions creates a closed circuit, forming a simple battery that not only helps direct solution mixing during the initial chemical reduction phase but also drives the subsequent elongation of the wire. It is difficult to calculate the expected battery potential based on the standard redox potentials of the two solutions since the redox potential of BH_4^- is known to be solvent dependent and is not reported for ethanol. However, we measured the cell potential to be $\sim$1.2 V using a salt bridge to connect the two bulk redox solutions.

This spontaneous electrochemical potential is set by the identities and concentrations of the redox species, which cannot be easily or controllably adjusted during the growth process. However, these concentrations naturally fluctuate during the reaction as reagents are consumed and transport limitations change, causing simultaneous variations in both the battery potential and mass transport to the deposition site. Therefore, we introduce an independent, externally applied electric potential across the two Ag/AgCl electrodes that allows us to dynamically tune the total driving force of the system *in situ*. The equivalent circuit model for our setup is shown in Figure 2-2b. Depending on its polarity, this additional potential will either enhance or oppose the battery potential, providing a significant degree of control. This is particularly beneficial during the bipolar electrochemical deposition phase, in which the growth of the short section of gold formed by chemical reduction is driven by coupled oxidation and reduction reactions at opposite ends of the growing nanowire. Adjusting this externally applied potential therefore gives precise control over the growth rate of the gold during this

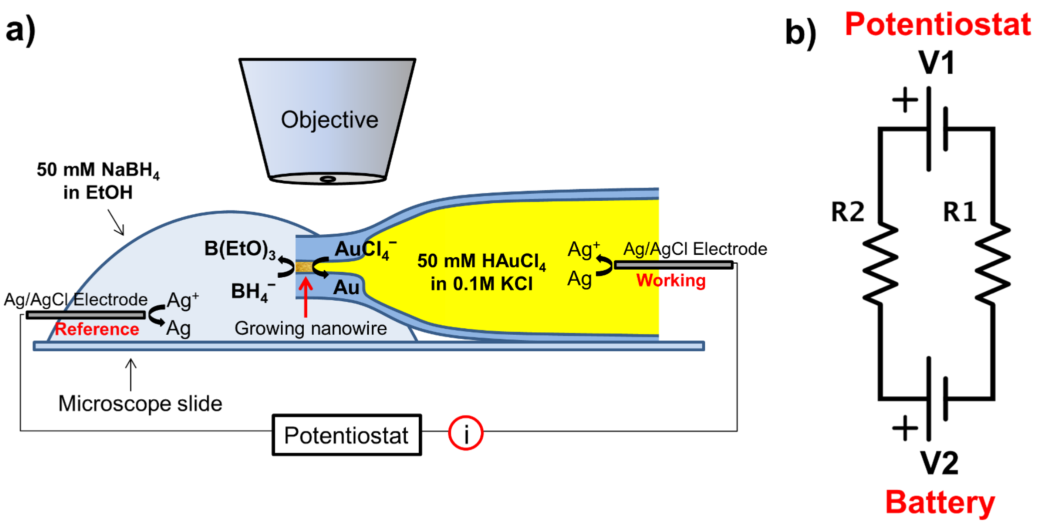

FIGURE 2-2: (a) Schematic of controlled nanowire deposition inside a silica nanochannel by a two-step mechanism requiring no direct electrical connection to the template. When the two precursor solutions meet at the channel entrance, BH_4^- reduces $AuCl_4^-$ on contact, blocking the channel diameter. The redox potential difference between the two solutions creates an inherent battery potential that drives subsequent growth by a bipolar electrochemical mechanism, with $AuCl_4^-$ reduction at one end of the wire coupled to BH_4^- oxidation at the other. Electroneutrality is maintained by electron flow through the external circuit. The deposition rate can be dynamically controlled *in situ* by applying an independently tunable electric potential across the channel (via a potentiostat) to either enhance or oppose the battery potential. (b) Equivalent circuit diagram of our setup, where V1 is the potentiostat voltage, V2 is the spontaneous battery voltage, R1 is the resistance of the $HAuCl_4$ solution and R2 is the resistance of the $NaBH_4$ solution.

period.

Chemical Reduction Phase

Initial gold deposition occurs by chemical reduction when the two redox solutions meet according to the following reaction:

$$8AuCl_4^- + 3BH_4^- + 9EtOH \Longrightarrow 8Au_{(s)} + 3B(EtO)_3 + 21H^+ + 32Cl^- \tag{2.2}$$

Ideally this chemical reduction phase would be both fast and localized, immediately forming a short section of gold to plug the channel. While it is difficult to completely control the preliminary solution mixing, the potential across the channel provides a significant degree of regulation due to the identical charges of the two redox species. The $AuCl_4^-$ ions are driven into the channel, away from the electrode in the pipette (defined as the working electrode), while the BH_4^- ions migrate away from the channel, toward the electrode in the external solution (defined as the reference electrode). Consequently, the initial interface of the two solutions is always located at the outside channel opening near the BH_4^- solution, which allows for consistent, reproducible control of both the starting point and direction of wire growth. It is important to note that the initial concentrations, while not easily controlled during the growth process, do play a vital role in determining how this chemical reduction phase proceeds. If the concentration of $NaBH_4$ is too high, there are too many nucleation sites, and deposition proceeds rapidly down the length of the channel without blocking the diameter. Similarly, if the concentration of $NaBH_4$ is too low, the rate of gold deposition is too slow to quickly block the channel, and growth likewise continues along the walls rather than across the width. Both situations produce porous wires. An additional transport hindrance is imposed on the $AuCl_4^-$ ions since they must travel through the channel to reach the deposition front. A 50 mM concentration of both $HAuCl_4$ and $NaBH_4$ was found to give a good balance between a reasonable number of nucleation sites and a fast enough chemical reduction rate.

Figure 2-3 shows a typical current-time trace with corresponding optical microscope images of the growing nanowire at different time points during the deposition. After $NaBH_4$ is initially added, a sudden increase in ionic current is observed as the solutions meet and the circuit is completed. The sign of the current is negative in accordance with the polarity of the potential. The current then immediately begins to decrease as gold is deposited at the channel entrance, shrinking the effective diameter of the channel. However, after this initial decrease, the current fluctuates significantly, reflecting the dynamic nature of this chemical reduction phase. Since BH_4^- reduces $AuCl_4^-$ on contact as soon as the solutions meet, there are multiple nucleation points for gold growth. Therefore, as Wong and coworkers have noted, this initial portion of the wire likely consists of many small gold nanoparticles connected together and is probably somewhat porous in nature.[205] This is confirmed by the SEM image of the outer section of the wire (Figure 2-9a), which shows aggregates of gold particles joined together. It is possible that initially-formed gold nanoparticles or aggregates are easily dislodged from the channel before they can establish a strong anchor, causing the observed current fluctuations as they travel through and exit the channel. This conclusion is supported by the fact that these fluctuations resemble stochastic particle detection events observed in resistive-pulse sensing of nanoparticles passing through a nanopore.[96] Therefore, we believe this is the most likely explanation for this variable current behavior.

Eventually, the particles form a large and stable enough conglomerate to completely obstruct ion flow through the channel, as indicated by the subsequent current decrease to zero. Due to the nature of this initial chemical deposition, we have oriented our solutions with $AuCl_4^-$ on the inside and BH_4^- on the outside so that this more porous part of the wire is located near the outside of the channel and can be easily removed by focused ion beam milling, polishing, or etching.

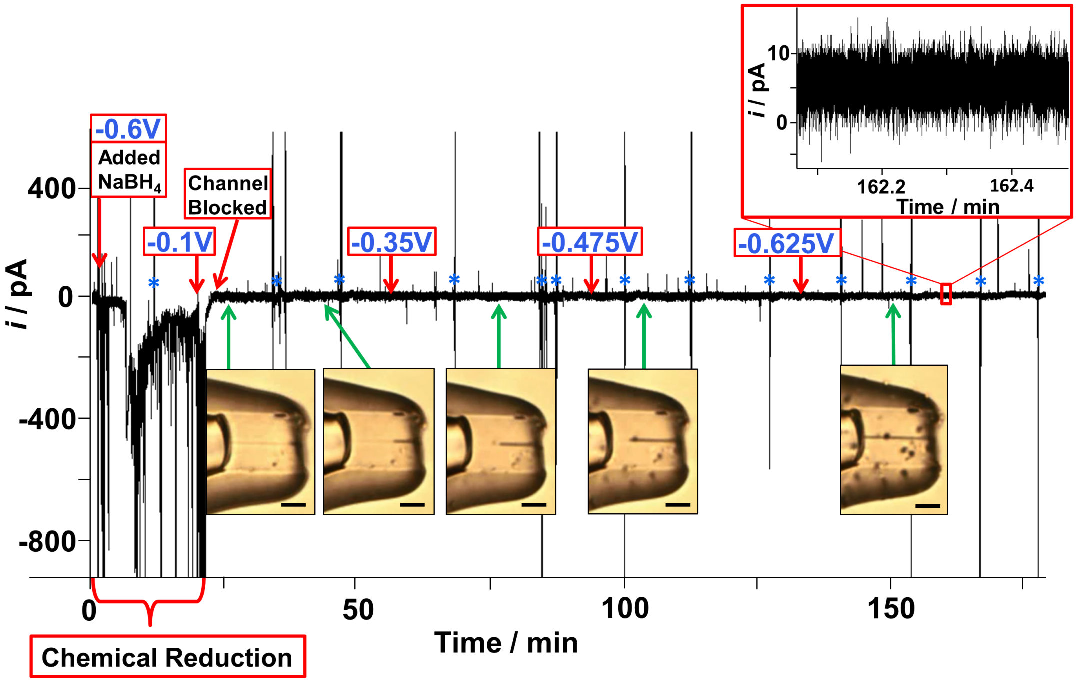

FIGURE 2-3: Current-time trace for gold deposition in a 293-nm-diameter channel, along with accompanying optical microscope images at different time points during the growth process. The voltage values represent the external potential applied at the indicated times. An increase in ionic current is observed after adding $NaBH_4$ due to completion of the circuit through the channel. An external potential is applied during this initial stage to help direct solution mixing. Particle formation and translocation through the channel are likely responsible for the transient current fluctuations observed until the channel is fully blocked (indicated by a current decrease to zero). The subsequent small, positive faradaic current represents the onset of bipolar electrochemical deposition. As deposition proceeds, decreased mass transport resistance causes a natural increase in the deposition rate, which is countered by gradually increasing the magnitude of the externally applied potential to maintain an average rate of 3.1 nm/s. The blue asterisks indicate each time more $NaBH_4$ solution was added to the soution chamber. The large vertical current spikes correspond directly to these additions and are due to physical disruptions to the setup during these periods. The much smaller current spikes are due to footsteps and other small vibrations. Dark particles seen on the outside of the channel are small pieces of silicone rubber that have broken off from the chamber seal and do not affect the deposition process. All scale bars are 10 μm.

Solution Mixing Behavior without Potentiostat Control

While we have found that controlling the potential during this initial phase provides the best control over the rate of blockage formation, it is interesting to note that just the presence of a closed circuit (without the potentiostat) has a regulatory effect on solution mixing. This is illustrated by comparing the behavior observed in two control experiments: one without an external electrical connection and one with only a wire connecting the two Ag/AgCl electrodes (no potentiostat). With no external connection between the redox solutions (Figure 2-4), their mixing is controlled solely by diffusion, and gold growth occurs exclusively by chemical

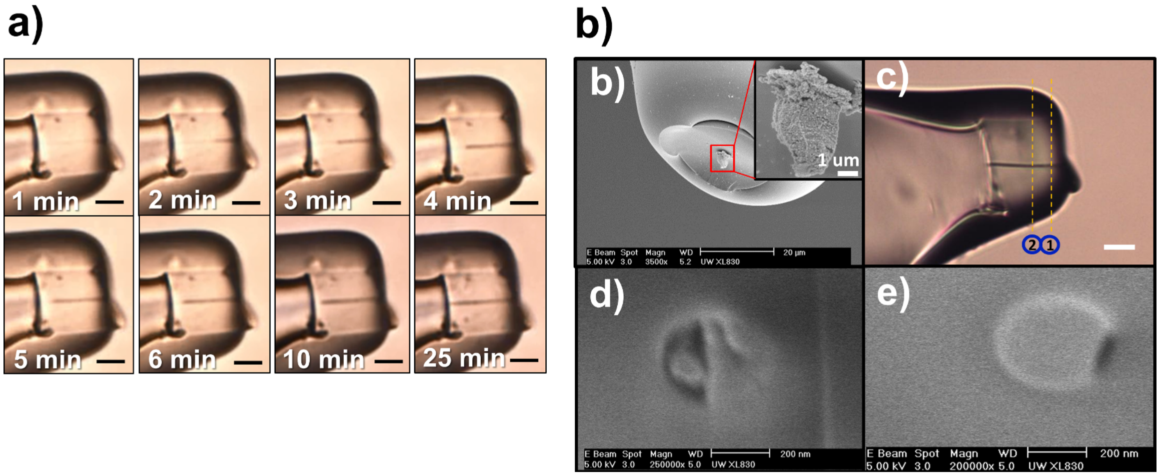

FIGURE 2-4: Control experiment performed in a 289-nm-diameter channel with no external electrical connection. (a) Optical microscope images of wire growth at different time points during the deposition. Transport is controlled by diffusion, and growth occurs solely by chemical reduction, proceeding rapidly down the length of the channel due to the simultaneous formation of multiple nucleation sites. Eventually deposition slows down as the reduced gold finally blocks the channel diameter. (b) SEM image of the wire before cutting, showing the outer portion of the wire formed by chemical reduction. (d-e) SEM cross-section images of the wire: after the first (d) and second (e) FIB cuts at the approximate locations indicated in (c). The wire is not completely solid due to the fast growth rate. All scale bars are 10 μm unless otherwise indicated.

reduction. As BH_4^- infiltrates the channel, rapid gold deposition takes place at multiple nucleation sites simultaneously, producing a porous wire that begins its growth at various locations in the channel. Consequently, the deposited gold does not initially block the channel diameter, instead continuing quickly down the sidewalls. As the wire approaches the end of the channel, the deposition rate slows down since the majority of the channel breadth has finally been blocked and mass transport through the channel is severely hindered. Conversely, the initial mixing behavior in the channel with the two Ag/AgCl electrodes connected only with a wire (Figure 2-5) shows a much slower and more controlled growth rate that is quite similar to the channel under potentiostat control shown in Figure 2-3.

Bipolar Electrochemical Deposition Phase

After the channel is fully obstructed and the solutions are no longer in physical contact, the growth mechanism switches from chemical reduction to bipolar electrochemical deposition. We have previously reported the unique behavior of closed bipolar systems, in which oxidation at one end of an insulated bipolar electrode is directly coupled to reduction at the other, allowing the reaction rate to be monitored by observing the faradaic current.[136,137] Therefore, once the deposited gold blocks the entire channel diameter, it acts as a bipolar electrode in the presence of a closed circuit, with $AuCl_4^-$ reduced at the cathodic end of the wire and BH_4^- oxidized at the anodic pole. Since the spontaneous battery potential of 1.2 V results in a growth

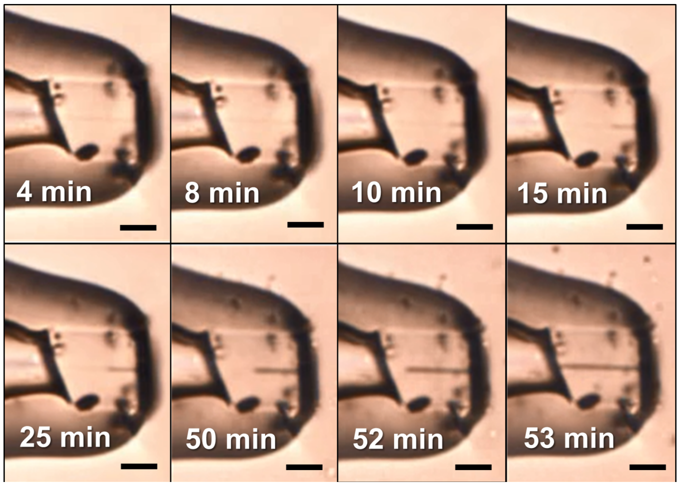

FIGURE 2-5: Control experiment performed in a 271-nm-diameter channel according to the setup shown in Figure 2-2 but with the two Ag/AgCl electrodes connected only with a wire (no potentiostat). Optical microscope images of wire growth are shown at different time points during the deposition. Growth proceeds in a much slower and more controlled manner than for the case without an external electrical connection (Figure 2-4), indicating that having an external pathway for electrons to flow actually changes the initial mixing behavior. As growth proceeds and the end of the wire nears the $AuCl_4^-$ solution, the growth rate increases due to decreased mass transport resistance (similar to Figure 2-3 and Figure 2-7.

rate that is often too fast to produce a high-quality wire, we apply the independent external potential in a direction contrary to the battery potential to decrease this driving force and reduce the deposition rate. The total potential across the gold wire is thus the difference between these two potential sources. In order to maintain electroneutrality, oxidation of Ag must occur at the Ag/AgCl working electrode to balance the reduction of $AuCl_4^-$ at the cathodic end of the growing gold wire. Likewise, reduction of Ag^+ must occur at the Ag/AgCl reference electrode to balance the oxidation of BH_4^- at the anodic end. Therefore, the working electrode should record a positive faradaic current as deposition proceeds. The current trace in Figure 2-3 confirms that this is the case, showing a small positive current of ~ 6 pA as growth continues after the channel is initially blocked.

To further verify that gold deposition can occur by the described bipolar mechanism without physical contact between the metal precursor and the reducing agent, we performed a control experiment mimicking the setup in Figure 2-2, but with two changes: the $AuCl_4^-$ and BH_4^- solutions were placed in two separate beakers, and the two ends of the growing gold nanowire were represented by two glass-sealed Pt nanoelectrodes (one in each solution) connected to each other with a wire (Figure 2-6). Electrochemical measurements and SEM images confirm that when a potential was applied across the two Ag/AgCl electrodes, gold was deposited on the Pt nanoelectrode in the $AuCl_4^-$ solution even though it was not directly connected to the potentiostat, demonstrating that deposition occurred via a bipolar mechanism.

We can calculate the amount of gold deposited and the deposition rate for the channel

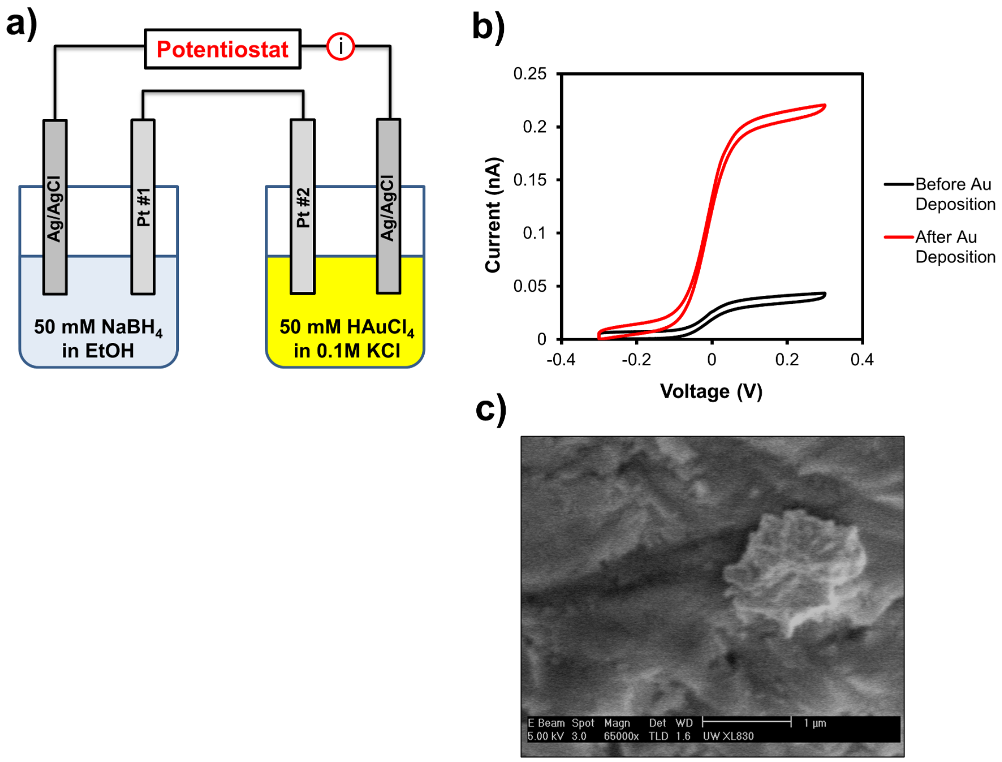

FIGURE 2-6: (a) Diagram of the experimental setup for a control experiment performed with the $HAuCl_4$ and $NaBH_4$ solutions in two separate beakers to prevent chemical reduction by solution mixing. Each beaker contained one Pt nanoelectrode (Pt #1 = $\sim$ 373 nm diameter, Pt #2 = $\sim$ 275 nm diameter) and one Ag/AgCl electrode, creating two electrochemical cells which were connected in series to mimic our nanochannel setup in Figure 2-2, with the two Pt nanoelectrodes representing the two ends of the growing gold nanowire. When a negative potential (between -0.4 V and -0.6 V) was applied to the Ag/AgCl electrode in the $HAuCl_4$ solution for 1 h, gold was deposited on Pt #2 even though it was not directly connected to the potentiostat, confirming that growth proceeds by a bipolar mechanism, with gold reduction on Pt #2 coupled to borohydride oxidation on Pt #1. (b) Cyclic voltammograms of Pt #2 in 1 mM ferrocenemethanol in 0.1 M phosphate buffer at pH 7.4 before (black) and after (red) deposition at a scan rate of 20 mV/s. The diameter of the electrode after deposition was calculated to be 1.6 μm (approximating the geometry as a disk). (c) SEM image of Pt #2 after gold deposition, verifying that it matches the size calculated from the CV in (b). Pt nanoelectrodes were fabricated according to the process described in our previous publication.[158]

shown in Figure 2-3 using Faraday's law, which states the relationship between the total charge passed Q and the number of moles of material deposited N:[88]

$$Q = nFN \tag{2.3}$$

where n is the number of electrons transferred per redox molecule and F is Faraday's constant. The value of Q can be obtained by integrating the current-time curve in Figure 2-3 over just the bipolar electrodeposition phase and can be used to calculate the moles of deposited gold N. Taking into account the dimensions of the channel, this number can then be converted into an

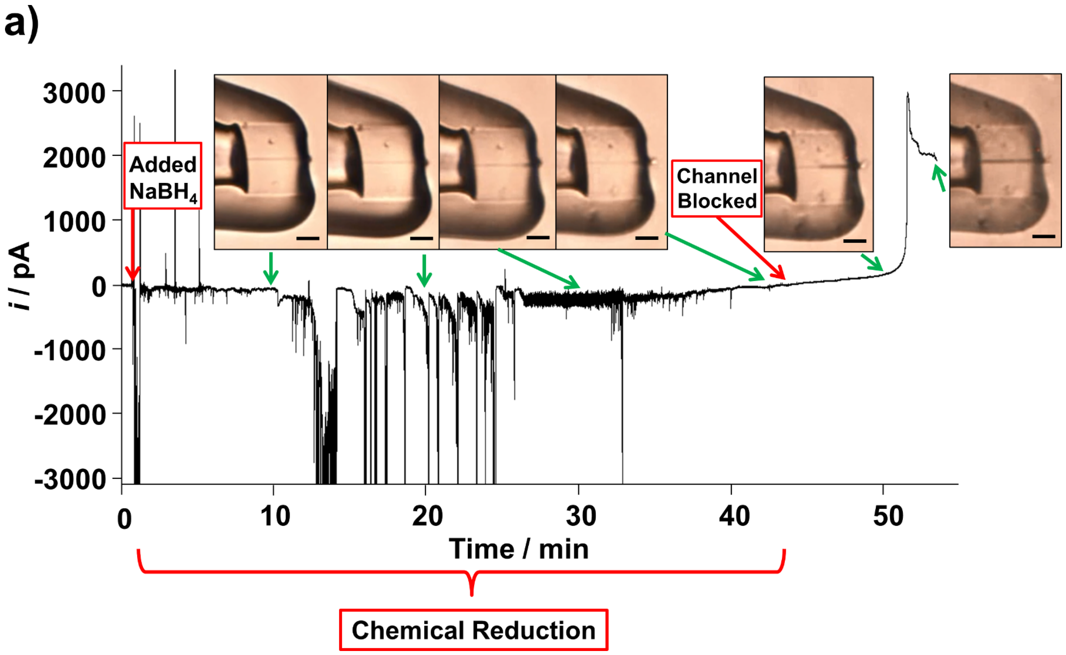

FIGURE 2-7: (a) Current-time trace and corresponding optical microscope images of a control experiment performed in a 394-nm-diameter channel using the same setup shown in Figure 1 but with no adjustment of the applied potential during the growth process. The ionic current increases after NaBH$_4$ is added due to completion of the circuit. Transient current events are most likely due to newly-formed particles passing through the channel. Eventually the channel is blocked and the current decreases to zero, after which bipolar electrodeposition begins. The faradaic current increases substantially as the end of the wire approaches the bulk AuCl$_4^-$ solution due to decreased mass transport resistance, resulting in rapid growth that reaches a maximum rate of 863 nm/s. (b, d-e) SEM images of the wire: (b) before cutting, showing the hollow channel opening. (d-e) after the first (d) and second (e) FIB cuts at the approximate locations indicated in (c). The wire does not become solid until the second bipolar growth mechanism takes over. All scale bars are 10 μm unless otherwise indicated.

equivalent length and compared to the optical measurement of the channel length filled with gold during this time period. In order to make a more accurate optical comparison, we have chosen to analyze a slightly shorter time period within the bipolar electrodeposition phase, in which the starting and ending points of wire growth are clearly visible. Approximating the current as a constant value of 6 pA and integrating from 30 to 127 min gives 1.21 x 10^{-13} moles of deposited gold. This value can be converted into an equivalent volume using the density of gold and then an equivalent length by diving by the cross-sectional area of the channel. Thus, the length of gold deposited in the channel based on the faradaic current is calculated to be 18.2 μm, giving an average deposition rate of 3.1 nm/s. This length calculation agrees well with the value of 19.6 μm determined optically. The small discrepancy is likely due to the error associated with approximating the current as a constant value and error from the optical measurements, which are limited by the resolution of the microscope. In addition to the average growth rate determined above, an instantaneous linear growth rate can be calculated from the faradaic current at any point during the deposition, providing insight into the growth conditions at that particular moment. For example, at 60 min the current is 5.7 pA or 5.7 x 10^{-12} C/s, which can be used to calculate a volumetric rate and then divided by the cross-sectional area of the channel to give an instantaneous deposition rate of 3.0 nm/s. Therefore, recording the faradaic current allows the growth rate to be directly monitored and adjusted in real time.

As deposition proceeds and gold fills the channel, the mass transport resistance of the $AuCl_4^-$ ions decreases due to the diminishing distance between the bulk $AuCl_4^-$ solution and the recessed deposition site. Consequently, the enhanced migration of $AuCl_4^-$ ions results in an increased growth rate. This is observed in the control experiment performed using the same setup shown in Figure 2-2 but with no adjustment of the applied potential during the growth process (Figure 2-7), which shows a substantial increase in current as the growing wire nears the end of the channel, reaching a peak growth rate of 863 nm/s. Therefore, in order to maintain a constant deposition rate, the externally applied potential must be continually increased in opposition to the battery potential to reduce the effective potential at the growing wire and slow down the transport kinetics, as illustrated in Figure 2-3. It should be noted that this potential is controlled manually. While ideally a constant current would be maintained by galvanostatic control during this phase, our setup does not possess the capability to switch between potentiostatic (needed for the initial chemical reduction stage) and galvanostatic modes without first stopping the potentiostat to switch the settings, which could result in uneven growth and defects during this transition period.

We have further demonstrated this *in situ* control over the deposition rate by performing an experiment in which we intentionally changed the external potential by a significant amount in either direction several times during the growth process, causing large increases or decreases in the corresponding deposition rate and confirming that this externally applied potential can be used to dynamically tune the growth rate (Figure 2-13).

Wire growth is monitored under the microscope until it reaches the end of the channel. As we have shown in our previous papers on bipolar electrochemistry,[136, 137] for electrochemical applications it is advantageous to allow the inner surface of the gold wire to grow well beyond the end of the channel, as this increased size will help ensure that the current is limited by reactions occurring at the outer surface of the wire. This deposition method can also be used to fabricate other metal nanowires, as we have demonstrated for platinum (Figure 2-14 in the Supporting Information).

Characterization by Microscopy and Cyclic Voltammetry

Optical microscope images of the finished wire are shown in Figure 2-8. The gold wire spans the entire length of the channel and appears solid throughout. An SEM image of the outside surface of a wire deposited under the same conditions is shown in Figure 2-9a. The unique gold structure reveals the initially disordered chemical reduction that occurs at the interface between the $AuCl_4^-$ and BH_4^- solutions. In order to further investigate the morphology and

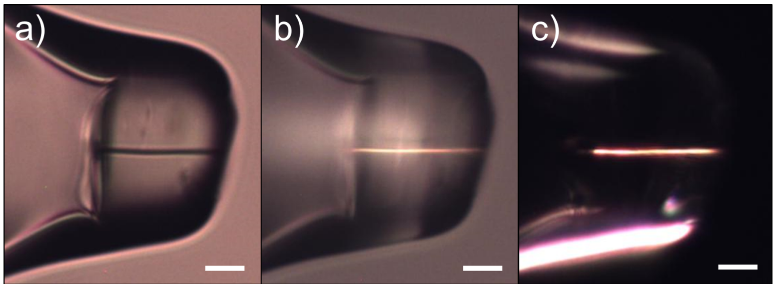

FIGURE 2-8: Optical microscope images of the completed wire from Figure 2-3: (a) bright-field, (b) reflectance, and (c) pseudo dark-field. All scale bars are 10 μm.

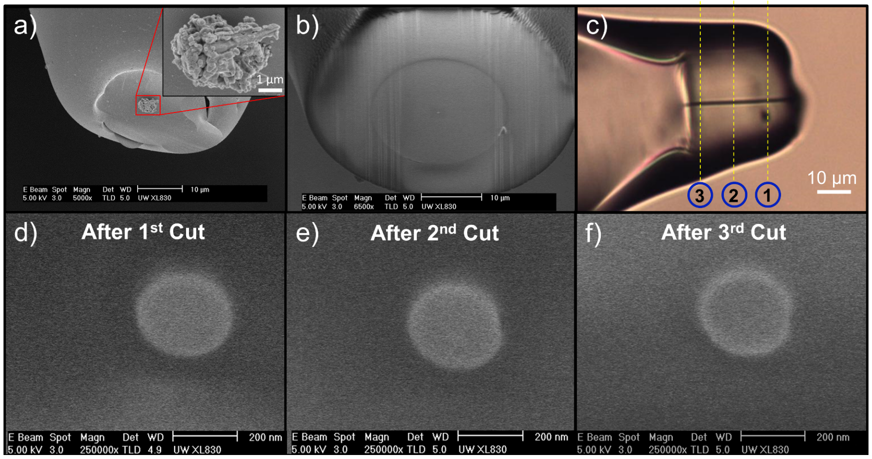

FIGURE 2-9: SEM images of a completed gold wire: (a) before cutting, showing the outer portion of the wire formed by chemical reduction. (b) after cutting. (d-f) cross-section images after the first (d), second (e), and third (f) FIB cuts at the approximate locations indicated in (c), confirming that the wire is solid and maintains good contact with the glass throughout its length.

integrity of the wire, focused ion beam (FIB) milling was used to cut cross-sections at three different points along the finished wire. These three locations and the corresponding SEM images of the cross-sections are shown in Figures 2-9b-f. These images confirm that the wire is solid and maintains good contact with the glass throughout its length.

It is interesting to note that the gold fills the entire channel diameter rather than propagating along the direction of the electric field from a single cross-sectional point, as has been observed in previous reports of open bipolar electrodeposition at conductive metal spheres and rings.[123,201] We believe that the primary difference lies in the profile of the deposition surface. In contrast to the curved deposition surfaces used in this prior work, we suspect that the profile of our growing nanowire surface is relatively flat due to the slow growth rate and the confinement of the template, which promotes some degree of adhesion between the gold and the glass. While the strength of the electric field will vary along the length of the channel, affecting the movement of ions within the channel to some degree, it should be fairly constant across the diameter at any given point. Consequently, the potential should be relatively uni-

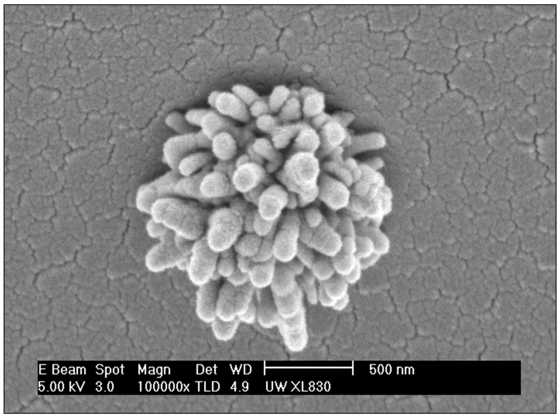

Figure 2-10: SEM image of the outside cap that grows on top of the wire after reaching the end of the nanochannel, shown for a wire deposited with the positions of the $AuCl_4^-$ and BH_4^- solutions reversed (BH_4^- inside the supporting capillary and $AuCl_4^-$ outside). This reversal ensures that the initial disordered portion of the wire formed by direct chemical reduction is located on the inside of the nanochannel, while the section formed by controlled bipolar electrodeposition continues through to the outside, where it can be easily imaged. The ordered arrangement of many smaller wire-like caps in the image indicates that the wire is probably high-quality polycrystalline.

form at either end of the wire along the anodic and cathodic surfaces, respectively, allowing gold to fill the entire cross-section.

While we were unable to obtain TEM images of the wire due to the thick surrounding glass, Karim and coworkers have noted that the type of cap that grows on top of the wire after it reaches the end of the confined nanochannel is indicative of wire crystallinity.[46] Figure 2-10 shows an SEM image of the cap grown on a wire via bipolar electrodeposition when the BH_4^- and $AuCl_4^-$ solution locations were reversed (in order to move the porous part of the wire formed by chemical reduction to the inside of the nanochannel and allow the section formed by controlled bipolar electrodeposition to grow through to the outside for easy imaging). Since the cap consists of an ordered collection of smaller wire-like protrusions rather than a single crystal, the nanowire is probably high-quality polycrystalline. However, this does not undermine its usefulness, and the crystallinity could likely be improved with further optimization.

Gold is a desirable electrode material because it is relatively inert but easy to functionalize for applications that require surface modification. However, it is difficult to fabricate single gold nanoelectrodes due to the challenge of establishing electrical contact and the low melting point of gold, which makes traditional laser-pulling methods used to fabricate platinum nanoelectrodes difficult.[94] Our method is therefore an excellent way to produce gold nanoelectrodes. For a closed bipolar system, in which the nanowire is electrically insulated as it is here, all of the current in the system is carried through the nanowire. Therefore, the measured current can be directly and quantitatively correlated to reactions occurring at the nanowire itself. This is in contrast to an open bipolar system, in which the nanowire is surrounded by an electrolyte solution, and the measured current is a combination of the faradaic current carried

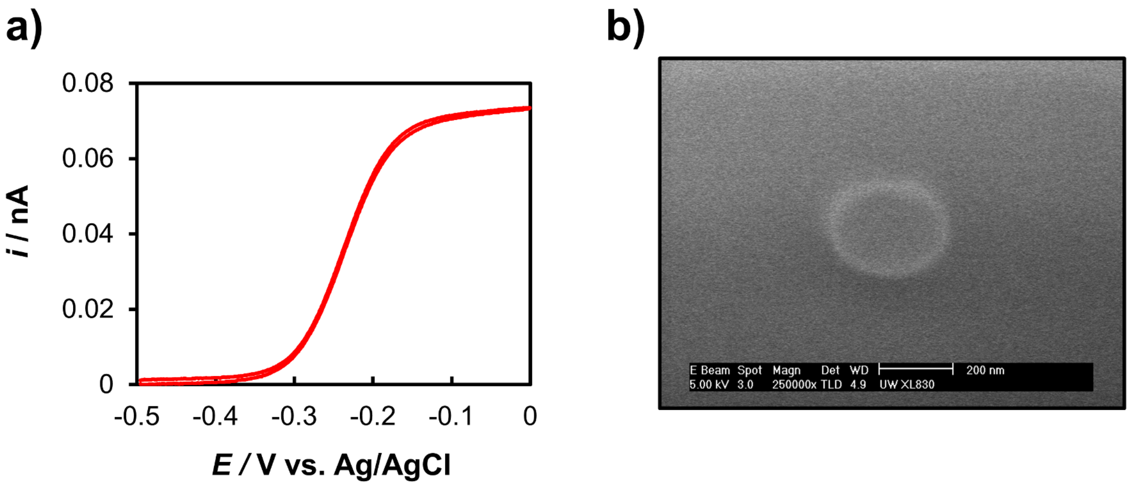

FIGURE 2-11: Demonstration of a deposited gold wire functioning as a bipolar nanoelectrode. (a) Cyclic voltammogram of the nanowire electrode in 2 mM ferrocenemethanol in 0.1 M phosphate buffer, pH 7.4 at a scan rate of 10 mV/s. The inside of the supporting capillary was filled with 10 mM ferricyanide in 0.1 M phosphate buffer, pH 7.4. (b) Corresponding SEM image of the cross-section confirming the 274 nm diameter calculated from the steady-state limiting current in (a).

through the wire and the ionic current carried through the open solution.[110]

Cyclic voltammetry was performed to demonstrate the ability of the insulated gold wire to function as a bipolar nanoelectrode. The supporting pipette was filled with 10 mM ferricyanide in 0.1 M phosphate buffer at pH 7.4, while the outside was immersed in 2 mM ferrocenemethanol in 0.1 M phosphate buffer at pH 7.4. As we have discussed in our previous reports, provided that the current is sufficiently limited by one pole of the electrode (through either ample area or concentration differences between the two poles), there are no functional limitations to the closed bipolar setup, and a bipolar electrode can be used in the same way as a traditional electrode. Since the inner face of the wire described here has a larger surface area and is in contact with a higher concentration redox solution, the current is limited by the oxidation of ferrocenemethanol at the outer surface. A cyclic voltammogram (CV) is shown in Figure 2-11, along with the corresponding SEM image of the electrode after FIB cutting. The electrochemical response is identical in shape and current magnitude to that expected from a traditional electrode. The radius of the electrode can be calculated using the equation for the steady-state current i_{ss} at a disk ultramicroelectrode:[88]

$$i_{ss} = 4nFDC^{*}r \tag{2.4}$$

where n and F are previously defined, D is the diffusion coefficient (6.7 10^{-6} cm^2/s for ferrocenemethanol),[137] C^{*} is the bulk concentration of the redox species, and r is the electrode radius. A steady-state limiting current of 73.5 pA corresponds to an electrode diameter of 274 nm, which matches well with the 279 nm diameter measured from the SEM image.

The only difference between the electrochemical response of a bipolar electrode and a traditional electrode comes from the position of the half-wave potential $E_{1/2}$ (the potential when the current is half of its steady-state value), which is shifted in a bipolar setup. However, this shift is predictable, meaning that a bipolar electrode can still be used for catalytic studies and other experiments in which results are determined by monitoring the $E_{1/2}$ position. We have previously shown that the $E_{1/2}$ for a closed bipolar electrode shifts depending on the ratio between the anodic and cathodic steady-state limiting currents according to the following equation:[136]

$$E_{1/2} = \left(E_a^{\circ'} - E_c^{\circ'}\right) - \frac{RT}{F} ln \left(-2\left(\frac{i_{ss}^c}{i_{ss}^a}\right) - 1\right) \tag{2.5}$$

where $E_a^{\circ'}$ and $E_c^{\circ'}$ are the formal potentials for the reactions occurring at the anodic and cathodic poles, R is the universal gas constant, T is the temperature, n and F are previously defined, and i_{ss}^a and i_{ss}^c are the maximum possible steady-state limiting currents at the anodic and cathodic poles, respectively. The cathodic current is defined as negative. The values of i_{ss}^a (73.5 pA) and $E_{1/2}$ (-0.24 V) can both be obtained from the CV. Solving for i_{ss}^c in Equation 2.4 gives a maximum cathodic limiting current of -7.0 nA. Since the gold grows outward after reaching the end of the channel, the inner end of the wire can be approximated as a hemisphere rather than a disk, with the steady-state current given by:[88]

$$i_{ss} = 2\pi nFDC^* r \tag{2.6}$$

The limiting current above corresponds to an inner hemisphere diameter of 3 μm, which is reasonable given that it is visible under the microscope. Therefore, we can calculate the diameters of both the outer and inner ends of the wire from a single CV. We have found that running repeated CVs often results in a loss of contact between the wire and the surface of the glass. We don't fully understand the nature of this disconnection, but we are currently working on surface modification procedures to improve adhesion.

2.3.3 Conclusions

We have presented a simple, reproducible method for dynamically controlling the rate of metal nanowire deposition *in situ*. This approach employs a combined chemical/bipolar electrochemical mechanism that does not require a direct electrical connection and is driven by the redox potential difference between solutions of a metal precursor and a reducing agent. When these solutions mix in a confined nanochannel template a short metal nanowire is formed, creating a closed bipolar electrochemical cell that separates the reduction of metal precursor ions at one end of the nanowire from the oxidation of the reducing agent at the other. This bipolar process is monitored in real time by the faradaic current readout and optical microscopy and can be regulated by applying an independently tunable electric field across the nanowire, enabling precise ”wireless” control over the deposition rate. We demonstrated this method by depositing a single gold nanowire in a silica nanochannel template and characterized the resulting wire by SEM and cyclic voltammetry, confirming that it is solid throughout its length and can be used as a bipolar nanoelectrode. The ability to directly monitor and control the deposition rate provides fundamental insight into the dynamics of metal growth under confinement. This procedure could be extended to other electrochemical systems as well and can be further tailored by modifying the template geometry, as the degree of confinement affects transport.[86]

Electrodes fabricated using this method could be easily modified to act as electrochemical sensors for the detection of specific analytes[209,210] or used to study single nanoparticle electrocatalysis if the electrode dimensions could be made sufficiently small.[10,13,211] With additional optimization, this process could also be used to fabricate small diameter tips for scanning electrochemical microscopy (SECM)[3] or nanowire arrays containing a known number of wires (so that the deposition rate could still be accurately monitored and controlled) for quick screening of potential catalysts[133] or use as high surface area sensors.[19,21,23,170] Since it provides a significant degree of control over the location, morphology, and growth rate of the wire without the need for a conductive starting substrate, this technique is particularly beneficial for applications that require precise positioning, such as fabrication of nanowires on a patterned chip for microfluidic electrochemical sensors[212,213] or deposition of metal catalysts used in the synthesis of other inorganic nanowires.[214] In addition, the miniature reaction chamber created by the channel is ideal for studying the confined dynamics of any process that can be optically or electrically monitored.

2.3.4 Methods

Chemicals and Materials

All aqueous solutions were prepared using >18 MΩ•cm water from a Barnstead Nanopure water purification system. Ethanol (Decon Laboratories, Inc., 200 proof), potassium chloride (KCl, Macron Chemicals), sodium chloride (NaCl, JT Baker), potassium ferricyanide ($K_3Fe(CN)_6$, Sigma-Aldrich), ferrocenemethanol (FcMeOH, Sigma-Aldrich), monopotassium phosphate (KH_2PO_4, JT Baker), dipotassium phosphate (K_2HPO_4, JT Baker), chloroplatinic acid (H_2PtCl_6, Sigma-Aldrich), and sodium borohydride ($NaBH_4$, Sigma-Aldrich) were all reagent grade and were used without further purification. Gold (III) chloride ($HAuCl_4$) was purchased from Salt Lake Metals (1 % solution by weight, 99.99 % purity). Silica capillary tubing (o.d. = 1.0 mm, i.d.= 0.3 mm) was obtained from Sutter Instrument Company and silica microcapillaries (o.d. = 0.35 mm, i.d. = 20 μm) from Polymicro Inc.

Nanochannel Fabrication

Nanochannels were prepared according to a previously reported process.[208] Briefly, a small piece of silica microcapillary (o.d.= 0.35 mm, i.d.= 20 μm) was first sealed inside a larger silica capillary (o.d. = 1.0 mm, i.d.= 0.3 mm) using a laser-based micropipette puller (P-2000, Sutter Instrument Company). The diameter of the inner capillary was decreased through a series of heating and cooling cycles under vacuum before the whole ensemble was pulled into two long nanotips. A nanotip was inserted into a larger diameter borosilicate holder pipette under an optical microscope until the end could be seen protruding 5-10 μm from the holder opening. It was then passed very quickly through a natural gas flame to seal a small section to the walls of the holder. The remainder of the tip was broken off and removed, leaving only the small sealed segment containing the nanochannel. The protruding end was cut off under the microscope using a razor blade.

Gold Deposition

After performing resistance measurements in 0.1 M KCl to determine the nanochannel diameter,[208] the supporting pipette was filled with 50 mM $HAuCl_4$ in 0.1 M KCl and inserted into a home-built polycarbonate solution chamber attached to a glass microscope slide. A thin glass coverslip was set on top of the chamber, and two Ag/AgCl electrodes were placed inside of the supporting pipette (designated as the working electrode) and the solution chamber (designated as the reference electrode). Pictures of the solution chamber as well as a more detailed description are given in Figure 2-12 in the Supporting Information section at the end of the chapter. The whole ensemble was then positioned under a 20X microscope objective (Nikon) inside a Faraday cage. A potential of -0.6 V was applied across the open circuit, after which $\sim$ 1 mL of 50 mM $NaBH_4$ in ethanol was slowly added to the solution chamber to initiate the reaction. Although the solution chamber is covered, there is a small area open to the air where the $NaBH_4$ is added. As time proceeds, two things occur: first, ethanol evaporates, and the solution must be replenished; second, bubbles generated by the slow decomposition of $NaBH_4$ in ethanol aggregate to form large bubbles that can cover the channel opening. A dark shadow can be seen in the optical microcope image when the solvent front begins to approach the channel (either from evaporation or a large bubble), indicating the need for more $NaBH_4$ solution to either replenish the solution or dislodge the bubble. The applied potential was adjusted manually to accelerate blockage formation during the initial chemical reduction phase and to maintain a near constant current value during subsequent bipolar deposition. Current-time traces were acquired using an Axopatch 200B high-impedance amplifier (Molecular Devices, Inc.) and a Digidata 1440A digitizer (Molecular Devices, Inc.) interfaced to a Dell computer. A 1.0 kHz low-pass filter was applied to the amplifier during data acquisition, but no further filtering was performed. An optical video was simultaneously recorded with the OCView7 software package using a Nikon Eclipse E600 microscope connected to a CCD camera (OptixCam Summit Series).

Resistance Measurements and Cyclic Voltammetry

Current-voltage responses were measured using a Chem-Clamp potentiostat (Dagan, Inc.) and a PAR 175 universal function generator (Princeton Applied Research). The potentiostat was interfaced to a Dell computer through a PCI-6251 data acquisition board (National Instruments) via a BNC-2090 analog breakout box (National Instruments). The data was recorded using a custom program written in LabView 8.5 (National Instruments). All measurements were conducted inside a Faraday cage in a one-compartment, two-electrode cell with a Ag/AgCl working electrode inside the supporting pipette and a Ag/AgCl reference electrode in the outside solution.

Focused Ion Beam and Scanning Electron Microscopy

Focused ion beam milling and SEM imaging were performed using a FEI XL830 dual beam FIB/SEM instrument.

2.3.5 Supporting Information

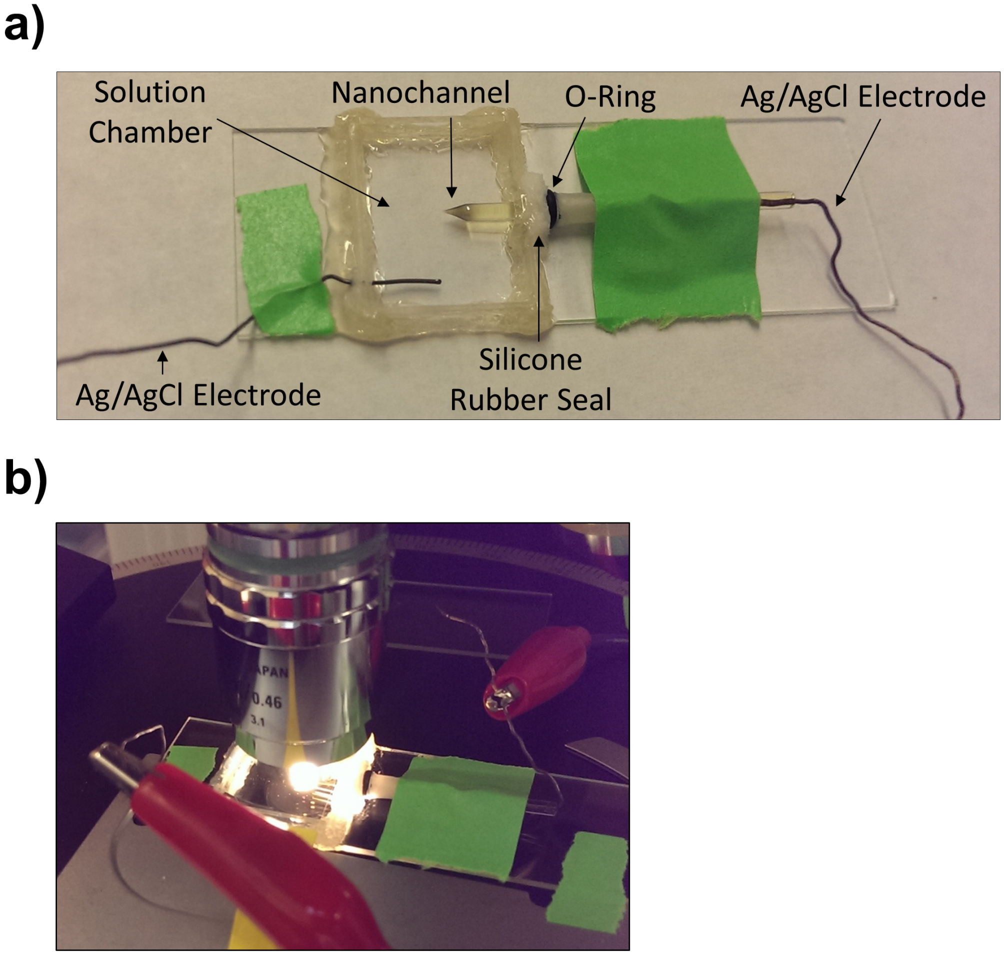

FIGURE 2-12: Pictures of the home-built polycarbonate solution chamber used for deposition (a) and the microscope setup (b). The chamber measures 2.5 cm x 2 cm x 0.3 mm and is secured to a glass microscope slide using epoxy. A small rubber O-ring is placed around the supporting pipette of the nanochannel, which is then inserted into the chamber through a hole surrounded by silicone rubber and secured in place using tape. The O-ring and silicone rubber form a seal around the pipette. A Ag/AgCl working electrode is positioned inside the pipette, and a Ag/AgCl reference electrode is poked through a small, silicone rubber-filled hole in the chamber wall to contact the solution inside. A glass coverslip is placed over the top of the chamber, leaving a small opening at the corner for solution filling, and the whole ensemble is positioned under the microscope for observation.

Figure 2-13 shows a control experiment in which the externally applied potential was intentionally changed by a significant amount in either direction to further demonstrate dynamic control over the deposition rate. After the channel is blocked, the potential is decreased from -0.6 V to -0.3 V, which increases the overall potential at the wire surface (because it is applied in opposition to the natural battery potential as diagramed in Figure 2-2b) and results in a current increase, reaching a maximum growth rate of 26 nm/s. The growth can be seen in the

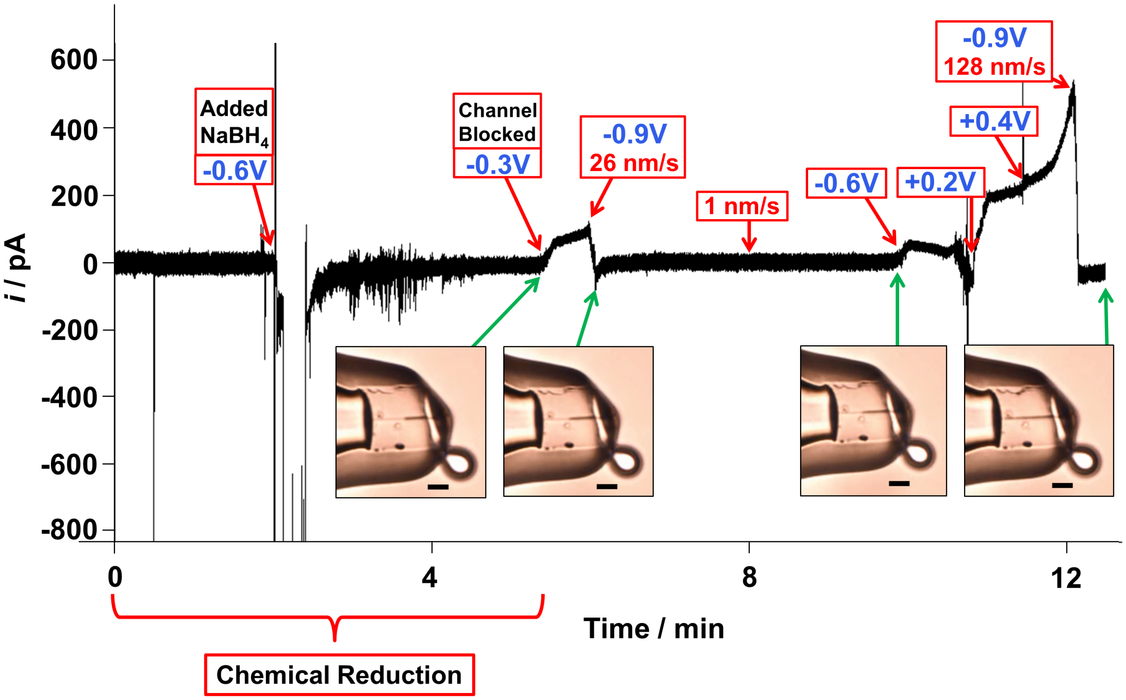

FIGURE 2-13: Control experiment in which the externally applied potential was intentionally changed by a significant amount in either direction to further demonstrate dynamic control over the deposition rate. All other experimental parameters were the same as described in Figure 2-2. The voltage values represent the external potential applied at the indicated times. Calculated deposition rates and optical microscope images of wire growth are shown for different time points during the deposition. The small oval shape connected to the nanochannel pipette visible in the optical images is a piece of glass left over from the fabrication process. The large 429 nm channel diameter allows for faster solution mixing, which decreases the overall blockage time but results in a greater section of initial growth before the channel is blocked. Changing the externally applied potential after the channel is blocked causes a corresponding response in the measured current and deposition rate by either increasing or decreasing the effective potential at the growing nanowire surface. All scale bars are 10 μm.

optical microscope images, which show a noticeable amount of deposition in only 43 s. The potential is then increased to -0.9 V, causing an immediate decrease in the current and leading to a much slower growth rate (1 nm/s). The images show that even after 3 min 45 s, the wire has hardly grown at all. The potential is then switched to -0.6 V, causing the current to rise briefly before decreasing again. This decrease is likely due to the large amount of time previously spent at -0.9 V, which causes migration of BH_4^- toward the positively charged reference electrode and away from the nanowire surface. Consequently, the BH_4^- battery concentration is probably fairly depleted by this point and cannot keep up with the higher deposition rate. Therefore, for a brief time the spontaneous battery potential largely disappears, causing temporary oxidation at the end of the nanowire in the $AuCl_4^-$ solution and resulting in a negative current (due to the negative potential being applied to the corresponding working electrode).

However, when the external potential is changed to +0.2 V and then +0.4 V, the concentration balance is restored, and the current begins to rise dramatically (because the external potential is now applied in the same direction as the battery potential), hitting a maximum deposition rate of 128 nm/s before it is switched back to -0.9 V, which again causes a large decrease in both the current and the deposition rate. In all cases, changing the externally applied potential causes a corresponding response in the measured current and deposition rate by either increasing or decreasing the effective potential at the growing nanowire surface. This shows that the deposition rate can be controlled *in situ* simply by changing the externally applied potential.

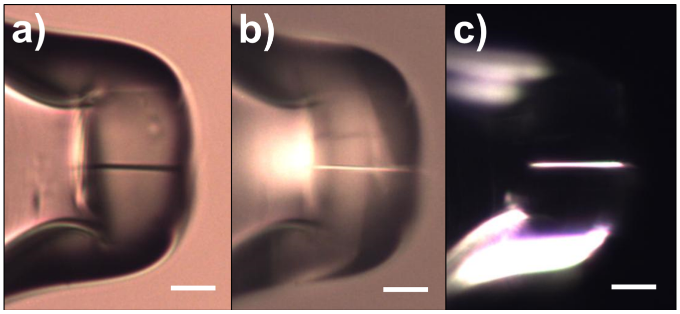

FIGURE 2-14: Optical microscope images of a platinum nanowire grown in a-356-nm diameter channel using the same setup shown in Figure 2-2 but with 50 mM H_2PtCl_6 in 0.1 M NaCl as the metal salt: (a) bright-field, (b) reflectance, and (c) pseudo dark-field. All scale bars are 10 μm.

CHAPTER 3

Anomalous Particle Transport Behavior in Silica Nanochannels

3.1 Introduction

EFFICIENT TRANSPORT behavior is critical to many different nanoscale systems and applications, including biological membranes, separations, geochemistry, and energy storage. These systems are complex, as transported species traveling through a porous network are simultaneously influenced by multiple different driving forces and interactions with the surrounding environment. These effects become increasingly pronounced under confinement, when the size of the transported species approaches the size of the pores. Therefore, understanding and controlling these nanoscale properties and interactions has become increasingly important, not only for gaining a better fundamental understanding of which factors govern transport in systems such as those mentioned above, but also for designing more tailored and tunable transport systems in the future.

Models for particle transport through fluids are typically based on either pressure-driven flow, where the particles are transported along with the fluid due to a pressure gradient, or voltage-driven flow, where the particles are transported through the fluid under the influence of an electric field. The simplest selection parameter for transport through a porous membrane is size. Conventional separation membranes function by excluding analytes whose size is greater than the pores of the membrane.[215] Additionally, reverse size selection can be accomplished by using techniques such as size-exclusion chromatography,[216] in which smaller particles are trapped in a porous network while larger particles, unable to fit into these small pores, are free to continue through the channel. Other methods of controlling transport are more sophisticated and specific, taking into account more intrinsic nanoscale properties such as charge,[60,63,65,215,217,218] polarity,[83] or chemical specificity.[60,77,217,219–222] However, most of these more specific methods require time-consuming modification of the pore surface, preventing the membrane from being used afterwards for other analyses and limiting the versatility of the setup.

Resistive-pulse sensing is a widely-used electroanalytical method for particle detection based on the Coulter counter technique developed in the 1950s.[223] In this method, a potential is applied across a single nanometer-sized pore or channel in an insulating material separating two electrolyte solution chambers. The ionic current through the channel is measured as a function of time and is partially blocked when a particle passes through, causing a temporary decrease or pulse in the current readout which can give information about the particle size and behavior inside the channel. The lasting popularity of this technique can be attributed to its simple design, label-free nature, potential portability, and sensitivity to individual particles. Many studies have used this method to distinguish analytes based on size[33–37,224] or charge,[33,40–42,75,225] as the pulse amplitudes and widths are reflective of these properties. Others have employed this technique to explore the relative roles of different driving forces,[33,36,75,80,226,227] showing that the interplay between pressure, electrophoresis, and electroosmosis can have a considerable effect on particle transport direction and velocity. However, most of these examples focus on how different parameters affect particle velocities without exploring how they affect particle entrance frequencies. Nevertheless, there have been a few reports examining entrance frequencies, and several have found anomalous behavior that cannot be explained using existing models, including lower than expected detection frequencies[33,36,78] and selective transport.[34,35,227] Some reports have proposed more subtle explanations for this unusual transport behavior, suggesting that electrostatic interactions or inhomogeneous charge distribution on the analyte surface or pore wall[34,75,77,78,80,81,228] may be affecting particle transport.

Indeed, it has been shown that these types of local, short-ranged nanoscale interactions play a significant role in controlling transport in molecular-scale nanochannels,[56,77,86,229–231] where the channel diameter is on the same order of magnitude as the size of the ions or molecules, and can lead to very interesting, non-intuitive transport phenomena. For example, several studies have reported cation-selective behavior[55,58,232] as well as significantly enhanced transport rates of ions in carbon nanotubes,[54,233] whereas others have observed solute depletion or enrichment under the influence of an electric field, which can result in interesting ion transport effects[61,234,235] that behave like a nanofluidic transistor.[71–73] While these types of interactions are usually considered to be short-ranged, Valtiner and coworkers have shown that they can extend much further than previously thought[236] ($\sim$ 100 nm) and may therefore be applicable to larger scale systems as well. Therefore, although most resistive-pulse systems are much bigger than these molecular-level transport examples, similar transport phenomena may still be relevant.

In this work we show that subtle nanoscale effects can have a profound influence on mesoscale transport behavior when the particle diameter approaches the size of the channel diameter. We investigated the transport of nanoparticles through a single silica nanochannel using resistive-pulse sensing and observed anomalous transport selectivity that is dependent on both particle size and material. When two different silica particle sizes are present in equal concentrations in solution, smaller particles are detected more frequently than larger ones, as expected from geometric restrictions. However, when the particle material is switched to polystyrene the opposite selectivity is exhibited, with larger particles passing through the channel much more frequently. To further investigate this unexpected behavior, we explored the influence of various experimental factors and material properties on particle entrance and transport, beginning with simple driving forces before focusing on more nanoscale interactions. We found that simple transport models do not explain this unusual selectivity, and it appears to be due instead to more subtle charge-related effects. These could be the result of dynamical charge properties, such as polarization of the particle or solvation environment or hydrophilic/hydrophobic interactions that are dependent on the surface chemistry and properties of the different materials. These effects could be leveraged to achieve custom control over nanoscale transport and demonstrate the importance of considering nanoscale effects in the prediction of mesoscale transport behavior.

3.2 Results and Discussion

3.2.1 Data Collection and Analysis

Particle detection measurements were carried out with a cylindrical-shaped silica nanochannel positioned inside a custom-built pressure cell, as shown in Figure 3-1. A potential of 1 V was applied to a Ag/AgCl working electrode inside the supporting capillary of the nanochannel with respect to a Ag/AgCl reference electrode in the solution chamber. The ionic current through the nanochannel was monitored as particles were driven through at an applied pressure of 1 psi.

Figures 3-2 a and b show a typical current-time trace for a 416-nm-diameter nanochannel (L=13 μm) in a solution of 0.1 M KCl and 0.1% Triton X-100 containing equal concentrations of 175 nm and 356 nm polystyrene particles (8.9×10^9 particles/mL). As a particle passes through the channel, it blocks some of the ionic current, producing a temporary square-shaped current pulse, which can be correlated to its size and behavior inside the channel. The particle diameter d_s is proportional to the amplitude of the current pulse Δi_c and can be calculated using equations described previously:[40]

$$\frac{\Delta i_c}{i_c} = S\left(d_c, d_s\right) \frac{d_s^3}{l_c' d_c^2} \tag{3.1}$$

where i_c is the baseline current, d_c is the channel diameter, and l_c' is the channel length corrected for the end effect, given by $l_c' = l_c + 0.785 d_c$. The correction factor $S\left(d_c, d_s\right)$ is dependent on the ratio of d_s to d_c:

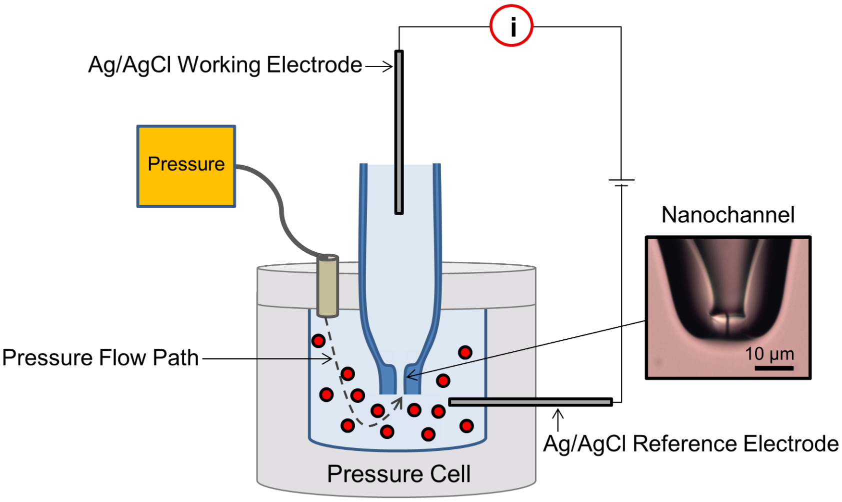

FIGURE 3-1: Diagram of the setup used for particle detection experiments. The ionic current through a nanochannel is monitored as nanoparticles are driven into the channel by an external pressure of 1 psi. As a particle passes through, it causes a temporary drop in the ionic current, which can be recorded and analyzed to give information about particle size and behavior. Typically, a potential of 1 V is applied to the Ag/AgCl working electrode inside the channel relative to the Ag/AgCl reference electrode inside the sample chamber.

$$S\left(d_c, d_s\right) = \frac{1}{1 - 0.8\left(\frac{d_s}{d_c}\right)^3} \tag{3.2}$$

The particle size distribution histogram for this current-time trace is plotted in Figure 3-2c and was fitted with a Gaussian function for further analysis. Two particle size populations are clearly observed, with peak 1 corresponding to the 175 nm particle size and peak 2 to the 356 nm particle size. The difference between the observed and nominal particle sizes is most likely due to swelling of the polystyrene particles in solution, as DLS measurements of the hydrodynamic diameters match our observed sizes. The smaller peak around 260 nm corresponds to small aggregates of 175 nm particles and was not used in the analysis. While these aggregates will result in a slightly lower concentration of single 175 nm particles in solution than was initially added, minor aggregation was detected in all samples, and thus the comparison trends observed are valid even if the absolute values might be slightly affected.

Three characterization parameters can be extracted from the data to give a thorough description of particle behavior. By investigating how each of these parameters varies with changing experimental conditions, we can gain a more comprehensive understanding of which factors are contributing to size selectivity. We looked at the following parameters for each particle size: (1) the detection frequency f, given by the number of particles/s and calculated by integrating each peak from the size distribution histogram and dividing by the total time; (2) the translocation time t, or the amount of time it takes for the particle to travel through the

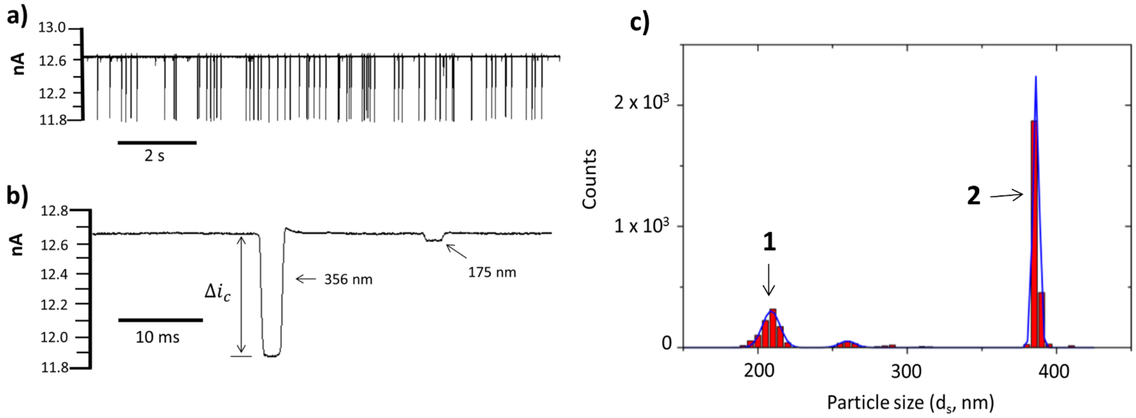

FIGURE 3-2: a) Typical current-time trace for a 416-nm-diameter nanochannel (L=13 μm) in 0.1 M KCl and 0.1 % Triton X-100 containing equal concentrations of 175 nm and 356 nm PS particles (8.9×10^9) at an applied voltage of 1 V and an applied pressure of 1 psi. b) Close-up of detection events from a) representing both particle sizes. The pulse amplitude Δi_c can be used to calculate the particle size. c) Particle size distribution histogram for the current trace in a). The Gaussian fit is indicated by the blue line and was used to extract the relative particle detection frequencies by integrating the area under each peak.

channel; (3) the selectivity %, defined as the percentage of total detected particles attributable to each particle size (denoted % small and % large). In addition, when changes in size selectivity were observed, we examined whether differences in the small or large particle behavior were responsible.

3.2.2 Material Dependence

Different particle materials were investigated to determine the effect of material properties on size selectivity. Experiments were performed using two different particle solutions: the first contained 175 nm and 356 nm polystyrene (PS) nanoparticles while the second contained 172 nm and 361 nm silica nanoparticles. Detection of both particle materials was performed with the same channel, enabling a direct comparison of the results without any complicating effects due to channel geometry. Since the sizes of the polystyrene and silica particles are very similar and all other experimental conditions are the same, the only difference between the two cases is the particle material. The three characterization parameters described above are compared for polystyrene and silica particle detection in Table 3.1.

Geometric constraints predict that smaller particles should be detected more frequently since they have a higher number of successful approach vectors to the channel entrance. Therefore, according to geometric arguments, there should be no difference in size selectivity between the two particle materials. We can calculate the predicted selectivity % for each particle size as follows (Figure 3-3a illustrates this theory, based on geometric limitations described by Giddings[237]). When a particle (red circle) enters the channel (blue circle), the minimum

Particles	***Solution***	d_c *(nm)*	***L*** *(μm)*	***% Small***	***% Large***	f_{small} (Part./s)	f_{large} (Part./s)	t_{small} *(ms)*	t_{large} *(ms)*
175 nm PS/ 356 nm PS	0.1 M KCl	604	19	19%	81%	1.7	7.4	2.4 ±0.8	2.6 ±0.2
172 nm Silica/ 361 nm Silica	0.1 M KCl	604	19	83%	17%	23.6	5.0	1.8 ±1.0	2.7 ±0.3

TABLE 3.1: Comparison of characterization parameters for silica and polystyrene particle detection using the same channel.

distance between the center of the particle and the channel wall is equal to the radius of the particle r_s. Thus, as a particle approaches the channel opening only a portion of the channel area is available to the particle for translocation (shaded in yellow). The effective radius of this area is given by $r_{eff} = (d_c - d_s)/2$, where d_c is the channel diameter and d_s is the particle diameter. The effective available area then becomes

$$A_{eff} = \pi \frac{(d_c - d_s)}{2}^2 \tag{3.3}$$

This effective area can be calculated for each particle size. The predicted selectivity % for the small particles (S_{small} %) is simply the ratio of the small particle effective area to the sum of the small particle and large particle effective areas:

$$S_{small}\% = \frac{A_{eff,S}}{(A_{eff,S} + A_{eff,L})} \tag{3.4}$$

Therefore, the expected selectivity % can be calculated for each particle size based on geometric sieving alone.

The silica particles behave as predicted by these arguments, with small particles making up 83% of the total particles detected. This is close to the predicted selectivity percentage of 84% for the small particles. Surprisingly, the polystyrene particles behave oppositely, with *large* particles comprising 81% of the total particles detected—about 3X higher than predicted (25%). Experiments were repeated in over twenty-five channels to confirm the reproducibility of this result, and reverse size selectivity was observed each time. Interestingly, similar transport behavior for polystyrene nanoparticles has been mentioned in a few previous publications. White and coworkers have reported comparable results using a conical glass nanopore, detecting larger 160 nm particles 2.5X more frequently than smaller 80 nm particles.[34] They suggest that this could be due to the size of the particle relative to the pore opening or non-uniform surface charge distributions. Similarly, Fraikin et al. observed higher detection fre-

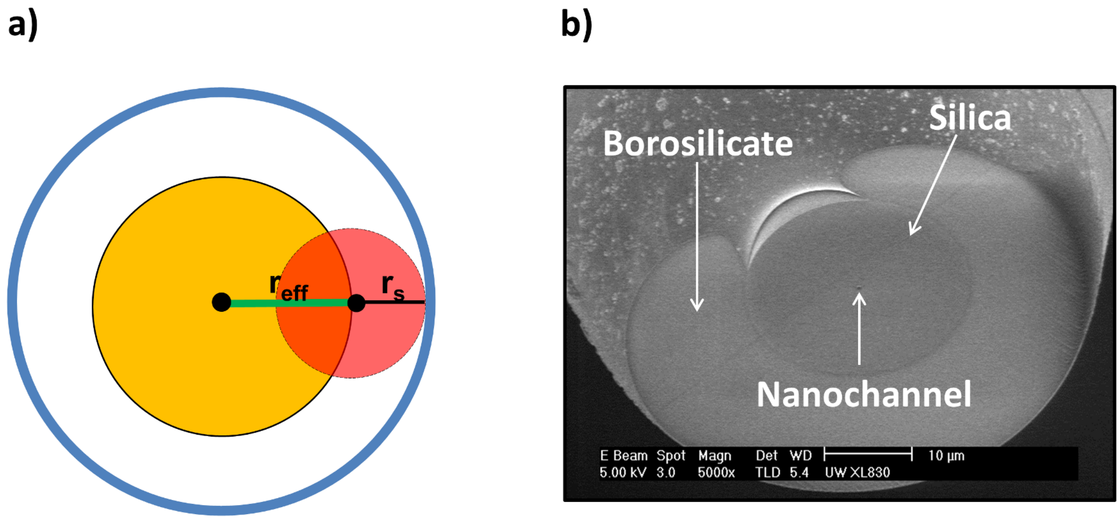

FIGURE 3-3: a) Diagram of geometric restrictions placed on particles when entering a nanochannel of similar size. Based on this theory, the small particles should be detected more frequently due to the higher number of successful approach vectors to the channel entrance. b) SEM image of a nanochannel showing the very large cross-sectional surface area of the glass surrounding the nanochannel entrance.

quencies for 117 nm nanoparticles in a mixture also containing equal concentrations of 51 nm and 75 nm particles using a PDMS nanopore. However, neither of these reports explored this anomalous behavior, as this was not the focus of their work.[35]

Comparing the magnitudes of the detection frequencies in Table 3.1 provides more information about the possible mechanism of this unusual behavior. Although large polystyrene particles are detected slightly more frequently than large silica particles, the majority of the selectivity difference between the two materials can be attributed to changes in the small particle behavior, as the small polystyrene particles are detected ~14X less frequently than the small silica particles. Three important conclusions can be drawn from these comparisons. First, selectivity is not based solely on particle size. Second, it is strongly dependent on the particle material, indicating that the chemical identity of the particle plays a key role. Third, most of the selectivity difference between the two particle materials is due to the inhibited entrance of the small polystyrene particles relative to the small silica particles.

Analyzing the translocation times reveals another significant finding. The translocation times for both sizes of polystyrene particles are nearly identical, meaning that once they enter the channel, pressure pushes them through at the same rate. Consequently, we can conclude that selectivity must occur *outside* the channel, which narrows down the possible mechanisms. The small silica particles, on the other hand, actually travel through the channel ~1.5X faster than the large silica particles, indicating that the pressure force is unable to overcome the selectivity mechanism as successfully as it does for polystyrene. This suggests that there may be differences between the mechanisms of selectivity for the two particle materials. This could be related to the additional driving force provided by the applied voltage. As we will show, voltage should have the same effect on the large particles of both materials due to their similar charges but should have a stronger effect on the small silica particles relative to the small polystyrene particles, which could be contributing to the observed differences.

In order to better understand the origin of this unusual selectivity, we explored possible contributions from several different factors. We will first discuss the relevance of the simple driving forces present in our system before examining the significance of more subtle nanoscale effects, including competition dynamics, charge-related factors (electrolyte concentration, solvent dependence, surfactant, and pH), and temperature. The three primary driving forces are diffusion, pressure, and voltage, and the relationship between size selectivity and each of these is addressed below.

3.2.3 Diffusion

Diffusion of particles through the fluid is expected to be only a minor driving force relative to the other two and should be most relevant in the bulk solution, where the electric field and pressure forces are weak relative to their magnitudes inside the channel. Diffusion of a sphere through a liquid is described by the Stokes equation:[61]

$$D = \frac{k_B T}{6\pi\eta R} \tag{3.5}$$

where k_B is the Boltzmann constant, T is the temperature, η is the viscosity of the fluid, and r is the radius of the sphere. According to this equation, small particles should diffuse faster than large ones, which would aid small particle entrance into the channel rather than hinder it as is observed for polystyrene. Thus, diffusion can be ruled out as a primary factor for determining selectivity. The roles of the other two main driving forces, pressure and voltage, are examined in greater detail below.

3.2.4 Polystyrene Pressure Dependence

Pressure-driven flow is expected to be the primary driving force under our experimental conditions. As shown in Figure 3-4, pressure-driven flow inside a cylindrical channel is parabolic, with the fluid moving fastest in the middle of the channel and slowest near the walls.
The relationship between volumetric fluid flow Q, pressure, and channel geometry is given by the Hagen-Poiseuille equation for fluid flow through a cylindrical tube:[90]

$$Q = \frac{\pi d_c^4 \Delta P}{128\eta L} \tag{3.6}$$

where d_c is the channel diameter, ΔP is the pressure difference between the two ends of the channel, η is the solvent viscosity, and L is the channel length. In order to better exam-

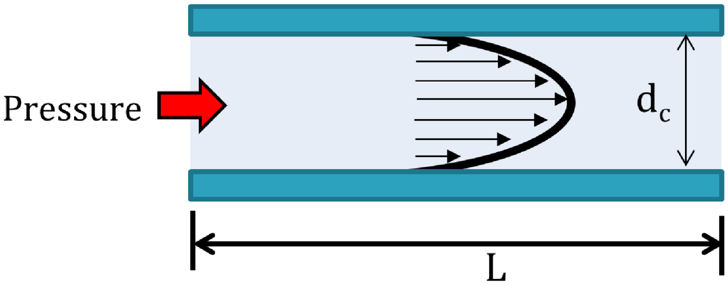

FIGURE 3-4: Parabolic flow profile for pressure-driven flow in a cylindrical channel (Poiseuille flow). The fluid velocity is highest in the center of the channel and assumed to be zero near the walls due to friction forces.

ine the role of pressure in determining particle behavior and size selectivity, we compared the experimentally-determined detection frequencies and translocation times to the predicted Poiseuille behavior. Due to the small dimensions of nanochannels, Poiseuille flow is fully developed at the channel entrance,[61] which allows this equation to be used to predict the particle entrance frequencies, assuming that the particles are uniformly distributed and are carried along with the fluid. The volumetric flow rate Q (mL/s) can be converted into a particle flow rate (particles/s) using the known particle concentration (particles/mL). The average velocity v_{avg} can be obtained by dividing Equation 3.6 by the cross-sectional area of the channel to give

$$v_{avg} = \frac{d_c^2 \Delta P}{128 \eta L} \tag{3.7}$$

We can calculate the expected particle translocation time by dividing the length of the channel by the velocity obtained from Equation 3.7. Equations 3.6 and 3.7 predict that the volumetric flow rate Q and velocity v_{avg} should depend only on pressure and channel geometry. Therefore, the expected detection frequencies and translocation times of both particle sizes should be the same for a given channel size and pressure. While this would be true for point particles that can access the entire cross-sectional area of the channel, our particles have finite sizes that are subject to geometric constraints. Since large particles cannot approach the wall as closely, successful entrances are limited to streamlines that are closer to the center of the channel where the flow is fastest. Thus their average velocity should be faster than that of the small particles which are able to sample the slower streamlines near the walls. This is the principle behind hydrodynamic chromatography, in which analytes are separated by size as they are driven through a channel by a pressure gradient.[102] The predicted particles/s can be corrected based on these limitations by integrating the velocity only over the channel diameter range that is accessible to each particle size (the yellow shaded area in Figure 3-3a) rather than over the entire channel diameter, as is done to calculate the average velocity in Equation 3.7.

We examined the dependence of our three characterization parameters on both pressure

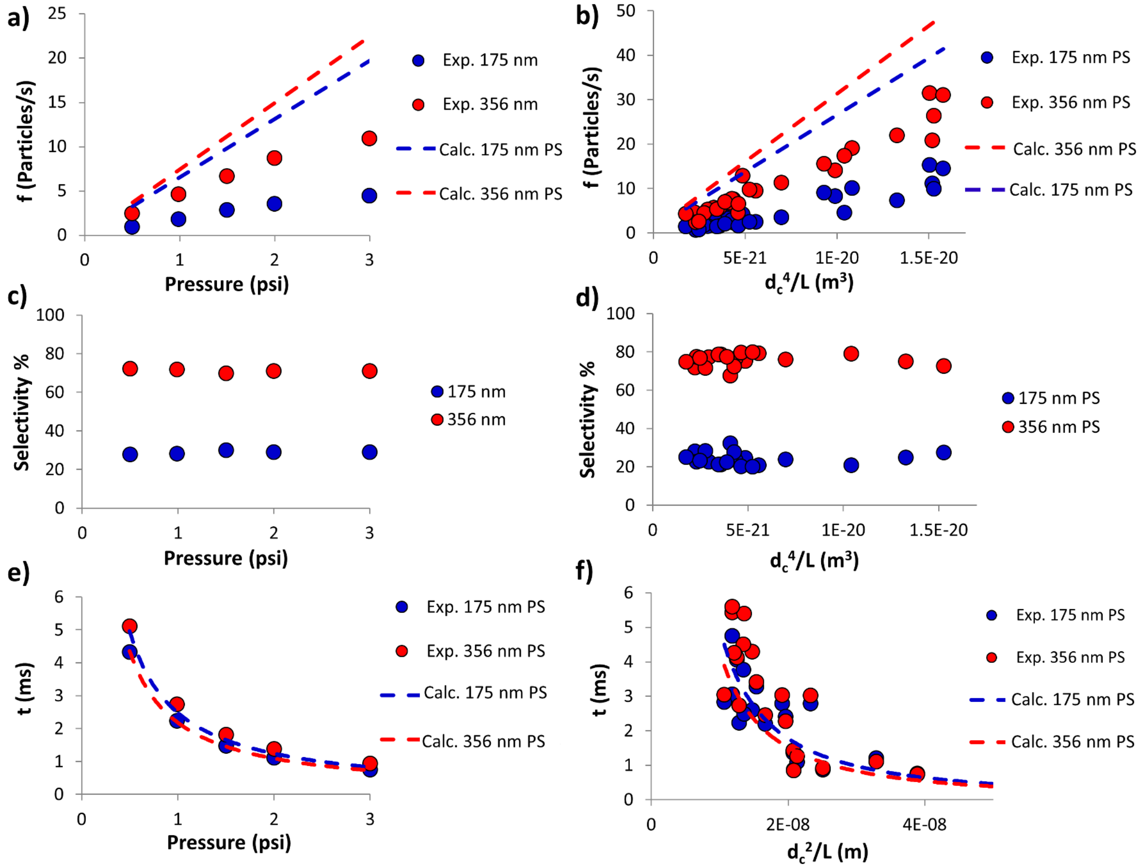

FIGURE 3-5: Comparison of characterization parameters for polystyrene particle detection as a function of applied pressure (a, c, e) and channel geometry (b, d, f). Experiments were performed with 175 nm and 356 nm polystyrene particles in 0.1 M KCl and 0.1% Triton X-100 using a 416-nm-diameter channel (L = 13 μm).

and channel geometry (shown in Figure 3-5) in order to determine any deviations from Poiseuille behavior that might provide insight into the possible mechanism of selectivity. All of the channel geometry data was collected at the same pressure (1 psi), and all of the pressure data was collected using the same channel to ensure that only one variable was changed at a time. We will discuss each of these parameters individually. For all graphs in both the pressure and voltage dependence discussions to follow, the predicted polystyrene behavior is plotted with red (356 nm PS) and blue (175 nm PS) dashed lines, whereas for silica it is plotted with light blue (361 nm silica) and brown (172 nm silica) dashed lines.

The predicted and experimental polystyrene particle detection frequencies are shown as a function of pressure in Figure 3-5a and channel geometry (d_c^4/L) in Figure 3-5b. Two important conclusions can be drawn from these results. First, the detection frequencies for both particle sizes scale linearly with pressure and with the critical channel geometry for Poiseuille flow (d_c^4/L), confirming that pressure is the primary driving force. However, both particle sizes are detected less frequently than predicted, suggesting that their entrance is somehow hindered, perhaps as a result of interactions with the channel walls. Interestingly, the deviation from prediction is more pronounced for the small particles, implying that their entrance is more inhibited. Yet the fact that the small particle detection frequency still scales linearly with pressure and with d_c^4/L suggests that whatever mechanism is responsible for the increased inhibition also scales with pressure and channel geometry.

Although the small particles have a weaker dependence on both pressure and channel geometry than the large particles, the selectivity % remains remarkably constant over both variables (shown in Figures 3-5c and d), indicating that neither the channel geometry nor the magnitude of the applied pressure is responsible for size selectivity. It is particularly surprising that selectivity is not affected by channel geometry, since the particles should have more interactions with the channel walls when the channel diameter is smaller. While we are unable to explain the reason for this lack of correlation, it is possible that the selectivity is primarily affected by interactions with the cross-sectional glass surrounding the channel entrance, which is several orders of magnitude larger than the channel diameter, as shown in Figure 3-3b. If these interactions dominate, there would be very little dependence on the channel diameter itself.

The predicted translocation times (based on the average calculated Poiseuille velocities) are plotted along with the experimental values in Figures 3-5e and f, providing information about particle behavior inside the channel. The experimental translocation times match the predicted trends and magnitudes very well, showing a $1/P$ dependence on pressure and a linear dependence on d^2/L. This again confirms that pressure is a significant driving force for particle translocation. According to the geometry argument outlined above, the larger particles should on average spend more time near the middle of the channel and should therefore travel through the channel faster than the small particles. As discussed previously, the fact that the translocation times for both particles sizes are the same is somewhat surprising given this argument but confirms that selectivity must happen outside the channel.

3.2.5 Silica Pressure Dependence

The same comparisons can also be made for the silica particles (shown in Figures 3-6a-f). The detection frequencies of both particle sizes appear to be independent of pressure below a certain threshold value ($\sim$1 psi), above which pressure begins to have an effect (Figure 3-6a). The behavior under this threshold value is likely governed by voltage. Silica particles should respond more strongly to an applied electric field relative to polystyrene particles due to their increased charge. This will be discussed in more detail in the following section. Since the magnitudes of the voltage and pressure forces appear to be similar for silica, the dominant driving force likely changes depending on the experimental conditions, with the electrophoretic force dominating at low pressures and the pressure force dominating at high pressures. Above the threshold point, the small particles appear to have a greater response to pressure than the

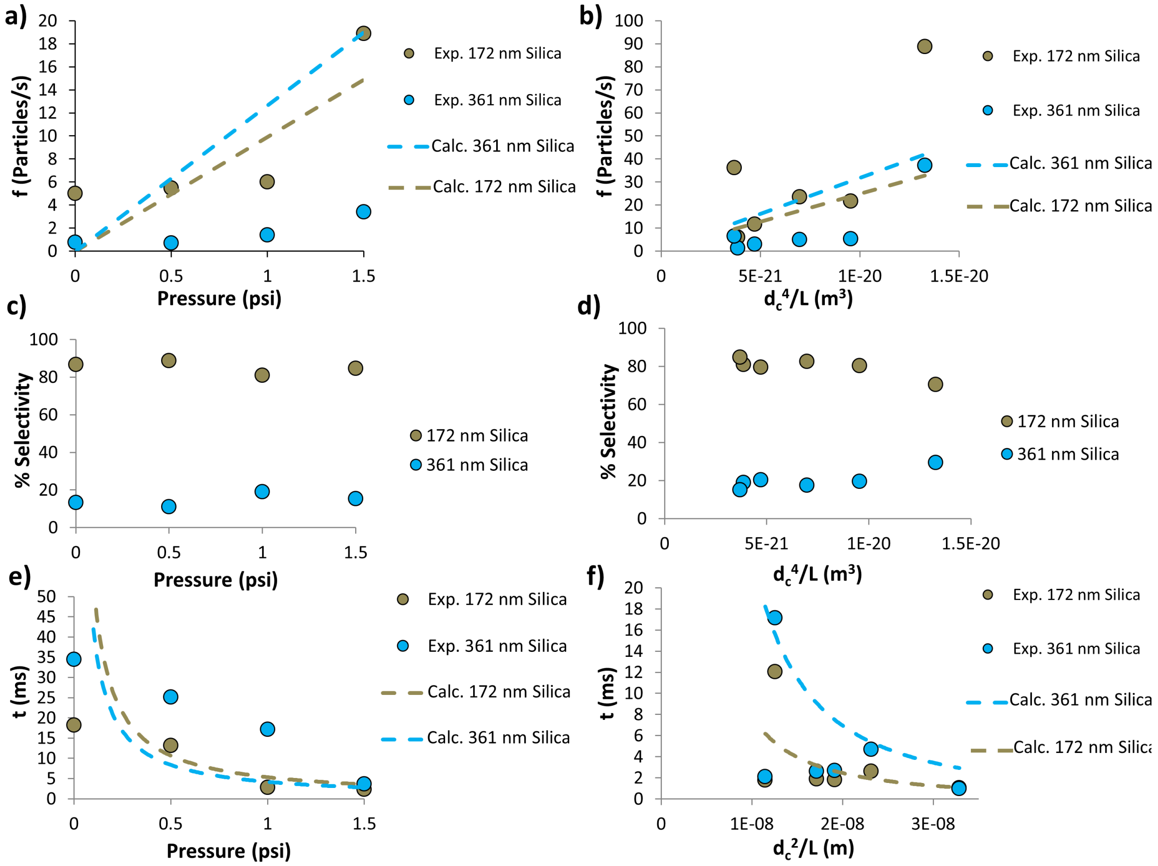

FIGURE 3-6: Comparison of characterization parameters for silica particle detection as a function of applied pressure (a, c, e) and channel geometry (b, d, f). Experiments were performed with 172 nm and 361 nm silica particles in 0.1 M KCl using a 555-nm-diameter channel (L = 25 μm)

large ones. It is difficult to draw many conclusions from the dependence of particle detection frequencies on channel geometry, as there is a wide spread in the data (Figure 3-6b). The deviation from the predicted values likely comes from two sources. First, there are a limited number of data points, which makes the error much higher. Second, the experimental detection frequencies were determined at 1 psi, which, as mentioned above appears to be the transition point between the voltage-dominated and pressure-dominated regimes. Therefore, there could be some additional variation introduced from this transitional behavior.

Similar to the polystyrene case, the selectivity for silica particles remains constant over the range of pressure values and channel geometries tested (Figures 3-6c and d), with the exception of the largest d_c^4/L value. The selectivity decreases at this value, which is expected since the particles are less confined when the channel diameter is larger.

While the translocation times show no clear dependence on channel geometry for either size (Figure 3-6f), the small silica times match the predicted values calculated as a function of pressure, following a $1/P$ dependence above 0 psi (Figure 3-6e). Interestingly, the large particle translocation times are quite a bit higher and instead decrease linearly with increasing pressure, matching the predicted value only at 1.5 psi, when pressure dominates over the voltage driving force as discussed above. The weaker pressure dependence for the large particles is again consistent with a stronger voltage influence, which agrees with the conclusions drawn from the detection frequency data above.

While pressure-driven flow is not as dominant of a driving force for silica particle translocation, these findings generally agree with those from the polystyrene data, confirming that neither channel geometry nor pressure is responsible for size selectivity.

3.2.6 Polystyrene Detection without Pressure

We also investigated how the three characterization parameters change in the absence of pressure (Table 3.2). Without an applied pressure, the driving force should be primarily voltage-driven (with a small contribution from diffusion). Since the total number of particles detected is much lower due to the decreased driving force, the error is much larger. However, there are still several important insights that can be gained from these data. First, as expected, the detection frequencies of both polystyrene particle sizes decrease without pressure due to a substantially lower driving force. Most importantly, the small particle translocation times are much longer (∼3X) than those of the large particles in the absence of pressure, matching the selectivity observed for the detection frequencies. This strongly suggests that whatever interactions are responsible for size selectivity outside the channel may in fact continue during particle entrance and translocation through the channel. However, pressure appears to act as a normalizing force, partially overcoming the selectivity mechanism to drive both particles through the channel at the same rate. This mediating effect is confirmed by the fact that the reverse size selectivity increases substantially without pressure (from 75% to 91% large particles). Nevertheless, the fact that selectivity still occurs even in the presence of pressure indicates that pressure is not strong enough to overcome the selectivity mechanism in the spatial regime outside the channel where the flow lines diverge. These results show that experiments would ideally be done without pressure in order to enhance size selectivity. However, this poses a significant challenge, as it is difficult without pressure to acquire enough particle events to be statistically relevant before the channel becomes blocked.

3.2.7 Silica Detection Without Pressure

The absence of pressure does not have as great of an effect on the silica particles (Table 3.2). While the detection frequencies for both particle sizes are slightly lower without pressure, they decrease by a much smaller amount compared to the polystyrene case. Likewise, the size selectivity increases (from 81% to 87% small particles) as do the translocation times, but the magnitudes of these increases are again much lower than for polystyrene. These results

Particles	***Pressure (psi)***	***d_c (nm)***	***L (μm)***	***% Small***	***% Large***	***f_{small}*** (Part./s)	***f_{large}*** (Part./s)	***t_{small}*** *(ms)*	***t_{large}*** *(ms)*
175/356 nm PS	0	635	12	9%	91%	0.1	1.2	114.7 ± 42	38.9 ± 8
175/356 nm PS	1	635	12	25%	75%	7.3	22.0	1.2 ± 0.4	1.1 ± 0.1
172/361 nm Silica	0	555	25	87%	13%	5.0	0.8	18.2 ± 2.0	34.4 ± 1.5
172/361 nm Silica	1	555	25	81%	19%	6.0	1.4	12.1 ± 1.3	17.2 ± 2.2

TABLE 3.2: Comparison of characterization parameters for polystyrene and silica particle detection with and without pressure.

confirm not only the normalizing effect of pressure on selectivity, but also the weaker pressure dependence of silica particle translocation, likely due to the larger role of voltage-driven flow.

3.2.8 Applied Voltage

Electrophoretic Effect

Compared to pressure, voltage-driven transport is expected to play a much smaller role in driving particle translocation, particularly for the polystyrene particles, which are only slightly negatively charged due to surface sulfate groups left over from the initiator during synthesis. Charged particles will move in an electric field by electrophoresis. The electrophoretic velocity v_{ep} is given by the following equation:[52]

$$v_{ep} = \frac{\varepsilon_0 \varepsilon \zeta_p E}{\eta} \tag{3.8}$$

where ε_0 is the permittivity of free space, ε is the dielectric constant, η is the viscosity of the solution, ζ_p is the zeta potential of the particle, and E is the magnitude of the electric field. Therefore, for a given channel and applied voltage, the only variable is the zeta potential. The zeta potential measurements for polystyrene and silica particles in 0.1 M KCl are shown below in Table 3.3. Since the particles are negatively charged, the electrophoretic force should drive the particles into the channel toward the positively charged working electrode inside the supporting capillary. The zeta potential values are much lower for the polystyrene particles when they are measured in a solution with added surfactant (0.1 M KCl with 0.1% Triton X-100). However, the large silica and polystyrene particles have remarkably similar zeta potentials in 0.1 M KCl (without Triton) even though silica would be expected to have a higher charge since the number of negatively charged sulfate groups on polystyrene is relatively low. Therefore,

Particles	*Zeta Potential (mV)*
172 nm Silica in 0.1 M KCl	-37.4
175 nm PS in 0.1 M KCl / 0.1 % Triton	-6.7
175 nm PS in 0.1 M KCl	-23.7
281 nm PMMA in 0.1 M KCl / 0.1% Triton	-6.0
356 nm PS in 0.1 M KCl / 0.1 % Triton	-11.5
356 nm PS in 0.1 M KCl	-51.0
361 nm Silica in 0.1 M KCl	-55.5

TABLE 3.3: Comparison of zeta potentials for different particle sizes and materials

as discussed in the material dependence section above, the slight increase in the detection frequency of large polystyrene particles relative to large silica particles measured using the same channel cannot be explained by the electrophoretic driving force, which should be the same for both materials. However, the majority of the selectivity difference between the two particle materials is due to the significantly higher detection frequency of the small silica particles relative to the small polystyrene particles. Since the small silica particles have a higher zeta potential, the electrophoretic force pushing them into the channel will be greater, which could account for some of this difference. Still, as we will show, particle charge differences alone cannot fully explain the material-dependent size selectivity.

Electroosmotic Effect

In addition to the electrophoretic force that results from the applied potential, there is also an electroosmotic force oriented in the opposite direction. Charged surfaces in contact with an electrolyte solution will attract a region of counterions from the solution to neutralize the charge, forming an electrical double layer. Since the silica nanochannel walls are negatively charged at neutral pH, this electrical double layer has a net positive charge and will move in response to the electric field, dragging the surrounding fluid and particles with it (regardless of their charge). Since the working electrode inside the channel is also positively charged, the electroosmotic flow is directed out of the channel. The equation for electroosmotic velocity v_{eo} is very similar to the equation for electrophoretic velocity except it depends on the zeta potential of the channel walls ζ_c rather than the particles:[52]

$$v_{eo} = \frac{\varepsilon_0 \varepsilon \zeta_c E}{\eta} \tag{3.9}$$

If the zeta potential of the channel walls is greater than that of the particles, electroosmotic flow should dominate, and the net effect of voltage should be to push particles away from the channel, which could affect size selectivity. Electroosmotic flow should be relatively uniform across the channel cross-section (except right near the walls where the double layer is located) and should therefore have a similar effect on all particles. However, when combined with the parabolic flow profile of pressure-driven flow, there can be significant differences in the direction of the net driving force along the channel cross-section, with electroosmotic flow pushing fluid out of the channel near the walls and pressure driving fluid into the channel closer to the center.[238,239] Therefore, particles could be driven either into or out of the channel depending on their cross-sectional position relative to the channel walls. However, at low pH when the channel walls should carry very little charge, electroosmotic flow should be very weak. Therefore, if it is affecting particle entrance, the selectivity should decrease dramatically at low pH, but as we will show it instead increases, suggesting that electroosmotic flow is not responsible for the reverse size selection observed for polystyrene. Nevertheless, it should still be considered, as it could result in an overall decrease in detection frequencies with increasing voltage and could be contributing to transport behavior in other ways.

3.2.9 Polystyrene Voltage Dependence

The role of voltage was explored by performing particle detection experiments at six different applied potentials (ranging from -1 V to +1 V) at 1 psi using the same channel. Since the applied voltage determines the baseline current level and ultimately the magnitude of the translocation pulse, we were unable to investigate voltages below +/-300 mV due to the low signal-to-noise ratio. Graphs of the three characterization parameters for polystyrene particle detection are shown in Figures 3-7a-c. It is important to note that 0.1% Triton X-100 was added to the particle solutions for these experiments, meaning that their zeta potentials (given in Table 3.3) are much lower than those discussed during the comparison with silica above. While ideally the experiments would have been done without adding Triton, it is difficult to collect enough data without surfactant before the channel is blocked.

A quantitative comparison with the expected detection frequencies based on Equation 3.8 is not beneficial, as the dominant pressure driving force makes the experimental values higher than predicted. However, the expected trend with voltage can be compared. Davenport et al. have reported that the magnitude of the electric field E can be approximated as follows:[33]

$$E = \frac{U}{L + \frac{\pi d_c}{4}} \tag{3.10}$$

where U is the applied voltage, L is the channel length, and d_c is the channel diameter. Therefore, the electrophoretic velocity given in Equation 3.8 should change by a factor of 3.3 from +/-300 mV to +/-1 V. If voltage has a significant influence on particle entrance, the particle detection frequencies should increase by a similar factor over the same voltage range.

At negative applied voltages, the slightly negatively charged particles should be driven

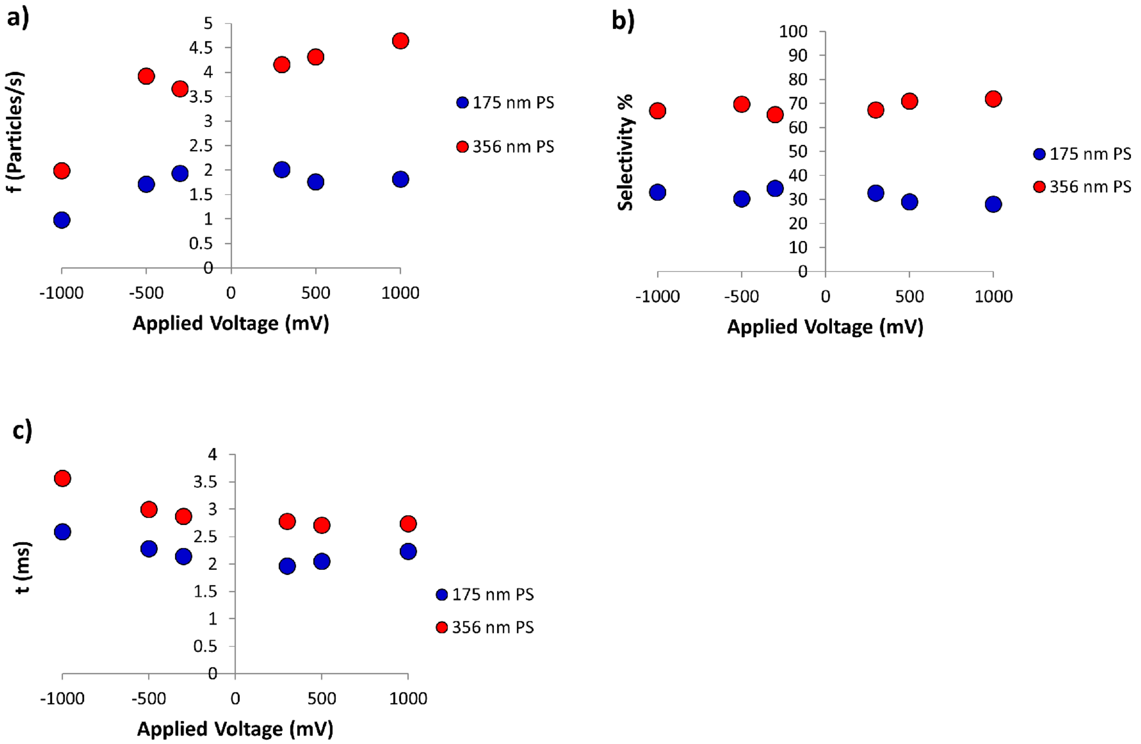

FIGURE 3-7: Comparison of characterization parameters for polystyrene particle detection as a function of applied voltage. Experiments were performed with 175 nm and 356 nm polystyrene particles in 0.1 M KCl and 0.1% Triton X-100 using a 416-nm-diameter channel (L = 13 μm).

out of the channel due to repulsion from the negatively charged working electrode inside the supporting capillary. However, the presence of pressure driving fluid into the channel ensures that they are still detected. The generally lower detection frequencies observed for both particle sizes at negative voltages match this prediction. However, these values only decrease by a factor of ~2 over the voltage range tested, meaning that particle entrance has a weaker dependence on voltage than expected. Likewise, the translocation times for both particle sizes increase with increasing negative voltage, which is consistent with the above explanation since the electrophoretic force pushing them out of the channel should slow them down.

Conversely, when the applied voltage is positive, the working electrode should attract the particles, driving them into the channel. Thus, the detection frequency should increase with increasing positive voltage. Indeed, the large particle detection frequencies do increase linearly with increasing voltage, but only by a factor of 1.1 over the entire voltage range, which is significantly smaller than the factor of 3.3 predicted by Equation 3.8, again demonstrating their weak dependence on voltage. The small particle detection frequencies remain relatively constant. These results reflect the slightly stronger electrophoretic force on the large particles due to their higher charge. The charge on the small particles is low enough that voltage does not appear to have much of an effect on particle entrance. The magnitudes of the translocation times are much smaller than predicted, and although they should decrease with increasing voltage due to the increased electrophoretic driving force, they instead remain relatively constant for both particle sizes. This again can be explained by the dominant pressure force, which we have already shown pushes particles through at about the same rate once they are inside the channel. Interestingly, size selectivity remains relatively constant over all voltage values with the exception of +/-300 mV, where it is slightly lower. The most surprising observation is the asymmetry in the particle behavior trends at positive and negative voltages, as the electrophoretic force should have the same effect in both cases, just in opposite directions. The fact that both particle sizes are more strongly affected by negative applied potentials indicates that there may be other consequences to the voltage polarity beyond simple electrophoretic effects.

3.2.10 Polystyrene Voltage Dependence Without Pressure

To further isolate and understand the role of applied voltage, polystyrene detection experiments were conducted under purely voltage-driven flow without any applied pressure (with 0.1% Triton X-100 added). As mentioned above, ideally all experiments would be conducted without applied pressure to amplify the size selectivity (since pressure has a normalizing effect), but the significantly decreased frequency of particle events under these conditions makes gathering enough data difficult. As a result of the much lower number of total events, the error bars for this data are much higher. Figures 3-8a-c show results for particle detection with the same channel at five different applied potentials between 500 mV and 1 V without any applied pressure. The dashed blue and red lines represent the expected behavior of 175 nm and 356 nm particles based on Equation 3.8. Again, the low signal-to-noise ratio below 500 mV prevented lower voltages from being included.

Several interesting conclusions can be drawn from these data. Again, while it is difficult to quantitatively predict the detection frequencies from Equation 3.8, since it describes the motion of the particles rather than the fluid like the Poiseuille flow equation, the qualitative trends with increasing voltage can be predicted. The detection frequency of the large particles is slightly higher than expected, increasing by a factor of 2.1 over the voltage range tested, compared to the expected factor of 1.5 predicted from the increased electrophoretic flow into the channel. This suggests that there is some additional influence on particle translocation from other forces. The small particles, on the other hand, are essentially not detected at all when the voltage is below 1 V, and even at 1 V the detection frequency is very low. This behavior is in agreement with the conclusions from the voltage dependence data with pressure above and can again be explained by the very low zeta potential of the small particles. At low voltages, the electrophoretic force is most likely too weak to have a significant effect on particle entrance. However, once a threshold voltage is reached, this force becomes strong enough to cause an increase in detection frequency. Since the zeta potential of the channel

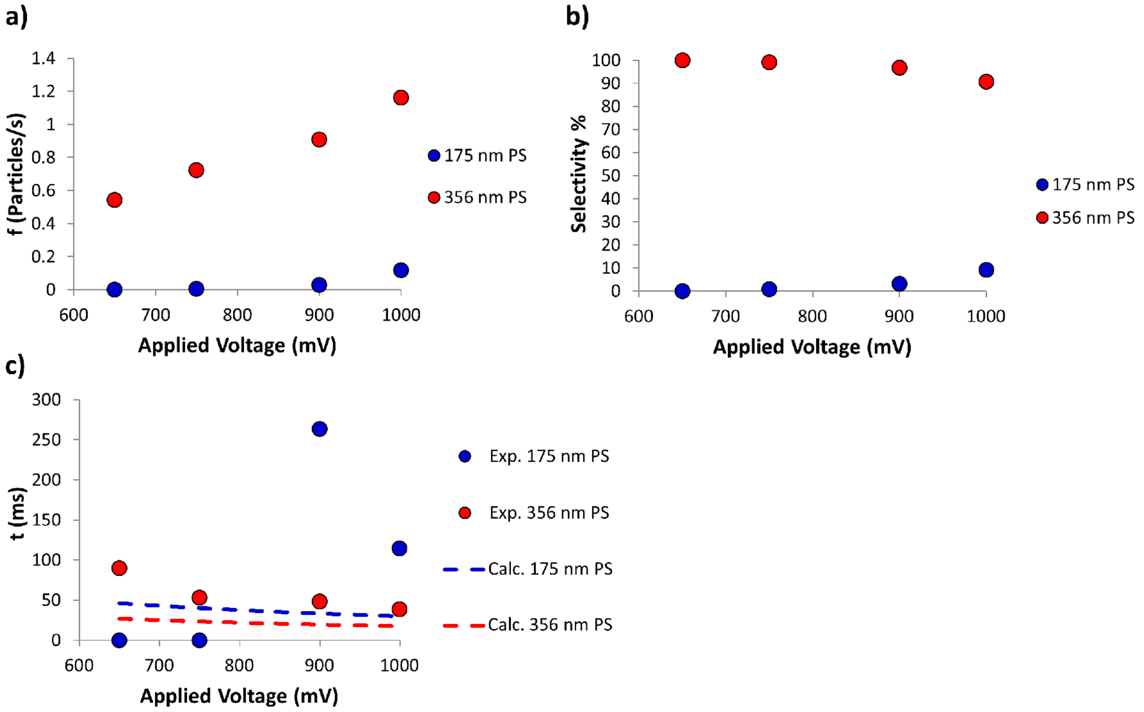

FIGURE 3-8: Comparison of characterization parameters for polystyrene particle detection as a function of applied voltage without pressure. Experiments were performed with 175 nm and 356 nm polystyrene particles in 0.1 M KCl and 0.1% Triton X-100 using a 635-nm-diameter channel (L = 12 μm).

walls is higher than the zeta potential of both polystyrene particle sizes (when surfactant is used), the electroosmotic flow should actually be stronger than the electrophoretic flow, with the net voltage effect pushing the particles out of the channel. Although this should be the case for both particle sizes, the electroosmotic flow should have a greater effect on the smaller particles than the larger ones due to their lower zeta potential (and thus their weaker ability to counteract it by electrophoresis driving them the other direction). This could be contributing to the very low detection frequencies observed for the small particles. Given this expected net voltage effect out of the channel, it is somewhat surprising that the particles are detected at all. Diffusion should continue to bring particles to the channel entrance, but this is expected to be a much weaker driving force, as discussed above. We are still evaluating the factors surrounding this voltage-driven behavior. Since Equation 3.8 predicts the linear electrophoretic velocity of the particles, it can be used to quantitatively predict translocation times, shown by the red (356 nm) and blue (175 nm) dashed lines. The translocation times match these same general trends, with the large particles moving through the channel faster at higher voltages but traveling quite a bit slower than predicted, and the small particles showing no clear trend since again the electrophoretic force appears to be too weak to have a noticeable impact.

Due to the very low small particle detection frequency without the added pressure driving force aiding their entrance into the channel, the reverse size selectivity is very high at all ap-

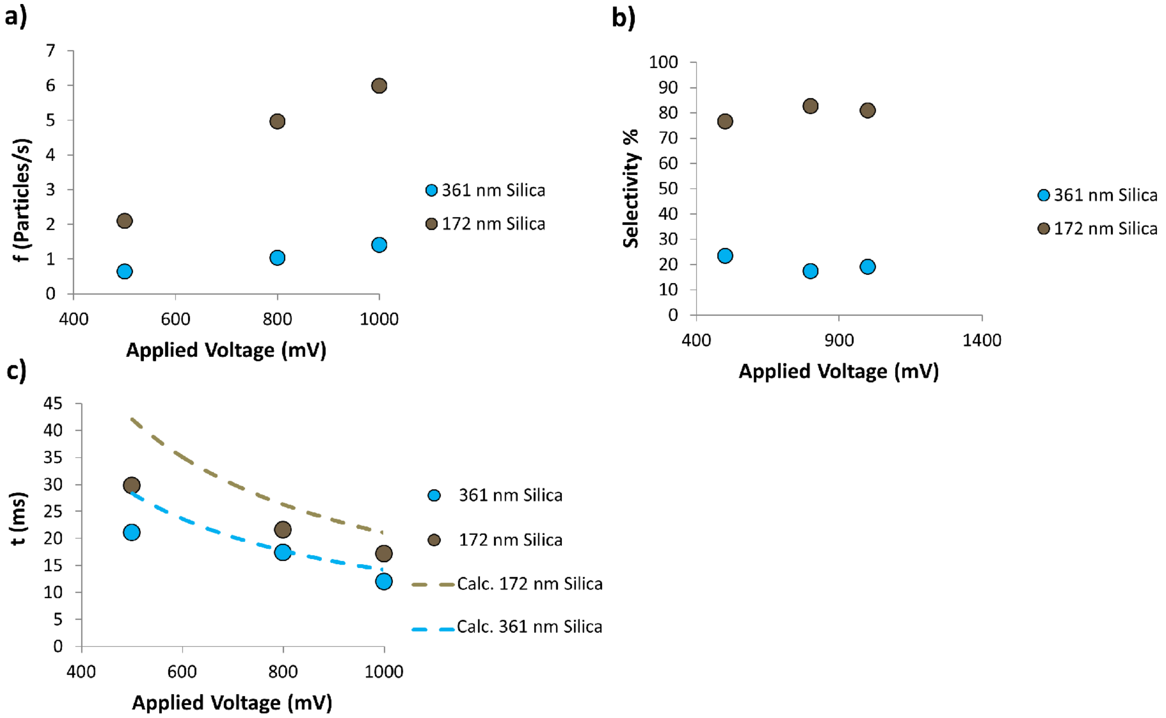

FIGURE 3-9: Comparison of characterization parameters for silica particle detection as a function of applied voltage. Experiments were performed with 172 nm and 361 nm silica particles in 0.1 M KCl using a 555-nm-diameter channel (L = 25 μm).

plied voltages, with large particles comprising 90-100% of all particles detected compared to only 75% for the same channel at 1 V with an applied pressure of 1 psi. Selectivity remains relatively constant until 1 V, when it decreases slightly because the electrophoretic force is finally strong enough to make a minor difference in small particle detection.

3.2.11 Silica Voltage Dependence

Voltage dependence experiments were also performed with silica at three voltages between 500 mV and 1 V at 1 psi using the same channel (shown in Figures 3-9a-c). The brown and blue dashed lines represent the predicted behavior for the 172 nm and 361 nm particles based on Equation 3.8. We were unable to collect data at negative applied voltages or without applied pressure due to the more frequent occurrence of channel blockages with silica.

Several interesting observations can be made from these figures. First, the detection frequencies for both sizes increase linearly with increasing voltage, as expected from the stronger electrophoretic force. However, the small particles show a significantly stronger voltage dependence than the large ones, which is somewhat surprising since the zeta potential of the large particles (and thus the expected electrophoretic driving force) is higher. The small particle detection frequency is quite a bit higher than predicted, increasing by a factor of 2.9 over the voltage range compared to the predicted factor of 2.0, whereas the large particle detection frequency matches the prediction closely, increasing by a factor of 2.2. These trends clearly indicate that additional influences outside of pressure and voltage are somehow enhancing small particle entrance.

These conclusions are further supported by comparing the voltage dependence of polystyrene and silica particles. Overall, voltage has a larger effect on the silica particles as expected from their higher charge. However, although the zeta potential of the large silica particles is $\sim$5X greater than that of the large polystyrene particles (with surfactant), their voltage dependence, analyzed by comparing the slope of the trendlines, is only twice as strong. This same comparison cannot be made for the smaller particles since a trendline could not be fitted to the small polystyrene data. The selectivity remains relatively constant over the tested voltage range, further supporting the conclusion that simple electrophoretic effects are not responsible for the reverse size selectivity observed for polystyrene particles. Further insight can be gained from examining the translocation times. Interestingly, although the small silica particles are detected more frequently, they actually move through the channel slightly more slowly than the large particles. Most notably, while the observed translocation times for polystyrene particles are substantially shorter than those predicted based on voltage alone due to the additional driving force from pressure, the translocation times for the silica particles are only slightly shorter than expected from voltage alone and roughly follow the expected voltage dependence. This further confirms that voltage is the more dominant driving force for silica, whereas pressure dominates for the polystyrene particles.

Although they do affect particle translocation, the obvious simple driving forces (diffusion, pressure, and voltage) do not appear to be responsible for size selectivity. The implications from this finding are significant. If large, simple driving forces are not responsible, selectivity must be due to nanoscale properties or interactions that are able to produce more macroscale effects. Therefore, we next turn our investigation to more subtle factors that might affect localized nanoscale properties and behavior. Voltage clearly affects silica more than polystyrene, but this difference cannot be explained solely by the increased electrophoretic driving force for silica, as explained above. Therefore, we looked at factors that might influence more local charge distributions. Our discussion of nanoscale effects will focus on polystyrene since the anomalous reverse size selectivity is only displayed when polystyrene particles are used.

3.2.12 Competition Effects

In order to determine whether particle-particle interactions or competition between particles contribute to size selectivity, experiments were repeated with only a single particle size present in solution. Table 3.4 shows the detection frequencies for each polystyrene particle size (175 nm and 356 nm) detected individually in solution compared to values for the two particle sizes detected in a mixture of equal concentrations with the same channel. Although the detection frequencies of both sizes are slightly higher when they are detected individually, they are

	f_{small} **(Part./s)**	f_{large} **(Part./s)**
Individually	1.1	3.7
Mixed Solution	0.9	3.1

TABLE 3.4: Comparison of polystyrene particle detection frequencies individually and in a mixed particle size solution. In all cases the individual particle concentration was held constant at 8.9 x 10^9 particles/mL.

Particles	***Solution***	d_c *(nm)*	***L*** *(μm)*	***% Small***	***% Large***	f_{small} (Part./s)	f_{large} (Part./s)	t_{small} *(ms)*	t_{large} *(ms)*
175 nm PS/ 356 nm PS	0.1 M KCl w/0.1% Triton	627	10	27%	73%	10.0	26.4	0.76 ±0.20	0.74 ±0.09
175 nm PS/ 281 nm PMMA	0.1 M KCl w/0.1% Triton	627	10	36%	64%	9.9	17.4	0.78 ±0.4	0.76 ±0.1

TABLE 3.5: Mixed material particle detection using equal concentrations of PMMA and PS particles.

nearly the same, suggesting that competition between the two particle sizes does not influence size selectivity.

Experiments were also conducted with small and large particles of different materials in the same solution. Particle detection performed with a 175 nm PS/281 nm poly (methyl methacrylate) (PMMA) particle combination was compared to detection conducted using the 175 nm PS/356 nm PS combination, with the characterization parameters shown in Table 3.2.15. Although the PMMA particles are smaller than the large PS particles, overall trends can still be compared. The PMMA particles should be more hydrophilic than the polystyrene particles, which could affect their interactions with the surrounding solvent. While the PMMA particles are expected to have a slight negative charge, the zeta potential was actually measured to be only -6.0 mV compared to -11.5 mV for the larger 356 nm PS particles. Therefore, the electrophoretic driving force for the PMMA particles is smaller than for the large PS particles, which could result in a slightly lower detection frequency.

When the larger particle is switched from PS to PMMA using the same channel, the small particle detection frequency stays the same. It is not affected by the other particle in solution even when it is a different material, again indicating that particle competition is not responsible for size selectivity. On the other hand, the large particle detection frequency decreases by a factor of 1.5. This decrease results in a significant shift in the size selectivity, with only 64% of the total particle detection attributable to the larger 281 nm PMMA particles compared to 73% when the 356 nm PS particles are used. Even though the PMMA particles are smaller than the

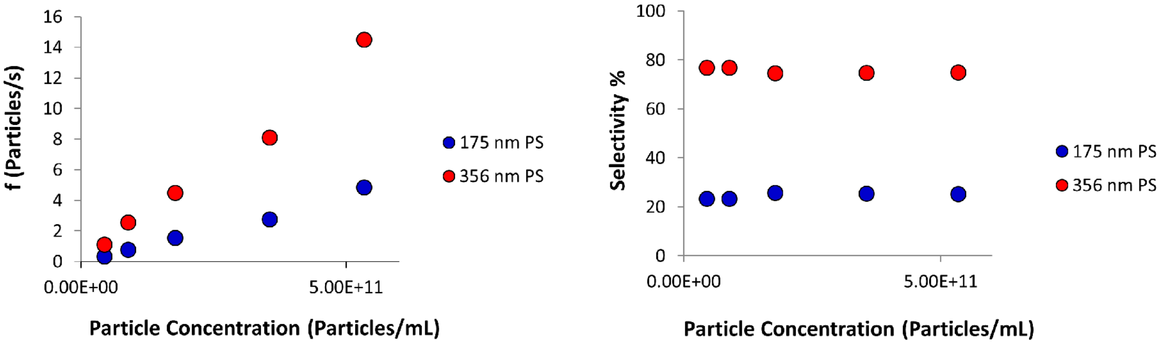

FIGURE 3-10: Comparison of characterization parameters for polystyrene particle detection as a function of particle concentration. Experiments were performed with 175 nm and 356 nm polystyrene particles in 0.1 M KCl and 0.1% Triton X-100 using a 457-nm-diameter (L = 18 μm) channel.

356 nm PS particles and should therefore be less geometrically constrained, detection of the PMMA particles is less favorable. This again confirms that particle material plays a key role in selectivity. Using PMMA decreases the selectivity, moving it more towards the silica particle trend that follows geometric predictions. This could be due to the more hydrophilic nature of the PMMA particles, which should result in a more tightly held solvation shell around the particle. It would therefore be harder to rearrange this solvation shell in response to local charge effects, which could affect its transport behavior. Results from mixed material particle detection with small 172 nm silica particles and large 356 nm polystyrene particles also confirm that the particle detection frequencies are unaffected by the presence of other particle materials and that competition is not responsible for selectivity.

Similarly, concentration dependence was also investigated for the mixed particle solution by performing experiments at four different polystyrene particle concentrations between 8.9 $\times 10^9$ and 5.3 $\times 10^{10}$ particles/mL using the same channel. In each case, the concentrations of the two particle sizes remained the same. The three characterization parameters are shown in Figures 3-10a-c. As expected, the detection frequencies increase linearly with concentration for both particle sizes by the same relative amounts. Additionally, the selectivity is essentially the same at all concentrations, further demonstrating that particle-particle interactions do not play a role in size selection.

3.2.13 Effect of Electrolyte Concentration

The electrolyte performs several key roles in our experimental setup. First, it carries the ionic current through the channel, which is necessary to detect particles as they pass through. Second, it determines the charge screening length for both the particles and the channel walls. The electrical double layer becomes more and more diffuse as it extends farther away from the charged surface until the charge is completely neutralized. The number of cations and anions present in solution will affect the thickness of this layer, with higher concentrations forming

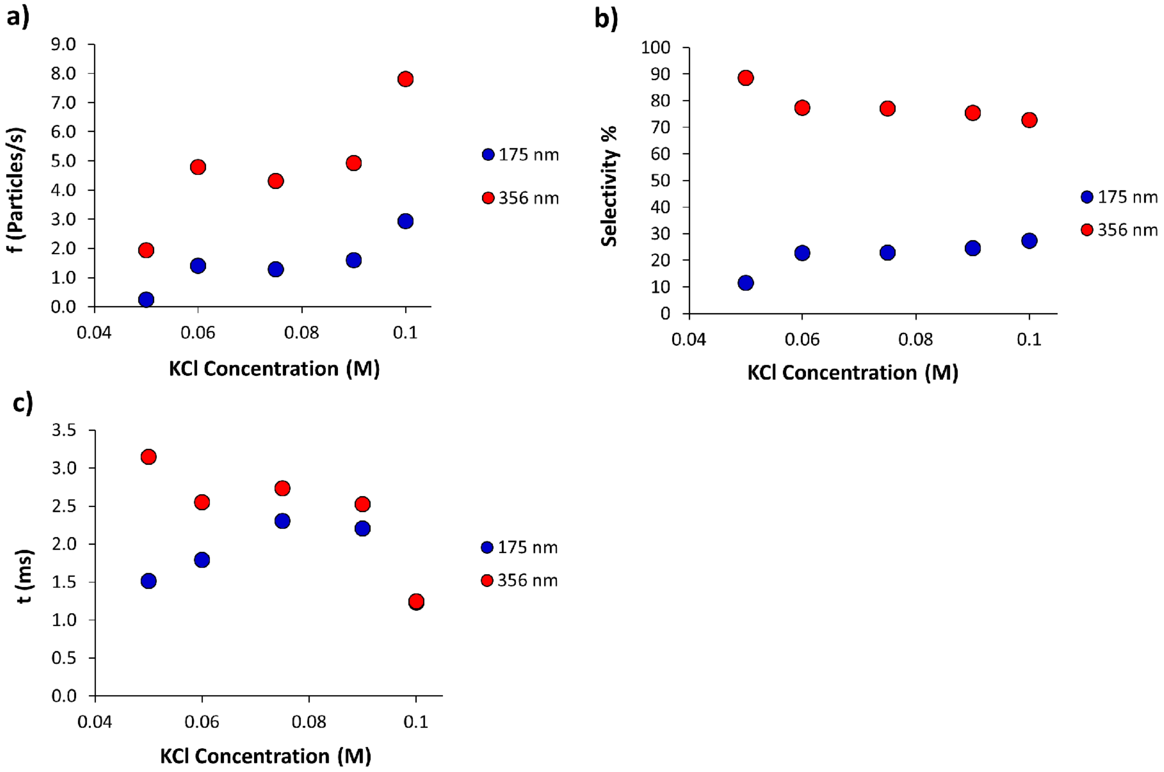

FIGURE 3-11: Comparison of characterization parameters for polystyrene particle detection as a function of electrolyte concentration. Experiments were performed with 175 nm and 356 nm polystyrene particles in KCl solutions of various concentrations and 0.1% Triton X-100 using a 715-nm-diameter channel (L = 10 μm).

a thinner double layer and lower concentrations forming a thicker, more diffuse layer. Since both the particle and channel walls are negatively charged, a double layer will surround both surfaces. Consequently, at lower electrolyte concentrations, the screening length of both the particle charge and the channel charge will be greater. Therefore, the effective charge very close to either surface will be higher. Additionally, this immediate solvation environment may be more polarizable at lower electrolyte concentrations, perhaps allowing it to respond more easily to localized charge differences and unique interfacial properties. This could have important implications for confined interactions, such as those that may occur between the particles and the channel walls. Therefore, we investigated the effect of electrolyte concentration by measuring the particle detection behavior at five different KCl concentrations (between 0.05 M and 0.1 M) using the same channel. Unfortunately, we were limited in the range of concentrations we could test. The particles aggregate if the KCl concentration is higher than 0.2 M, but the signal-to-noise ratio is too low if the KCl concentration is decreased by too much (since the percentage of current displaced by the particle is too small to detect). The three characterization parameters are plotted as a function of electrolyte concentration in Figures 3-11a-b.

The detection frequencies for both particle sizes decrease with decreasing electrolyte concentration, indicating that particle entrance is somehow inhibited as a result of thicker electrical double layers surrounding both the particles and the channel walls. The lower detection frequency could be partially a result of increased electrostatic repulsion when particles approach the walls. However, a higher effective charge should also result in a stronger electrophoretic force pushing the particles into the channel, which would increase the detection frequency. The resulting particle behavior due to the charge increase should therefore be a balance between these two forces. The fact that the frequency decreases suggests that either the electrostatic repulsion is stronger than the corresponding increase in the electrophoretic force, or there are other charge effects influencing particle behavior.

Interestingly, although the overall detection frequency decreases, the size selectivity remains relatively constant from 0.1 M down to 0.06 M. However, it increases significantly at the lowest concentration (0.05 M), with the large particle selectivity % rising to 89% from 73% at 0.1 M. A larger increase was probably not observed due to the relatively small electrolyte concentration range. We can compare the relative changes in the detection frequencies of the two particle sizes to determine which size is responsible for the observed selectivity changes. The low electrolyte concentration appears to have a larger effect on the small particles, decreasing their frequency by $\sim$12X compared to a decrease of only $\sim$4X for the large particles.

Surprisingly, the disparity between the large and small translocation times, while nonexistent in 0.1 M KCl, becomes larger and larger with lower electrolyte concentration. The large particles actually appear to slow down at low electrolyte concentrations even though they are detected more frequently. Since pressure typically pushes both particle sizes through at the same rate once they enter the channel, overcoming whatever forces are responsible for selectivity, deviation from this behavior may indicate that selectivity-related interactions at low electrolyte concentrations are strong enough to partially overcome the pressure normalization.

3.2.14 Solvent Dependence

Changes in the solvation environment can have a significant effect on local interactions and charge distributions. In order to gain a better understanding of how solvent might affect selectivity, we added ethanol to the solution of particles to create a solvent mixture of 20% ethanol and 80% water, while keeping the KCl concentration the same (0.1 M). Ethanol is less polar than water and will therefore decrease the overall polarity of the solvent. Ideally these experiments would have been performed in a more non-polar organic solvent to accentuate the polarity difference, but the particles aggregated when they were added to 100% acetonitrile or ethanol. Therefore, a mixture of ethanol and water was used to introduce more non-polar properties while still maintaining enough polar characteristics to keep the particles solvated. This highlights the dual hydrophilic/hydrophobic nature of the polystyrene particles. While bare polystyrene is inherently hydrophobic, the hydrophilic surface sulfate groups left over from the initiator during synthesis produce hydrophilic pockets. In addition, the manufac-

Particles	***DLS Diameter in 0.1 M KCl in 20% ethanol/80% water (nm)***	***DLS diameter in 0.1 M KCl in water (nm)***
175 nm PS	178	210
356 nm PS	326	379

TABLE 3.6: Comparison of polystyrene particle diameters obtained by DLS with and without ethanol.

Particles	***Solution***	d_c *(nm)*	***L*** *(μm)*	d_c^4/L	***% Small***	***% Large***	f_{small} (Part./s)	f_{large} (Part./s)	t_{small} *(ms)*	t_{large} *(ms)*
175 nm PS/ 356 nm PS	0.1 M KCl	635	12	1.3 x 10^{-20}	25%	75%	1.3	5.7	1.1 ±0.3	1.0 ±0.1
175 nm PS/ 356 nm PS	0.1 M KCl in 80% H_2O / 20% ethanol	705	16	1.5 x 10^{-20}	6%	94%	0.9	14.4	1.0 ±0.2	1.0 ±0.1

TABLE 3.7: Comparison of characterization parameters for polystyrene particle detection with and without ethanol addition.

turer adds a small amount of surfactant in order to disperse the particles in aqueous solution, making them somewhat more hydrophilic than they would be normally. Consequently, the hydrophobicity is likely non-homogeneous across the surface, which will affect the interfacial structure via unique interactions with the solvent and could lead to unusual behavior.

Dynamic light scattering size measurements were performed in order to verify that the particles do not aggregate in the 20% ethanol / 80% water solution. Interestingly, while no aggregation was observed, the measured hydrodynamic diameters for each particle size (shown in Table 3.6) are significantly lower than those measured in 0.1 M KCl and are also lower than the nominal dry particle diameters observed by SEM/TEM for the 356 nm particles. These decreases in the hydrodynamic diameter measurements provide strong evidence that the interfacial solvation environment between the particle and the solvent is strongly dependent on solvent polarity. In addition, the charge screening with ethanol should be weaker than with water, which should decrease the effective surface charge and may increase the polarizability of the solvation shell. However, this is difficult to verify using zeta potential measurements because the results are not reliable in non-aqueous solutions. The dependence of our three characterization parameters on ethanol addition is shown in Table 3.7.

Although we were unable to collect data with and without ethanol using the same channel, we can compare the results to those obtained using a channel with a similar d_c^4/L ratio, since we have shown that particle detection frequency is dependent on this geometric factor. While the small particle detection frequency remains relatively constant upon addition of ethanol, the large particle detection frequency actually increases by ~3X in the presence of ethanol.

Particles	***Solution***	d_c *(nm)*	***L*** *(μm)*	***% Small***	***% Large***	f_{small} (Part./s)	f_{large} (Part./s)	t_{small} *(ms)*	t_{large} *(ms)*
175 nm PS/ 356 nm PS	0.1 M KCl w/0.1% Triton	604	19	24%	76%	3.6	11.3	2.8 ± 1.0	3.0 ± 0.3
175 nm PS/ 356 nm PS	0.1 M KCl	604	19	19%	81%	1.7	7.4	2.4 ± 0.8	2.6 ± 0.2

TABLE 3.8: Comparison of characterization parameters for polystyrene particle detection with and without surfactant addition.

This results in a substantial increase in reverse size selectivity, with the percentage of large particles detected increasing from 75% to 94%. Interestingly, unlike for low electrolyte concentrations, the translocation times of both particle sizes remain the same after ethanol addition, suggesting that the applied pressure is enough to normalize the translocation times.

3.2.15 Effect of Surfactant

Surfactant is often added to the solutions of polystyrene particles to help prevent aggregation. Triton X-100 is a nonionic surfactant and is known to adsorb to the surface of polystyrene. Adding surfactant will therefore have two main effects on the particles. First, because it adsorbs to the surface, it will block some of the surface charge. This is confirmed by comparing the zeta potential measurements with and without surfactant in Table 3.3. Values for both particle sizes decrease significantly upon addition of surfactant, reflecting their lower effective charges. Second, the surfactant changes the hydrophilic properties of the particle. The nonpolar chain will attach to the nonpolar polystyrene surface, allowing the polar head to interact with the aqueous environment and increasing the overall hydrophilicity. Consequently, the ratio and distribution of hydrophobic and hydrophilic pockets on the surface will likely change upon addition of surfactant. This could have important implications not only for the interfacial structure, but also for the polarizability of the solvation environment and the response of the particle to local charge variations. Therefore, comparing particle behavior with and without Triton using the same channel may provide interesting insight into the mechanism of selectivity. The dependence of the three characterization parameters on surfactant addition is shown in Table 3.8.

One interesting conclusion can immediately be drawn. When the surfactant is removed, the detection frequencies of both particle sizes actually decrease. However, the reverse size selectivity increases, with 80% of detection events attributed to large particles compared to 76% with surfactant. This is consistent with the behavior observed when screening is reduced by lowering the electrolyte concentration, suggesting that either the double layer thickness or the effective charge is key to determining the overall detection frequency. The observed changes in particle behavior could be due to several different factors. First, similar to the low electrolyte concentration case discussed above, the higher effective charge could result in competing consequences. Increased electrostatic repulsion between the particles and the negatively charged walls should decrease the detection frequency, but at the same time the increased contribution from the electrophoretic force should push particles into the channel at a higher rate. Interestingly, the translocation times are slightly faster for the particles without surfactant, which could be due to the latter effect. In addition, the selectivity difference could also be a result of changes in the solvation environment due to decreased screening, unique interactions with the solvent caused by the non-homogeneous hydrophilic properties of the particle, or the blockage of surface group interactions by the adsorbed surfactant. These changes might affect the structure and interactions of the solvation shell, which could allow it to respond differently to charge.

3.2.16 pH Dependence

The silanol groups on the silica nanochannel walls have two pKa values at ∼4.5 and ∼8.5.[240–242] Therefore the pH of the solution will determine whether these groups are protonated or deprotonated. Experiments were performed at five different pH values ranging from 2.2 to 12 in 10 mM phosphate buffer with 0.1 M KCl and 0.1% Triton X-100 using the same channel. The particles are expected to remain negatively charged throughout this pH range due to the low pK_a of sulfuric acid. However, its second pK_a is right around 2, meaning that they will be somewhat less negatively charged at the lowest pH value tested. The characteristic parameters are plotted in Figures 3-12a and b. It is important to note that the ionic strength of the buffer solution at each pH value is not the same, since the relative concentrations of HPO_4^{2-} and $H_2PO_4^-$ ions are different (even though the total phosphate buffer concentration is the same). As we have already seen above, the ionic strength affects the selectivity. Therefore, differences in ionic strength could be contributing to any observed pH trends. However, the buffer concentration is much smaller than the overall KCl concentration, meaning that these effects should be fairly small. Comparing the selectivity percentages of the polystyrene particles for the same channel in 0.1 M KCl and 0.1% Triton X-100 (∼ pH 6) with those in the buffer solution adjusted to pH 6.25 shows that they are the same for both particle sizes (65% large / 35% small), confirming that the effect of slightly different ionic strengths is minimal.

The detection frequencies for both particle sizes generally decrease with increasing pH. This trend is consistent with electrostatic repulsion effects. As the pH increases, the nanochannel walls become more negatively charged, which should lead to increased repulsion of the negatively charged particles. This repulsion is expected to be greater for the large particles due to their larger surface area, and this is in fact what we see, with the detection frequency

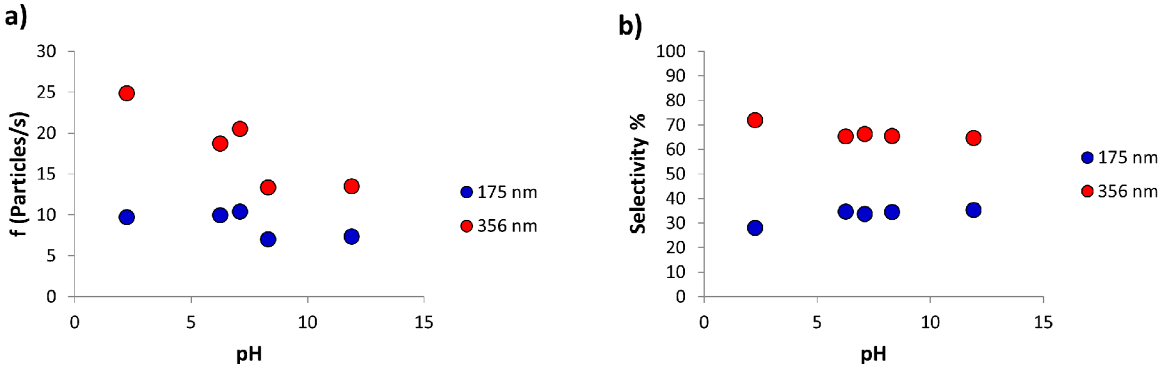

FIGURE 3-12: Comparison of characterization parameters for polystyrene particle detection as a function of pH. Experiments were performed with 175 nm and 356 nm polystyrene particles in 0.1 M KCl and 0.1% Triton X-100 using a 646-nm-diameter channel (L = 16 μm).

decreasing by ~1.8X from pH 2 to pH 12, compared to a decrease of ~1.3X for the small particles. However, even at pH 12, when the silanol groups should be mostly deprotonated and the repulsive forces should be the strongest, the large particles are still detected more frequently than the smaller ones. Additionally, at pH 2, when the majority of the silanol groups should be protonated and electrostatic interactions should be minimal, the larger particles are still detected more frequently than the smaller ones. In fact, while the size selectivity remains nearly the same for pH 6 through pH 12, it is slightly enhanced at pH 2. This strongly suggests that electrostatic repulsion effects between the particles and the channel walls are not causing size selectivity. However, this does not rule out the possibility that charge distribution or dynamical charge effects are contributing. As mentioned previously, the contribution from electroosmotic flow should be very small at pH 2 due to the low surface charge on the channel walls. Therefore, if electroosmotic flow was involved in the mechanism, the selectivity would decrease at pH 2 rather than increase.

While the exact mechanism responsible for the unusual reverse size selectivity is not clear, the results above suggest that charge effects are significant. However, they do not appear to be simple electrostatic effects and may instead be more dynamical charge effects resulting from polarization of the particles themselves or their surrounding solvation shells. The inhomogeneous hydrophobic/hydrophilic nature of the polystyrene surface likely produces a non-uniform solvation environment that is more loosely held and more easily polarizable, while the hydrophilic silica particles likely have a tightly held solvation shell that is harder to polarize. This could change their response to local charge effects in solution or near the nanochannel walls, altering their transport behavior. Different solution temperatures were investigated to gain additional mechanistic information and gather further evidence to support these suggestions.

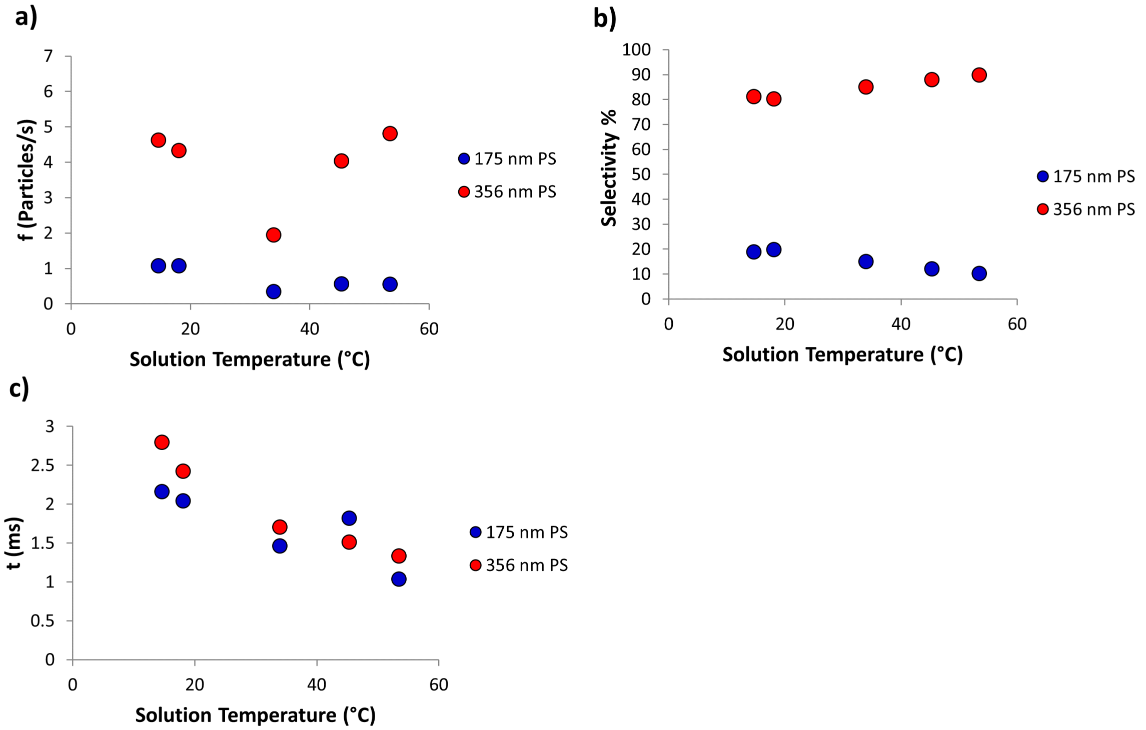

FIGURE 3-13: Comparison of characterization parameters for polystyrene particle detection as a function of temperature. Experiments were performed with 175 nm and 356 nm polystyrene particles in 0.1 M KCl using a 715-nm-diameter channel (L = 10 μm).

3.2.17 Polystyrene Temperature Dependence

Adding energy to the system in the form of heat can affect thermodynamically sensitive nanoscale processes. Therefore, we performed detection experiments at five different temperatures between 15 °C and 54 °C using the polystyrene particles in 0.1 M KCl (no surfactant) in order to gain further insight into the energy dependence of the relevant processes contributing to size selectivity. The characterization parameters are plotted in Figures 3-13a-c. It should be noted that the highest temperature data point represents fewer overall detection events and will consequently have a larger error. Interestingly, except for an anomalous point at 34 °C, the detection frequency varies minimally with no particular pattern for the large particles and decreases very slightly for the small particles with increasing temperature. This is somewhat surprising, since it is expected that the detection frequencies of both particles would increase with temperature, as the fluid should be moving faster. The translocation times, on the other hand, do decrease with increasing temperature, indicating that the particles are moving through the channel faster at higher temperatures once they enter—they just aren't entering any more frequently. While the 34 °C data could be significant, there may have been some systematic effect in this particular run that made the total detection frequencies lower for both particle sizes.

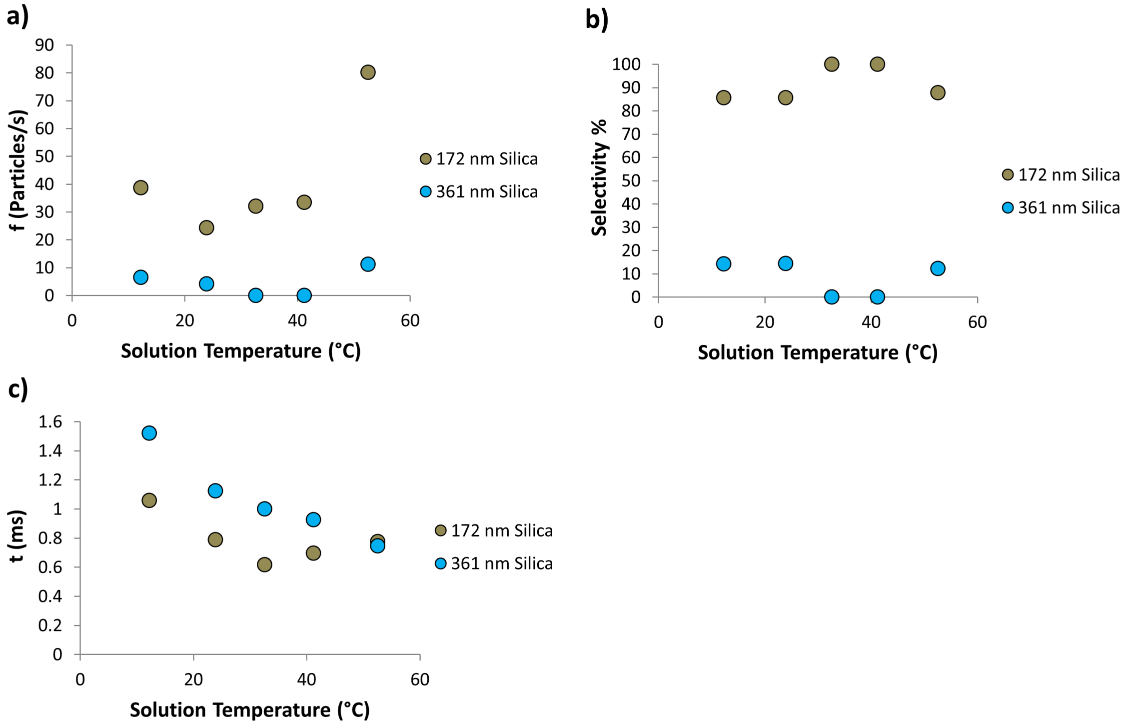

FIGURE 3-14: Comparison of characterization parameters for silica particle detection as a function of temperature. Experiments were performed with 172 nm and 361 nm silica particles in 0.1 M KCl using a 715-nm-diameter (L = 10 μm) channel.

However, the selectivity percentages (which essentially normalize all runs against anomalies) demonstrate that the reverse size selectivity is actually enhanced at higher temperatures, with the large particle selectivity % increasing to 90% at 54 °C. This suggests that the selectivity mechanism is energy dependent and may involve some sort of thermodynamic process, such as solvation shell reorganization or charge redistribution.

3.2.18 Silica Temperature Dependence

The same channel was used to investigate the temperature dependence of silica particles from 12 °C to 53 °C. The characterization parameters are plotted in Figures 3-14a-c. The detection frequencies of both particle sizes vary somewhat with temperature, but there is no clear trend. Similar to the polystyrene particles, the translocation times generally decrease with increasing temperature as expected from the faster fluid flow. Curiously, the small particles translocation times do begin to increase again at the highest two temperatures. However, the size selectivity is the same at all temperatures, except for 33 °C and 41 °C, in which 100% of detected particles were large. It is unclear why no small particles were detected at these two temperatures. Therefore, although there is some variation, the silica size selectivity does not show a clear trend with temperature like polystyrene does, suggesting that the selectivity mechanism for silica is not temperature dependent. This would be the case if it was solely based on geometry.

3.3 Conclusions

We have used resistive-pulse sensing to explore surprising material-dependent size selectivity in polystyrene and silica nanoparticle transport through silica nanochannels. When two different particle sizes are present in equal concentrations in solution, geometric constraints predict that smaller particles will be detected more frequently than larger ones. While this behavior is indeed observed with silica particles, when the particle material is switched to polystyrene a reverse size selection is exhibited, with larger particles passing through the channel much more frequently, suggesting that chemical identity plays a key role in determining transport. We determined that selectivity occurs outside of the channel and that simple driving forces (diffusion, pressure, electrophoresis) are not responsible. However, other more subtle charge effects do appear to play a role. For the polystyrene particles, reverse size selectivity increases at low electrolyte concentrations, low pH values, without surfactant, and when a more polar solvent is used. While it is not clear exactly what is responsible for the unusual size selectivity, these results suggest that charge effects are significant, possibly due to dynamical changes related to differences in the polarizability or hydrophilicity of the particles or the interfacial solvation environments. These could alter particle transport behavior by influencing their response to local charge fluctuations or structure variations in the surrounding environment, including near the nanochannel walls. Most importantly, these surprising results demonstrate that nanoscale effects and interactions can substantially influence mesoscale transport behavior when the size of the transported species approaches the size of the transport channel. This has important implications not only for gaining a better fundamental understanding of interfacial behavior under confinement, but also for leveraging these effects to design more efficient separation techniques and tunable transport systems.

3.4 Methods

Chemicals and Materials

All aqueous solutions were prepared using >18 MΩ•cm water from a Barnstead Nanopure water purification system. Triton X-100 (Sigma-Aldrich), potassium chloride (KCl, JT Baker), monopotassium phosphate (KH_2PO_4, JT Baker), dipotassium phosphate (K_2HPO_4, JT Baker), phosphoric acid (H_3PO_4, Mallinckrodt), and potassium hydroxide (KOH, JT Baker) were all reagent grade and were used without further purification. Polystyrene microspheres (d= 120 nm, 175 nm, and 356 nm) and poly(methylmethacrylate) (PMMA) microspheres (d = 281 nm) were purchased from Polysciences Inc. Silica microspheres (d = 172 nm and 361 nm) were purchased from Corpuscular, Inc. Quartz capillary tubing (o.d. = 1.0 mm, i.d.= 0.3 mm) was obtained from Sutter Instrument Company and silica microcapillaries (o.d. = 0.35 mm, i.d. = 20 μm) from Polymicro Inc.

Fabrication of Silica Nanochannels

Silica nanochannels were prepared in a multi-step process as reported previously.[208] Briefly, a small piece of a silica microcapillary (o.d.=0.35 mm, i.d.= 20 μm) is first sealed inside a larger silica capillary (o.d. = 1.0 mm, i.d.= 0.3 mm) using a laser-based micropipette puller (P-2000, Sutter Instrument Company). The diameter of the inner capillary is then decreased to $\sim$5 μm through a series of heating and cooling cycles under vacuum, after which the capillary ensemble is pulled into two ultrasharp nanotips. Larger borosilicate holders are produced using a filament-based micropipette puller (P-97, Sutter Instrument Company) by pulling borosilicate capillaries (o.d. = 2.0 mm, i.d.= 1.16 mm) into blunt tips with large openings. In the second step, a nanotip is inserted into this larger borosilicate holder under an optical microscope until the end of the nanotip protrudes from the holder opening by about 5-10 μm. It is then passed very quickly through a natural gas flame to seal a small section of the nanotip to the walls of the holder, after which the unsealed remainder of the tip is removed, leaving only the small sealed segment containing the silica nanochannel. The protruding end piece is then cut off under the optical microscope using a razor blade.

Measurement of Electrical Resistance

The current-voltage response of each silica nanochannel was measured using a Chem-Clamp potentiostat (Dagan, Inc.) and a PAR 175 universal function generator (Princeton Applied Research). The potentiostat was interfaced to a Dell computer through a PCI-6251 data acquisition board (National Instruments) via a BNC-2090 analog breakout box (National Instruments). The data was recorded using an in-house instrumentation program written with LabView 8.5 (National Instruments). All measurements were conducted inside a Faraday cage in a one-compartment, two-electrode cell with a Ag/AgCl working electrode inside the supporting nanochannel pipette and a Ag/AgCl reference electrode in the outside solution.

Microscopy

Optical images were acquired using a BX-51 microscope (Olympus) connected to a CCD camera.

Resistive-Pulse Sensing of Single Nanoparticles

Detection of polystyrene particles was performed in a custom-built Lucite pressure cell containing a small sample chamber with an opening for nanochannel positioning. A diagram of this cell is shown in Figure 3-1. Each nanochannel was secured in a vertical orientation with the tip immersed in the polystyrene particle solution. Particles were added only to the outside solution in the sample chamber. A Ag/AgCl electrode was placed inside the supporting nanochannel pipette, and another one was placed in the sample chamber to act as the reference electrode. All voltages were applied to the working electrode inside the nanochannel pipette. Constant pressure was delivered to the cell via a Femtojet Microinjector (Eppendorf). Current-time traces were acquired using an Axopatch 200B high-impedance amplifier (Molecular Devices, Inc.) and a Digidata 1440A digitizer (Molecular Devices, Inc.) interfaced to a Dell computer. A 1.0 kHz low-pass filter was applied to the amplifier during data acquisition, but no further filtering was performed.

Resistive-Pulse Analysis and Gaussian Peak Fitting

Resistive pulses from the amperometric traces were counted and characterized using Mini Analysis software (Synaptosoft, Inc.). OriginPro 8 data analysis software was used to generate a particle size histogram for each trace and to fit each peak in the histogram with a Gaussian function. Translocation times were measured using the Clampfit program from the Axon pClamp 10.4 software package (Molecular Devices, Inc.).

Dynamic Light Scattering and Zeta Potential Measurements

Dynamic light scattering (DLS) and zeta potential measurements were carried out using a Zetasizer Nano ZS instrument (Malvern Instruments).

CHAPTER 4

Gold Nanoelectrode Fabrication Methods

4.1 Introduction

ELECTROCHEMICAL TECHNIQUES are particularly well-suited for investigating nanoscale catalysis, as an increased temporal and spatial understanding of electron-transfer dynamics is key to the optimization of existing catalysts and the development of new ones. Traditionally, studies have focused on analyzing the behavior of an ensemble of nanocatalysts, but heterogeneity of individual nanoparticles limits the usefulness of this approach.[243] Thus, ideally these processes would be measured at a single-molecule level in real time in order to accurately correlate nanocatalyst structure with function. Gold can be easily modified to attach these nanostructures, making it an attractive material for these types of investigations.

This chapter focuses on using two unique gold nanowire fabrication techniques to produce individual, electrically insulated gold nanoelectrodes of controllable dimensions. The ultimate objective is to create a simple and reproducible method for the quick preparation of these electrodes for use in single-nanoparticle catalysis studies.

4.2 Gold Nanoelectrode Fabrication by Nanoskiving

The first fabrication method is based on a clever technique known as nanoskiving.[176,244,245] This process, developed by George Whitesides, takes advantage of the unique ability of a microtome to section samples with nanoscale precision. While this instrument is typically used to prepare sample slices for optical or electron microscopy, it is used here to achieve nanoscale wire dimensions. The basic procedure is as follows: epoxy is first poured over a nanopatterned PDMS mold to create a template. A thin film of gold is then deposited on top of this template, which is subsequently covered by another layer of epoxy, yielding a thin gold sheet

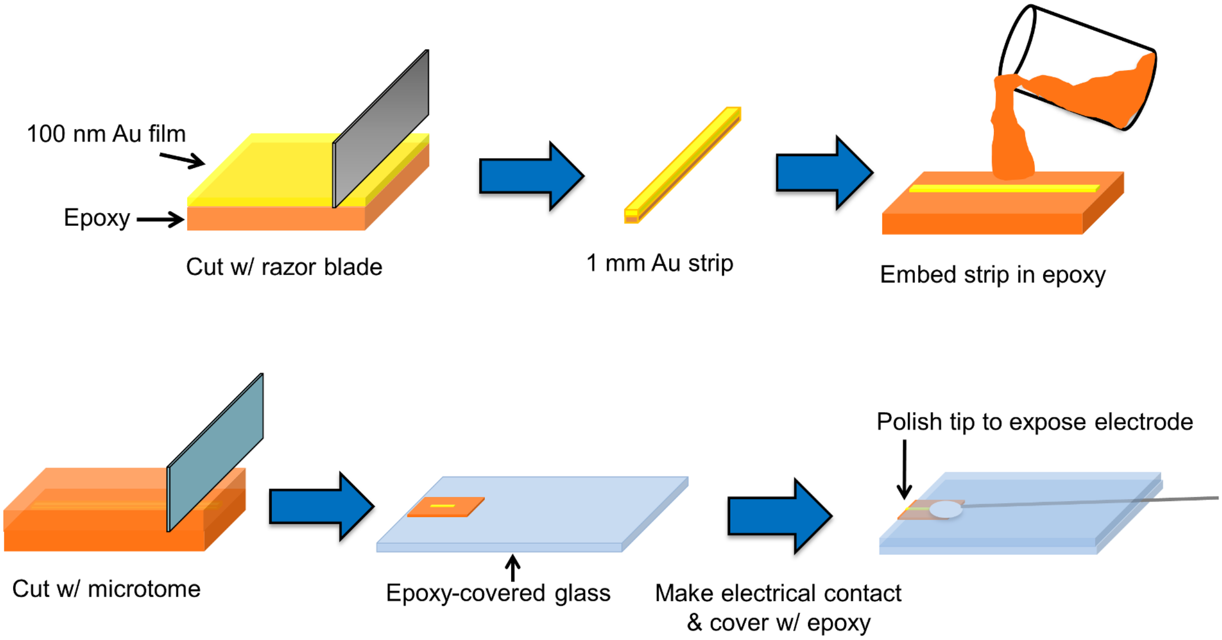

FIGURE 4-1: Diagram of gold nanoelectrode fabrication by nanoskiving.

sandwiched between two epoxy layers. A microtome is used to slice a thin section of this epoxy-gold assembly, which is transferred to a flat substrate and freed from the epoxy matrix using oxygen plasma, leaving behind an array of tailored nanostructures. This method has several advantages compared to traditional lithography methods. First, the dimensions of the nanostructures can be tuned by controlling the thickness of both the deposited Au layer and the microtomed section. Second, ordered, uniform arrays of many different shapes, including wires, rings, and squares, can be made by simply altering the original template. In addition, each slice can be easily manipulated and positioned and can even be stacked to create layered 3D structures,[246,247] and the same epoxy block can produce many slices, lowering the overall fabrication time. At the time of this work, this technique had never been used to fabricate an individual nanoelectrode. However, O'Riordan and coworkers published a similar paper shortly after,[248] although the surface area of their electrode is much larger than the wires described here due to differences in geometry.

Gold nanoelectrodes were fabricated using the nanoskiving technique according to the scheme shown in Figure 4-1. A thin film of gold (~100 nm) is first thermally evaporated onto a flat epoxy substrate and then cut into thin strips (~2 mm wide). One of these gold strips is embedded in the middle of an epoxy block, which is sectioned using a microtome to produce nanometer-sized wires. One major advantage of this method is that the diameter and height of the wire can be controlled by the thickness of the original evaporated Au film and the width of the microtomed piece, respectively. To fabricate a gold nanoelecrode, a microtomoed slice is transferred to a glass substrate that has been coated with epoxy. Electrical contact is made

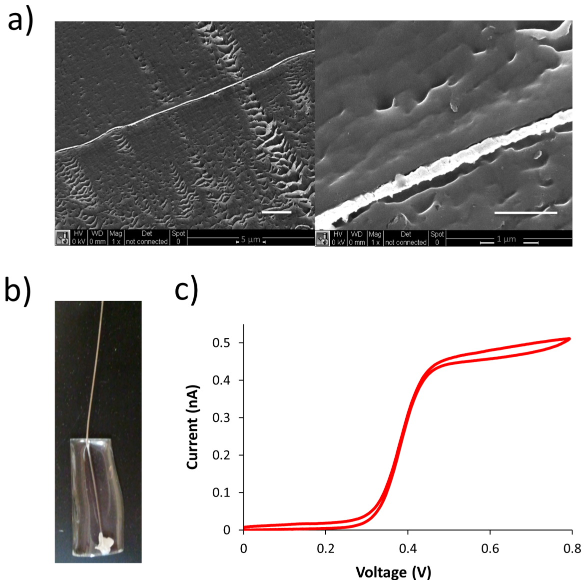

FIGURE 4-2: Characterization of a gold nanoelectrode prepared by nanoskiving. a) SEM images after microtome sectioning. b) Photograph of nanoelectrode after polishing. c) Cyclic voltammogram of the nanoelectrode shown in a) in 5 mM ferrocene in 0.1 M TBAPF$_6$ at a scan rate of 20 mV/s.

to the wire using conductive Ag paste before insulating the entire electrode with a top layer of epoxy. Electrodes are then polished using fine-grit sandpaper to expose the surface of the wire and characterized using cyclic voltammetry. Ideally the electrode can be re-polished to renew the surface while maintaining the same diameter, which is not possible with other fabrication methods that produce a tapered wire, such as the laser pulling or etching methods described previously.

Several challenges were encountered during this fabrication process, including bending of the gold strip inside the epoxy block during the heat curing step. When a bent strip is cut with the microtome, the resulting wire has a larger diameter than expected from the deposition thickness. Figure 4-2 shows SEM images of a wire cut from a 100-nm-thick gold strip with a diameter above 200 nm. Other problems include making good electrical contact to such a small wire and getting consistent cutting thicknesses using a glass knife, since it dulls quickly. In addition, the microtomed slices are very fragile, and the epoxy support can sometimes detach from portions of the wire, leaving the small wire vulnerable to breaking. In addition, since the length of the wire is so short, it is difficult to polish the electrode to expose the wire without overpolishing and hitting the conductive Ag paste. Many electrodes showed no electrical conductivity during polishing until the conductive Ag paste was exposed, indicating that either the wire itself was discontinuous or the electrical contact was not successful.

Of about one hundred nanoelectrodes fabricated in this manner, only a few were successful. One representative cyclic voltammogram is shown in Figure 4-2b. Although the surface area of this electrode is rectangular, an approximate diameter can be calculated using the equa-

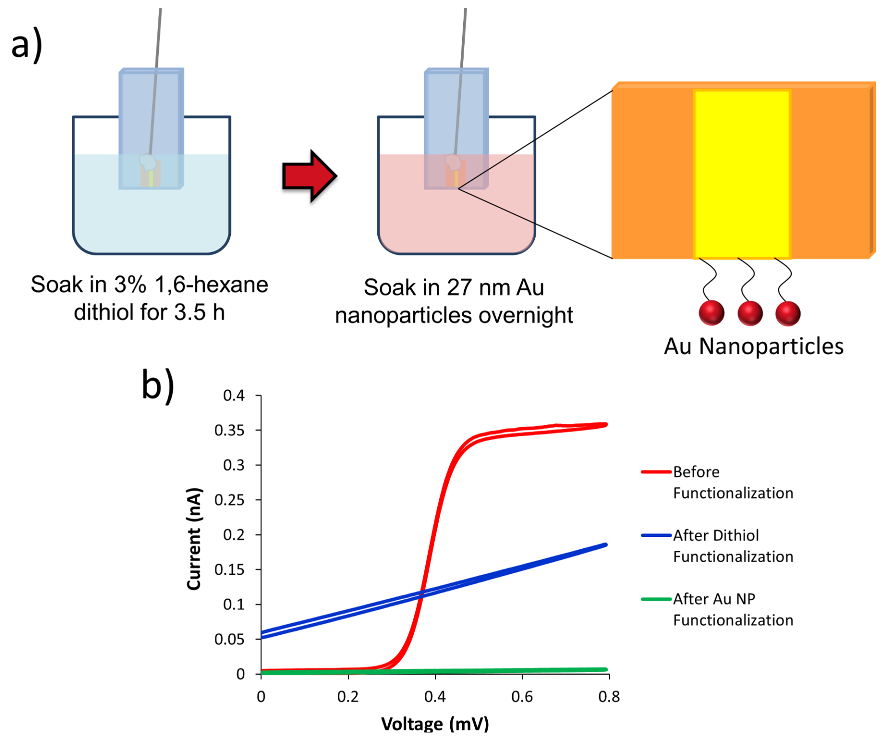

FIGURE 4-3: Gold nanoparticle functionalization of a nanoelectrode prepared by nanoskiving. a) Diagram showing the functionalization of the Au nanoelectrode in Figure 4-2 with 27 nm Au nanoparticles. 3% 1,6-hexane dithiol was used as a linker molecule between the electrode surface and the nanoparticles. b) Cyclic voltammograms of the nanoelectrode before and after each functionalization step in 5 mM ferrocene in 0.1M TBAPF$_6$ at 50 mV/s.

tion for the steady-state limiting current at a disk electrode, $i_{ss} = 4nFDC^{*}a$, where i_{ss} is the steady-state limiting current, n is the number of electrons transferred per redox molecule, D and C^{*} are the diffusion coefficient and bulk concentration of the redox molecule, and a is the radius of the electrode. The calculated diameter of 216 nm is within the expected range based on the SEM images shown in Figure 4-2a. Stability proved to be an issue with all of the successful electrodes. When the electrode shown in Figure 4-2 was re-tested after a few days, the current decreased substantially. This was observed with other electrodes as well, with the current sometimes decreasing within minutes of the initial scan. This could be partially a result of degradation of the insulating epoxy in the acetonitrile solvent used for cyclic voltammetry. Any degradation products or shrinking of the epoxy itself could result in either partial fouling of the electrode surface or recessment of the gold due to separation and detachment of the wire from the surrounding epoxy. Aqueous redox solutions would be a better choice for future experiments.

As a proof-of-concept experiment, the electrode in Figure 4-2 was functionalized with 27 nm Au nanoparticles using 1,6-hexane dithiol as a linker molecule (shown in Figure 4-3). Cyclic voltammograms were taken after both functionalization steps in order to assess the

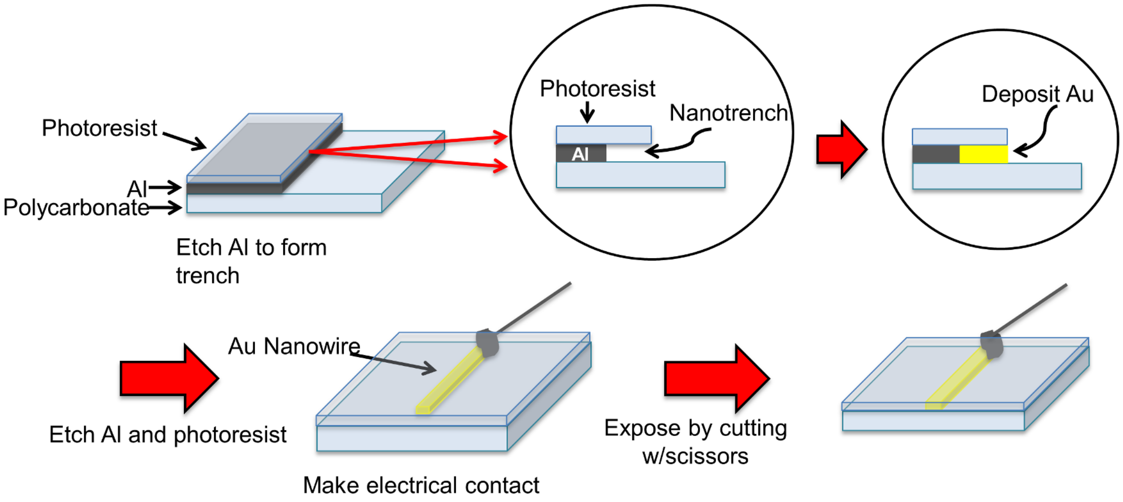

FIGURE 4-4: Diagram of gold nanoelectrode preparation by lithographically patterned nanowire electrodeposition (LPNE). A sacrificial aluminum layer is first covered with photoresist and patterned using a mask. The exposed photoresist is then removed, and the aluminum is etched along this new edge, creating a nanotrench. Gold is deposited into this trench from a solution of 6 mM $HAuCl_4$ in 0.1 M KCl using the aluminum layer as a working electrode. The aluminum layer and remaining photoresist are then removed, and electrical contact is made to the resulting nanowire using conductive Ag paste.

success of the procedure. As can be seen in Figure 4-3b, the current decreases after dithiol functionalization, as expected due to coverage of the electrode surface. However, after attachment of the conductive Au nanoparticles, the current decreases to almost zero rather than increasing again as it should. These results indicate that either the first or second step of the functionalization procedure was unsuccessful, or, given the previous pattern of electrode instability, that part of the gold may have detached and broken off.

Therefore, while this technique can produce gold nanoelectrodes with a good electrochemical response, the success rate is currently too low to make this a practical technique for mass production.

4.3 Gold Nanoelectrode Fabrication by Lithographically Patterned Nanowire Electrodeposition (LPNE)

The second approach is based on a nanowire fabrication technique developed by the Penner group called lithographically patterned nanowire electrodeposition (LPNE).[177,178,249–251] In this method, illustrated in Figure 4-4, a sacrificial metal layer is deposited onto a flat substrate, patterned with photoresist, and subsequently etched to produce a horizontal nanotrench beneath the overhang of the photoresist. Metals such as gold can then be electrodeposited into these trenches to create nanowires of different diameters by controlling the etching and deposition times. The photoresist and sacrificial metal are then removed, yielding the patterned

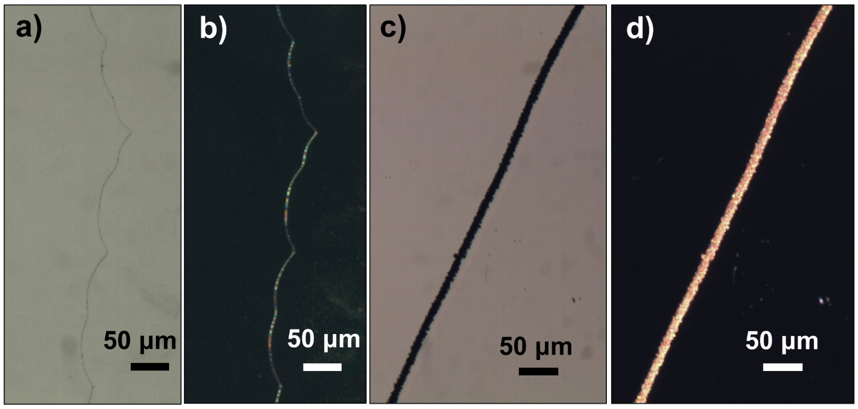

FIGURE 4-5: Optical microscope images of gold nanowires synthesized by LPNE. Bright-field (a) and pseudo dark-field (b) images of a nanowire formed using a rewriteable CD containing a thin aluminum film. Au was deposited from a solution of 6 mM $HAuCl_4$ in 0.1 M KCl at -1.25 V for 1 s, followed by -0.95 V for 30 s. Bright-field (c) and pseudo dark-field (d) images of a microwire formed as a result of a longer aluminum etching time.

nanostructure array. Like nanoskiving, this method has also been used to produce nanowire arrays of many different shapes.

Single nanoelectrodes were fabricated according to the scheme shown in Figure 4-4. Rewriteable CDs (CD-RW) contain a thin, uniform aluminum layer ($\sim$100 nm) on top of a polycarbonate substrate, which serves as a convenient starting material for LNPE, although other metal films and substrates can also be used. This film is first covered with photoresist and patterned using a mask to expose only half of it. The unexposed photoresist, along with the aluminum layer underneath, are then removed with a developer solution, producing a nanoetrench underneath the edge of the photoresist where the aluminum has been etched slightly further. An electrical connection is made to the aluminum layer, and gold is deposited into the nanotrench by submerging it in 6 mM $HAuCl_4$ in 0.1 M KCl at -1.25 V for 1 s, followed by -0.95 V for 30 s to 1 min, with the aluminum serving as the working electrode. The photoresist and aluminum are then removed with the developer solution, leaving the bare wire on the glass substrate. Electrical contact with the wire is established using conductive Ag paste, and the whole ensemble is insulated by spin coating another layer of photoresist on top of it. The electrodes are exposed by simply cutting the plastic substrate with a pair of scissors.

Figure 4-5a and b show a typical wire grown by this method. The scalloped shape of the wire is due to the mask we used, which had a curved edge. We found that it was difficult to precisely control the etching time. Therefore, many of the resulting wires either had larger diameters than expected (Figure 4-5 c and d) or varying diameters along their length due to inconsistent trench dimensions. Likewise, it is somewhat challenging to determine how long to deposit the gold. It has been noted in previous reports that once the gold reaches the end of the trench, it begins depositing dendrites out from the base wire,[177] which contributes to

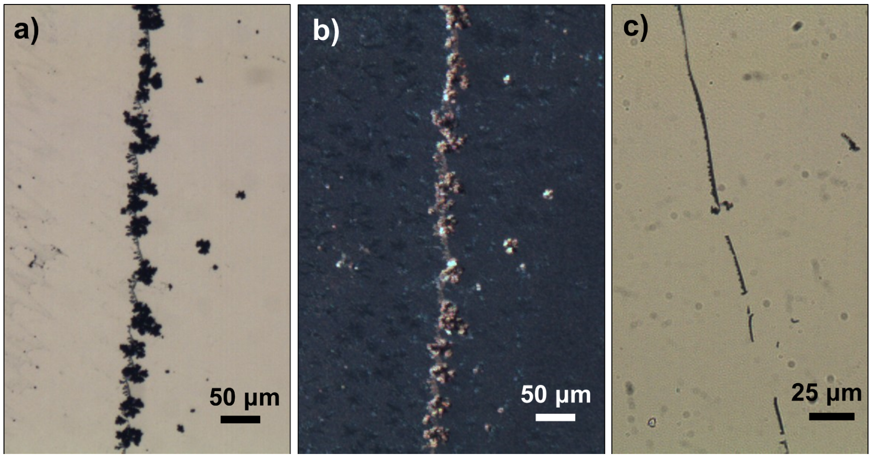

FIGURE 4-6: Optical microscope images of overgrown (a and b) and broken (c) gold wires synthesized by LPNE. Bright-field (a) and pseudo dark-field (b) images showing large gold dendrites grown from the main wire when the deposition front reached the edge of the trench. c) Bright-field image of a broken wire.

diameter variation, and this is indeed what we see with many of our wires (Figure 4-6a and b). Unfortunately, after making electrical connection, insulating with epoxy, and polishing, none of the nanoelectrodes demonstrated good electrochemical performance. Most cyclic voltammograms showed very tiny currents, suggesting that either there was a discontinuity in the wire itself, or electrical connection to the wire was not successfully established. On the other hand, some displayed a very high current, indicating that the photoresist insulation was incomplete or broken somewhere. Observations of optical microscope images, such as the one shown in Figure 4-6c, indicate that many of the wires were broken in places, either due to uneven gold growth or poor adhesion of the wire to the glass surface during subsequent removal of the photoresist and aluminum.

The major advantage associated with this method is that the electrode can be exposed by simply cutting through the wire and the surrounding insulating layers using a pair of scissors or a razor blade, eliminating the need for troublesome polishing, which often leads to inconsistent results. In addition, similar to the nanoskived electrodes, these electrodes can be cut repeatedly to renew the surface without changing the diameter. They can also be made much longer (cm) than the nanoskived wires (mm), making it theoretically easier to establish an electrical connection and repeatedly renew the surface without contacting the conductive Ag paste.

4.4 Conclusions

We have shown that two reported methods for making metal nanowires, nanoskiving and LPNE, can be used to fabricate single gold nanoelectrodes for use in electrochemical studies.

These techniques are advantageous because they allow control over the dimensions of the electrode and enable repeated renewal of the surface while maintaining the same diameter, unlike traditional pulling or etching methods that produce tapered wires. However, while some of the nanoskived nanoelectrodes showed a good electrochemical response, the success rate was low, and long-term stability proved to be an issue. The LPNE nanoelectrodes, while producing long wires, frequently displayed discontinuities over their length, making it challenging to successfully establish an electrical connection. More work is needed to optimize the fabrication conditions in order to increase the efficiency and reproducibility, but this work represents a proof of concept, demonstrating that these techniques can be successfully applied to single gold nanoelectrode fabrication.

Chapter 5

Preparation of Gold Nanowire Arrays

5.1 Introduction

As discussed in the introduction, nanometer-sized electrodes provide excellent temporal and spatial resolution due to high mass trasport rates and small double layer charging times.[16,18] Therefore, nanoelectrode arrays are particularly advantageous for electrochemical sensing applications. There are several advantages to using a bipolar electrode array design. First, the potential across each nanowire can be controlled wirelessly using a single potentiostat, eliminating the need for a direct connection to each electrode. In addition, high sensitivity and spatial resolution can be achieved by coupling electrochemical reactions on one side of the array to more sensitive reporter reactions (such as fluorogenic redox reactions) on the opposite end. In order to achieve the best spatial and temporal resolution possible, an ideal bipolar array should consist of densely-packed, highly uniform electrodes with small dimensions. Moreover, because the electrochemical reactions on both sides of each individual electrode are coupled, the wires must be straight and well-insulated from one another to avoid any potential cross-talk and to ensure the accuracy of the spatial information conveyed by the reporter reaction. Decreasing the thickness of the array helps limit this possibility. Although there are numerous different methods reported for nanowire array fabrication, preparing arrays with these ideal characteristics remains a challenge.

In this section, we describe efforts to fabricate uniform gold nanoelectrode arrays for bipolar electrochemical applications[134] based on reported methods. The work presented here involves the deposition of gold into the nanopores of polycarbonate (PC) and anodized aluminum oxide (AAO) membranes by two different mechanisms: electrodeposition and electroless deposition (direct chemical reduction). A summary of each mechanism is presented below, focusing on the challenges associated with producing uniform nanowire arrays. Although both methods resulted in some nanowire deposition, the electroless deposition technique has a number of advantages and proved to be far more successful, reliably yielding

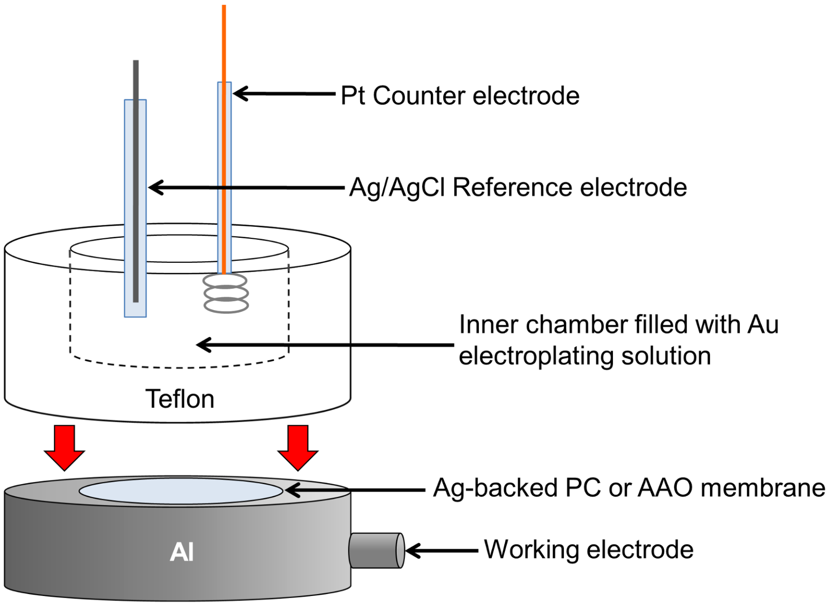

FIGURE 5-1: Diagram of the custom-built electrochemical cell used for Au electrodeposition in porous membrane templates.

uniform arrays of solid nanowires.

5.2 Electrodeposition

Electrodeposition of metals into nanoporous templates has been studied extensively, with many papers reporting vastly different experimental conditions and parameters. For electrodeposition to occur, direct electrical contact must be established with the template, usually by evaporating or sputtering a thin metallic film on one side. This film acts as the working electrode, reducing metal ions in solution at the appropriate applied potential. Establishing uniform electrical contact can be challenging for small nanoscale templates and introduces the potential for non-uniform electric fields, which can affect growth rates. However, this direct connection offers straightforward control over the working electrode potential, which is helpful for tuning deposition rates.

Polycarbonate Membranes

Polycarbonate (PC) filter membranes were initially chosen as the template for Au nanowire electrodeposition because they are commercially available with a variety of nanometer-sized pore diameters, eliminating the need for time-consuming template fabrication steps. Au nanowires were grown in polycarbonate (PC) membrane filters (SPI) with 30 nm pore diameters and a nominal thickness of 6 μm.

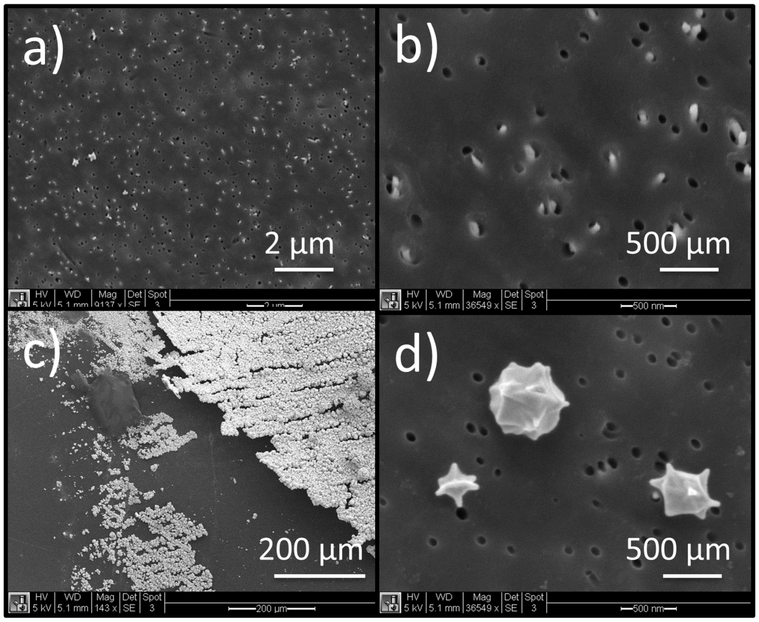

FIGURE 5-2: SEM images from different spots on the surface of a PC membrane after DC electrodeposition at -1.1 V for 4 h. Scotch tape was used to try and remove the surface layer and the membrane was etched 10X in 50:50 chloroform/EtOH to expose the wires. Images courtesy of Stephen Percival.

Silver was thermally evaporated onto the back of a membrane to form an electrically conductive layer. The membrane was then sonicated for 1 min in water and allowed to soak in diluted 50:50 H_2O/Orotemp Au electroplating solution containing $KAu(CN)_2$ (Technic) prior to electrodeposition to ensure thorough pore wetting, as many papers state that a sonication step is crucial to achieving homogeneous growth over the membrane.[252–254] The silver side of the membrane was then placed in contact with a conductive surface to form the working electrode while the other side of the membrane was positioned in contact with the gold electroplating solution in a custom-built cell (shown in Figure 5-1).

Over sixty nanowire growth experiments were conducted in PC membranes. Conditions such as applied potential, deposition time, surface treatments, and Ag working electrode thickness were varied in order to determine optimal conditions. Electrodeposition of Au has been reported at many different potentials, ranging from -0.49 V to -1.4 V vs. SCE.[252–255] Recently, Soleimany *et al*. determined that the mechanism of gold reduction in polycarbonate membranes is different depending on the applied potential.[255] Additionally, although all of the gold plating solutions in these references contain gold cyanide salts, the concentrations and compositions of the solutions differ slightly, as do the pore diameters and membrane thicknesses. It is unknown how these differences affect the required deposition potential. Multiple potentials were tested in the work presented here due to this assortment of reported values (from -0.5 V up to -1.1 V vs.Ag/AgCl). However, since little difference was observed, most experiments were carried out at the high end of the spectrum (-1.1 V) to try and reduce the

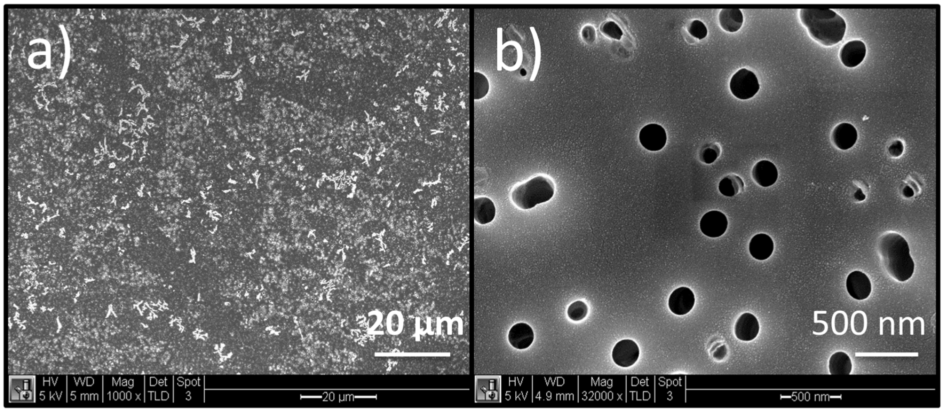

FIGURE 5-3: SEM images showing the partially filled pores of a PC membrane after DC electrodeposition of Au at -1.1 V for 40 min. A 20 nm Cr adhesion layer was deposited between the membrane and the 300 nm Ag film backing to try and improve electrical contact, and the membrane was degassed under vacuum for 45 min prior to electrodeposition to improve wetting.

overall deposition time. Reported Au deposition times are also highly variable, ranging from minutes[252,254,255] to hours.[46] Deposition was initially carried out for between 1 and 15 min, but the time was increased to 24 hours with several time points in between to see if this improved deposition homogeneity. While it perhaps resulted in a bit more wire growth, there was no significant improvement in uniformity with longer deposition times.

Consistency, both within the same membrane and between membranes, proved to be the single most troublesome problem with nanowire array deposition. Even membranes where wires were observed also contained other spots with empty pores, partially filled pores, and areas of dense surface coverage or large, oddly-shaped surface crystals (as seen in Figure 5-2). Reproducibility of wire growth between membranes was also highly variable. The exact same electrodeposition conditions used for the membrane shown in Figure 5-2 were repeated five times in subsequent trials with different results, none of which showed wires extending out of the membrane. The most likely causes of this low reproducibility are non-uniform electrical contact and insufficient pore wetting.

Each of these possible causes was explored further. A 50 nm silver layer was used as the conductive membrane backing for the majority of experiments, similar to other published procedures.[255,256] However, since several papers report using a thicker conductive layer,[252–254] the thickness was increased to 200 nm to see if poor contact with the working electrode was the cause of observed inconsistencies. No significant difference was detected in wire growth or quality. However, it is possible that the Ag backing is still not making adequate electrical contact between the pores and the working electrode. Valizadeh *et al.* mentioned that using a 20 nm Ti adhesion layer before the Ag coating was necessary for good adhesion.[254] Recently, we tried applying a 20 nm Cr adhesion layer to the back of the membrane, followed by a 300 nm Ag coating to serve as the working electrode. The sample was also degassed under vacuum for 45 min prior to electrodeposition to try and improve wetting. SEM images in Figure 5-3 reveal that the homogeneity across the surface seems to have improved. Many of the pores are partially filled, and there appears to be a much more uniform fill percentage compared to past trials. However, the origin of the surface structures is still not understood, and the deposition time needs to be increased to completely fill the pores.

With the inconsistencies observed in the electrodeposition of Au in PC membranes, efforts were re-focused on other methods, including deposition in anodized aluminum oxide membranes and electroless deposition techniques.

AAO Membranes

Given the challenges encountered growing uniform gold nanowires in PC membranes, we also explored anodized aluminum oxide (AAO) templates. Wires grown in AAO membranes are advantageous for bipolar applications because the pore density is much higher and much more uniform. There has been a lot of research focused on understanding and optimizing nanowire growth in AAO templates. It has long been known that anodic oxidation of aluminum produces ordered nanopore arrays, with studies dating back to the 1950s.[257] Since then, significant improvements have been made, resulting in more ordered pores and better control over characteristics such as diameter and length.[258,259] Although the process is not fully understood, pores are formed under steady-state conditions when equilibrium is reached between field-assisted dissolution at the electrolyte/oxide interface and oxide growth at the oxide/metal interface.[259] While commercial AAO membranes are available, we were unable to purchase them at the time of these experiments, opting instead to fabricate our own. Therefore, much of this work concerns the preparation of the AAO templates themselves and the related challenges associated with achieving uniform gold deposition.

We first tested different anodization potentials and times to determine the optimal parameters for fabricating reproducible porous membranes in two different types of aluminum. Flattened Al pellets of 99.99% purity (Kurt Lesker) used in initial experiments were anodized at 30 V in 0.3 M oxalic acid for ∼20.5 h in an ice bath. However, the majority of experiments were done using thinner (0.004 in) Al sheets of 99.99% purity (ESPI Metals), which eliminated defects caused by the stress of flattening the pellets and required shorter anodization times (∼7.5 h at 40 V in 0.3 M oxalic acid, also in an ice bath).

Depositing gold nanowires into the pores of these membranes presented new challenges stemming from the presence of an inherent insulating barrier layer between the pores and the bulk aluminum beneath. The structure of an ideal AAO membrane is illustrated in Figure 5-4. This barrier layer presents a significant obstacle to electrodeposition, as the bottoms of the pores need to be conductive in order for this method to be successful. Barrier layer thickness is related to the applied potential. Therefore, many papers report a sequential voltage decrease at the end of the anodization to thin the barrier layer, although specific conditions of this decrease

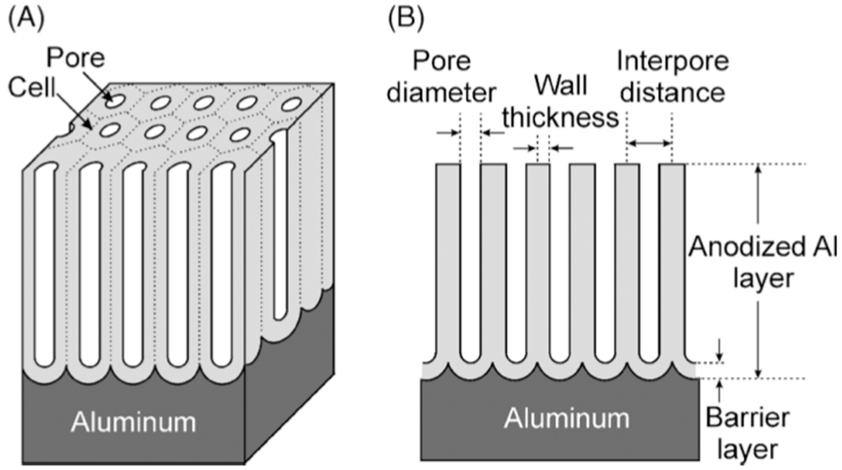

FIGURE 5-4: Structure of an ideal anodized aluminum oxide membrane (A) and cross-section of the pore structure (B). Taken from ref. 259.

vary.[259–261] We performed this voltage decrease at the end of each anodization using conditions found in a few different published methods.[260,261] Beyond this widely-reported initial barrier layer thinning, several other techniques have been developed to enable electrodeposition in the pores, and three of these methods are investigated herein: membrane separation followed by direct current (DC) electrodeposition, alternating current (AC) electrodeposition, and cathodic polarization followed by DC electrodeposition.

Membrane Separation Followed by DC Electrodeposition

An outline of the separation and DC electrodeposition process is given in Figure 5-5. Anodized membranes were successfully separated from the Al base by dissolving the aluminum layer in 50% saturated $CuSO_4$ / 38% HCl, a mixture found by Ding and co-workers to dissolve Al quickly without the hazardous Hg byproduct produced using the more traditional $HgCl_2$ method.[262] Although the separation was easy, handling the fragile membrane proved to be extremely challenging, as it was very brittle and easily broken, as reported by others.[262–265] Multiple membranes were broken after this removal step, but one membrane was successfully soaked in 5% phosphoric acid at 35 °C for 30 min to dissolve the remaining barrier layer. It was then coated with 60 nm of Ag to form a conductive substrate, after which electrodeposition was carried out at -1.1 V for ~3.5 h in the same commercial gold plating solution and Teflon cell used for the PC membranes. While the porous membrane looked good, no wires were observed in SEM images taken of the pores after deposition. It is possible that cracks developed in the fragile membrane from the pressure of the Teflon cell, allowing the solution to bypass the pores. Non-uniformity or delamination of the conductive Ag backing could also have contributed to the lack of wires. Indeed, Moon and Wei found that directly evaporating

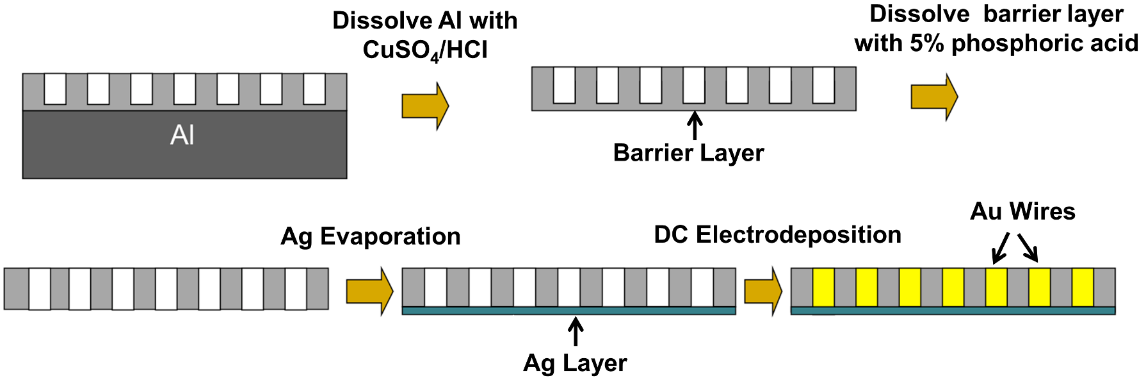

FIGURE 5-5: Schematic of the AAO membrane separation and DC electrodeposition process.

Au directly onto the AAO membrane to create a conductive layer resulted in poor adhesion and a >90% failure rate when Au was deposited into the pores,[266] suggesting that an adhesion layer may be necessary. As subsequent attempts to repeat this experiment resulted in more broken membranes, efforts were shifted to the other two techniques instead.

AC Electrodeposition

The second method investigated was AC electrodeposition of gold. The major advantage of this method is that it does not require removal of the barrier layer, resulting in fewer steps and a more stable membrane. The insulating barrier layer acts as a diode, conducting current preferentially in the cathodic direction. This rectification allows metal ions to be reduced during the cathodic half-cycles while preventing re-oxidation during the anodic half-cycles.[267] However, optimal conditions are highly dependent on solution composition and template,[268] making it difficult to determine effective parameters. Thinning the barrier layer first, as mentioned above, does improve deposition outcomes.

AC electrodeposition was performed at 10 to 20 V peak-to-peak at frequencies ranging from 250 to 750 Hz. Membranes were imaged using SEM to determine the efficacy of deposition. AC electrodeposition utilizing the thicker anodized flattened Al pellets was unsuccessful. One trial of sixteen resulted in wires, shown in Figure 5-6.

The observed wires were uniform and filled the pores completely without the superfluous surface coverage seen when using the PC membranes. However, only a small fraction of the pores were filled. These roughly circular patches of wire growth were scattered throughout the membrane, but even within these areas many pores remain empty. This phenomenon was previously reported for AC copper wire electrodeposition,[267] and the non-homogeneous growth could be a result of inadequate pore wetting, despite sonication performed prior to deposition. The high aspect ratio of the pores hinders mass transport, making it difficult for solution to reach the bottom. These results could also be due to local variations in the barrier

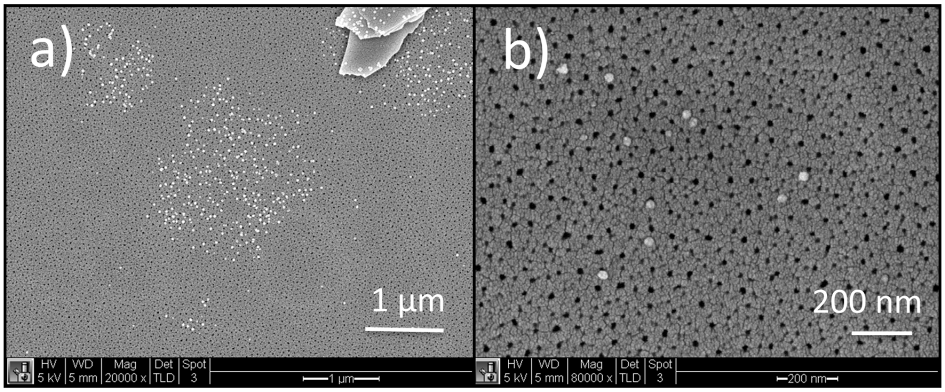

FIGURE 5-6: SEM images of wires grown in an AAO membrane by AC electrodeposition at 20 V (peak-to-peak) and 250 Hz for 5 h.

layer. Gerein and Haber point out that AC electrodeposition is a complicated process because the barrier layer structure may not be well-defined after the voltage thinning process and can change during the course of deposition,[267] thus impacting wire growth. As higher voltages can degrade the membrane,[268] this could also result in a damaged barrier layer. When these conditions were repeated, no pores were filled. A series of new membranes of the same size were made under the exact same anodization and pre-treatment conditions to try to promote consistency of the barrier layer. The voltage was lowered to 10 V peak-to-peak in successive trials to avoid potential barrier layer damage; however, no wires were observed. The frequency was also increased to 500 Hz and 750 Hz in subsequent runs. While there was no resulting wire growth at either frequency, 750 Hz proved to be too high and compromised membrane integrity. It was thought that the additional KCl added to the Orotemp gold solution might actually be a detriment to wire growth. However, removing this did not seem to have any effect, as wires were not produced in any of the six trials done without it. A lower concentration of gold was also explored (25:75 Orotemp gold plating solution/H_2O), but no difference was detected. Deposition time was also increased up to 40 h with no effect.

Cathodic Polarization Followed by DC Electrodeposition

The last technique explored was cathodic polarization followed by DC electrodeposition. In this method, the barrier layer is removed by applying a negative potential to the membrane after anodization and stepwise voltage reduction. This generates OH^- ions at the bottom of the pores as H^+ ions are reduced to H_2 gas at the cathode. These OH^- ions dissolve the surrounding aluminum oxide according to the reaction below as they travel toward the anode.[265]

$$Al_2O_3 + 2OH^- \Longrightarrow 2AlO_2^- + H_2O \tag{5.1}$$

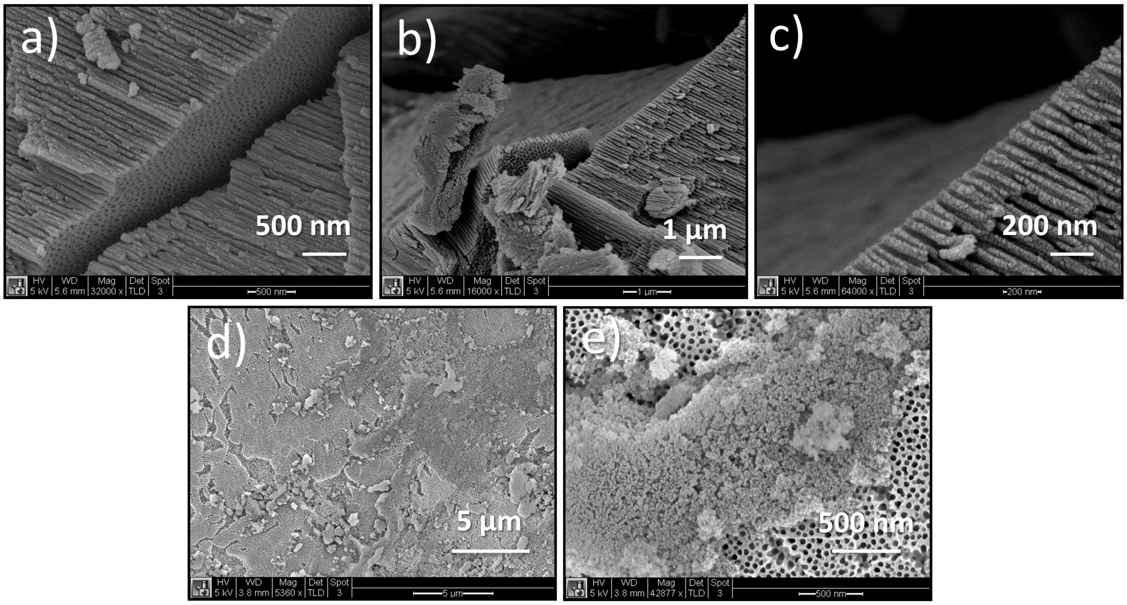

FIGURE 5-7: SEM cross-sections showing barrier layer removal (a-c) and top views (d and e) of an AAO membrane after cathodic polarization at -4 V for 13 min and DC electrodeposition of Au at -1.1 V for 3.5 h.

$$H^+ + AlO_2^- + H_2O \Longrightarrow Al(OH)_3 \tag{5.2}$$

Unlike pore widening in phosphoric acid, which etches the bottom and side walls of the pores at the same rate, cathodic polarization preferentially dissolves the aluminum oxide at the bottom of the pores at a faster rate than the pore walls, enabling dissolution of the barrier layer without destroying the structural integrity of the membrane.[264] While the first attempt using thicker Al samples resulted in visible membrane destruction, no obvious damage was observed when the procedure was repeated in an ice bath, consistent with reported findings that low temperatures prevent over etching of the AAO pore structure.[261] Subsequent experiments with the thinner Al membranes were conducted at -2.25 V for between 5 and 30 min.[265]

After cathodic polarization, all membranes were soaked in 5% phosphoric acid at 30-35 °C for 30 min to widen the pores and remove any remaining barrier layer.[264] They were then sonicated to wet the pores prior to deposition. SEM cross-section images in Figure 5-7 reveal that the barrier layer appears to have been successfully dissolved using the cathodic polarization method. However, electrodeposition for 3.5 h did not produce an ordered array of nanowires. Instead, significant surface coverage was observed in some areas of the membrane, similar to that seen with the PC membranes. This could be a result of wire overgrowth, but the non-uniformity again suggests inconsistency in the electric field, perhaps caused by irregularities in the barrier layer which could have remained in some areas.

Deposition times were increased significantly (up to 48 h) after gold deposition took much

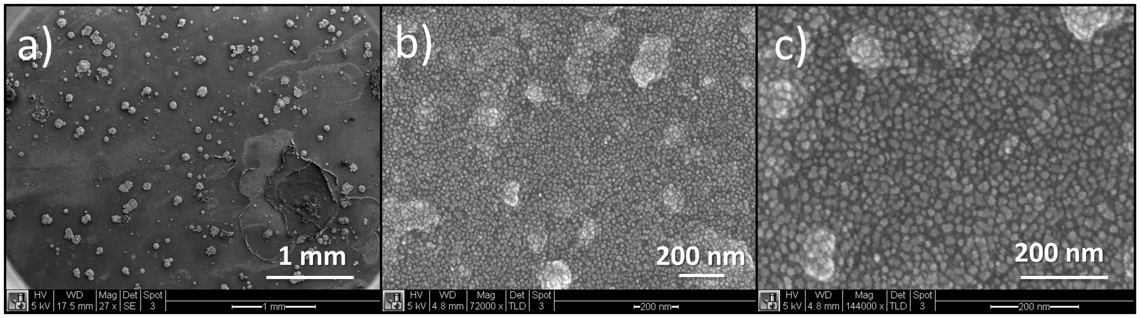

FIGURE 5-8: SEM images of an AAO membrane showing Au wire growth after cathodic polarization at -2.25 V for 30 min and DC electrodeposition of Au at -1.1 V for 45 h.

longer than anticipated during macroscale tests. Of twelve trials, only one produced uniform Au wires in the pores (Figure 5-8), and it was run at a longer deposition time of 45 h. The pore fill percentage appears to be quite high with minimal surface contamination. The same voltage thinning, cathodic polarization, and electrodeposition conditions were repeated three more times in an attempt to replicate the wires observed in Figure 5-8. While one experiment produced areas of the membrane that were covered by possible wire overgrowth, none resulted in the same uniform wires.

Results from another trial are shown in Figure 5-9. After Au deposition, the entire membrane is completely broken down, revealing two distinct layers (Figure 5-9b). The top opaque layer is comprised of mostly fibrous alumina wires with occasional small sections of porous membrane (Figure 5-9c, d, g, and h), while the layer underneath contains an imprint of the porous membrane with shallow pores (Figure 5-9). When the top membrane was lifted off of the surface and imaged separately, it looked quite different, containing no alumina wires, but only perfectly ordered pores (Figure 5-9e). Perhaps the wires are firmly attached to the bottom Al surface or totally detached from both surfaces, allowing the isolated removal of the porous membrane. Interestingly, the pores in Figure 5-9e and f appear more ordered than those produced by the initial anodization.

Improved pore ordering was also seen in another membrane run at similar conditions, shown in Figure 5-10. This suggests that some degree of pore rearrangement is occurring during the deposition process, but this is still under investigation. The applied potential was lowered slightly in subsequent experiments to avoid damaging the membrane, but breakdown was still observed.

Membrane separation and degradation occurred in nearly all of the membranes prepared by cathodic polarization and DC electrodeposition, suggesting that one of these steps is instrumental in this process. Long DC electrodeposition times are likely a major contributor for a number of reasons. First, the only trials that did not result in this degradation were run for shorter deposition durations but at similar cathodic polarization conditions. Addi-

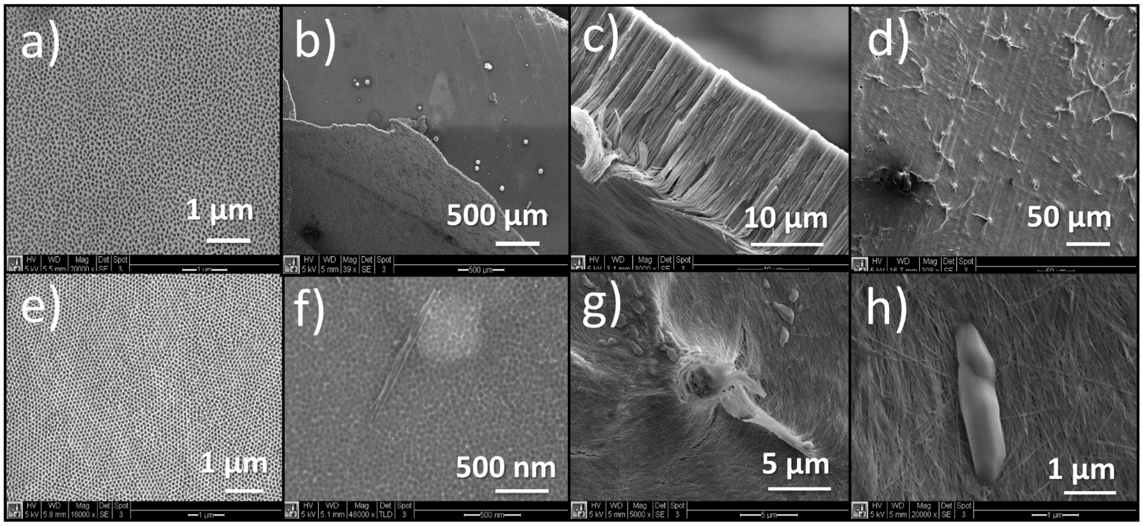

FIGURE 5-9: SEM images of an AAO membrane before (a) and after (b through h) cathodic polarization at -2.25 V for 30 min and DC electrodeposition of Au at -1.1 V for 41 h. (b) shows two layers of the membrane while (c) shows the edge of the top layer and (f) shows the bottom layer. (e) is the top layer after it has been separated completely from the rest of the membrane. (d, g, and h) are top-down views.

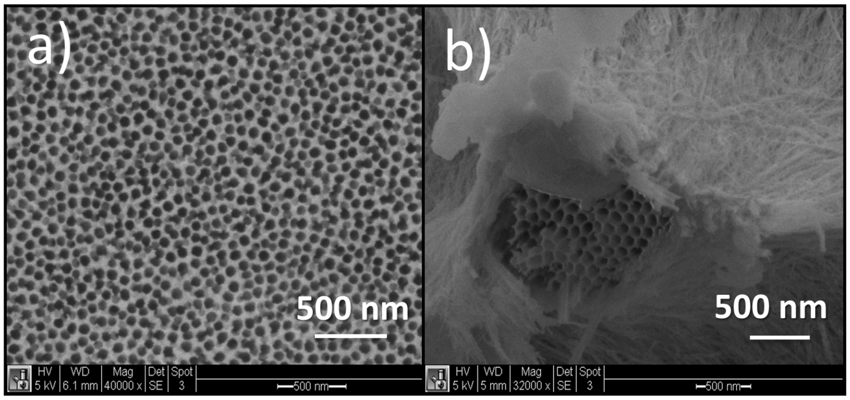

FIGURE 5-10: SEM images of an AAO membrane before (a) and after (b) cathodic polarization at -2.25 V for 30 min and DC electrodeposition of Au at -0.9 V for 48 h, showing increased pore ordering.

tionally, SEM images of another membrane from this set, shown in Figure 5-11, indicate that the porous membrane was still intact after cathodic polarization (Figure 5-11b), with the only change being an increased pore size caused by the phosphoric acid pore widening step. After deposition, however, the membrane was destroyed, leaving behind fibrous alumina wires (Figure 5-11c). As further evidence, shortening the cathodic polarization time did not seem to prevent membrane breakdown.

Other factors such as barrier layer and membrane composition may also play a role. Zhang and coworkers have reported the production of alumina wires rather than pores under certain anodization temperatures and voltages.[269] They propose that under these particular condi-

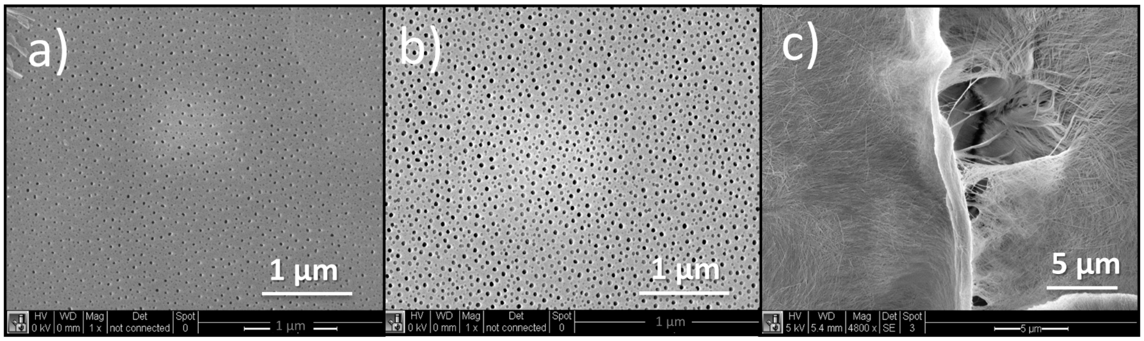

FIGURE 5-11: SEM images of an AAO membrane before cathodic polarization (a), after cathodic polarization at -2.25 V for 10 min (b), and after DC electrodeposition of Au at -0.9 V for 48 h (c).

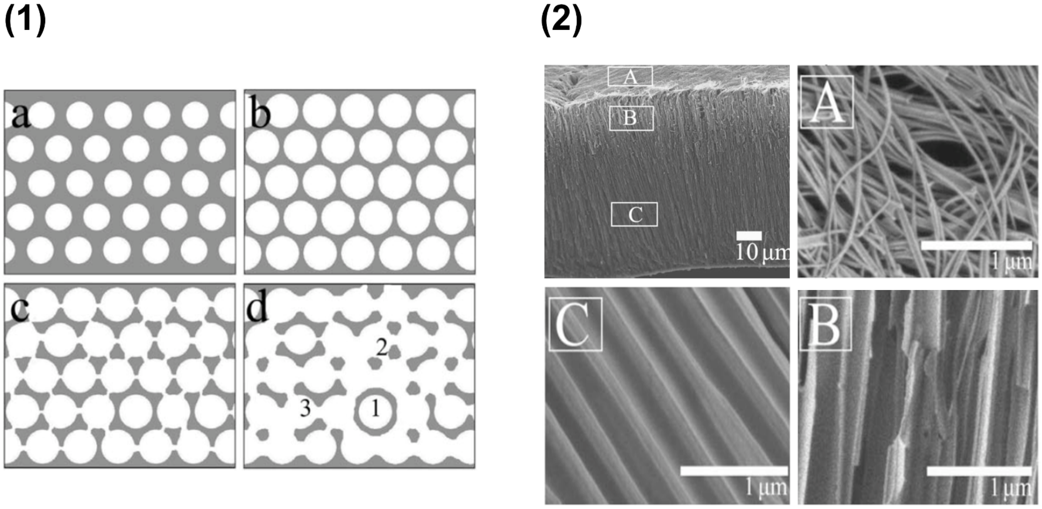

FIGURE 5-12: **(1)** Top-view diagram of possible formation stages of alumina nanowires. a) Porous AAO membrane. b) Pore walls are thinned by slow dissolution. c) Perforations are formed. d) Alumina nanotubes (1), nanowires (2), and nanofascias (3) are created. **(2)** SEM cross-section images of an anodized aluminum oxide membrane. Top left: overview, A) alumina nanowires, B) transition layer, C) alumina nanochannels. Taken from ref. 269.

tions, the channel walls begin to break down near the surface, which results in a high electrical field at these edges that increases dissolution. Depending on how neighboring pores dissolve, nanotubes, nanowires, or nanofascias are produced (Figure 5-12). Although they used much higher voltages and a different anodizing electrolyte, they report a cross-section (Figure 5-12) similar to the structure we observed in Figure 5-9, with a layer of alumina nanowires on top of the normally observed hexagonal pore structure, bridged by a transition layer. Since anodization conditions affect barrier layer and membrane characteristics, these results support the proposed importance of these factors.

In addition, Shaban *et al.* mention that it is difficult to entirely dissolve the barrier layer by cathodic polarization without destroying the membrane if it is thicker than 20 μm.[264] Thicker

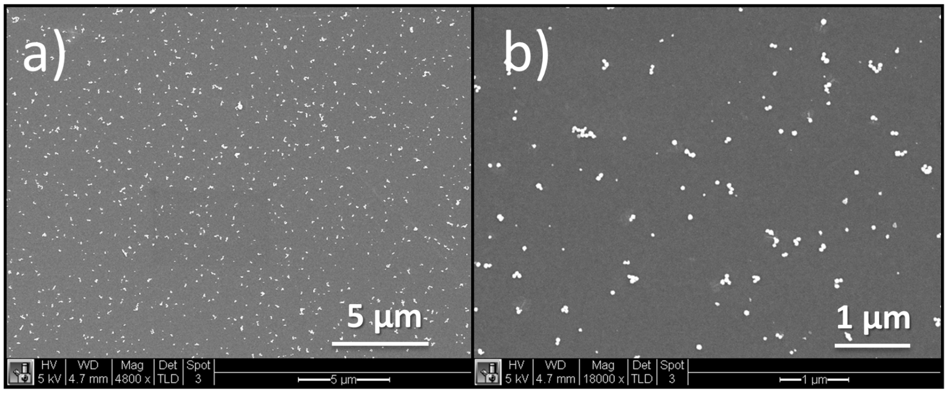

FIGURE 5-13: SEM images of an AAO membrane after cathodic polarization at -2.25 V for 5 min and DC electrodeposition of Au at -0.9 V for ∼24.5 h. This sample was anodized for a shorter time period (3 h) to decrease the membrane thickness.

membranes also make it more difficult for the gold electroplating solution to adequately wet the pores. Membranes grown on the thin Al are estimated to be around 20 μm thick, based on Figure 5-9c. To explore the effect of total membrane thickness, the anodization time was cut in half to yield a thinner membrane with smaller pores. The phosphoric acid soaking time was doubled to further widen the pores and compensate for their small size. Electrodeposition was done for only ∼24.5 h because of the relatively short pore length. Results are shown in Figure 5-13. Small gold structures appear to be protruding from the surface, which could be a result of wires overgrowing the top of the pores. There are fewer pores than in previous membranes, which is consistent with a shorter anodization time, but there does not appear to be any significant membrane damage even though the electrodeposition time was relatively long, suggesting that membrane thickness and composition do play a role.

Sousa and co-workers recently published work highlighting the importance of barrier layer thickness on DC electrodeposition.[270] They tested thicknesses from 2 to 16 nm and found that the optimal barrier layer thickness is 10 nm, with even very slight variations in thickness leading to dramatically different fill percentages, ranging from 5 to over 95%. They state that very thin barrier layers produce local variations that cause deposition to preferentially occur in certain pores. Conversely, thicker barrier layers require high applied potentials to penetrate the oxide layer, leading to high current density that causes dielectric breakdown at thinner regions. High current density in both cases can result in hydrogen evolution that inhibits nanowire growth. Although their procedure differs from ours in that they did not completely remove the barrier layer but only thinned it before deposition, and they used pulsed DC electrodeposition, their findings still apply. It is possible that in many of our trials, cathodic polarization did not completely dissolve the barrier layer in all areas but decreased it until it was very thin, causing variations in the thickness that resulted in preferential pore filling in those areas with little or no barrier layer. The increased current density in these pores could have led to barrier layer and membrane breakdown, and hydrogen production could have contributed to decreased nanowire growth.

From these observations, it was concluded that barrier layer removal and electrodeposition of gold into the pores of AAO membranes require a delicate balance between a number of parameters, necessitating precise control over anodization conditions, barrier layer thickness, and deposition time. Published procedures use a wide variety of starting aluminum surface areas and thicknesses, anodization times, and barrier layer thinning conditions, any of which could contribute to differences in barrier layer morphology or surrounding membrane structure that can affect wire growth. In addition, many papers report using commercially produced alumina membranes from Whatman,[271–273] which, while expensive, likely have much more uniform structures than homemade ones. Many different Au deposition potentials have also been reported,[274–276] while many other papers do not state the applied potential or deposition time[265,266,275,277–279] and use a variety of gold electroplating solutions,[274,275,277] making it difficult to reproduce results.

5.3 Electroless Deposition by Chemical Reduction

Electroless deposition is typically accomplished by direct chemical reduction and has several advantages over electrodeposition. Most notably, it does not require a direct electrical connection, thereby simplifying the experimental setup and eliminating concerns about inconsistent electrical contact between the membrane and the working electrode. It also provides an additional benefit for the preparation of bipolar arrays in particular because the resulting array is fully accessible to the solution on both sides without requiring the removal of a conductive working electrode layer (as is necessary with the electrodeposition method discussed above). However, this experimental design offers less direct control over the deposition rate due to the absence of an applied potential. There are many reports of electroless deposition of gold into polycarbonate membranes,[47,48,50] but the work presented here is based on a simple technique reported by Wong *et al.*,[205,206] in which solutions of a metal precursor ion and a reducing agent are added to opposite sides of a PC membrane template and allowed to meet inside the pores. The metal ions are reduced on contact, and growth continues until the pores are blocked or transport becomes too hindered to allow the solutions to mix freely.

As noted earlier, wetting the membrane is key to achieving homogeneous deposition. Therefore, the membrane was first sonicated in methanol for 1 min and then soaked in methanol and water for 15 min each to facilitate solution transport. It was then inserted between two halves of a homemade diffusion cell in a vertical orientation, using an O-ring to provide a leakproof seal (Figure 5-14a). The reduction reaction was initiated by adding 50 mM $HAuCl_4$ to one side of the cell and 0.25 M $NaBH_4$ (in water) to the other. The relative concentrations of metal ion precursor and reducing agent are important in determining the integrity of the

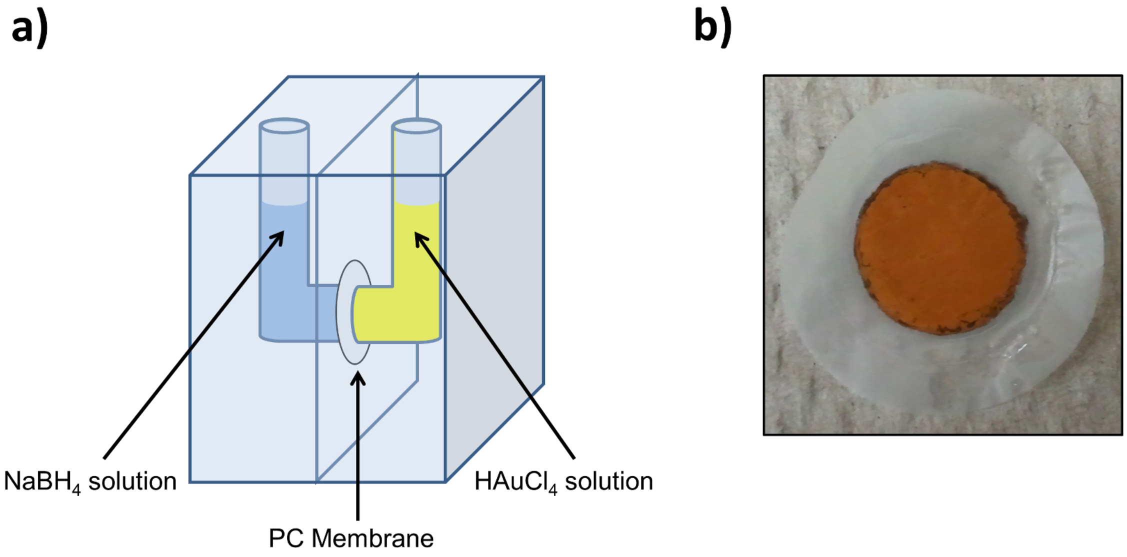

FIGURE 5-14: a) Diagram of the diffusion cell used to fabricate gold nanowire arrays via direct chemical reduction. b) Photograph of a membrane after a successful deposition.

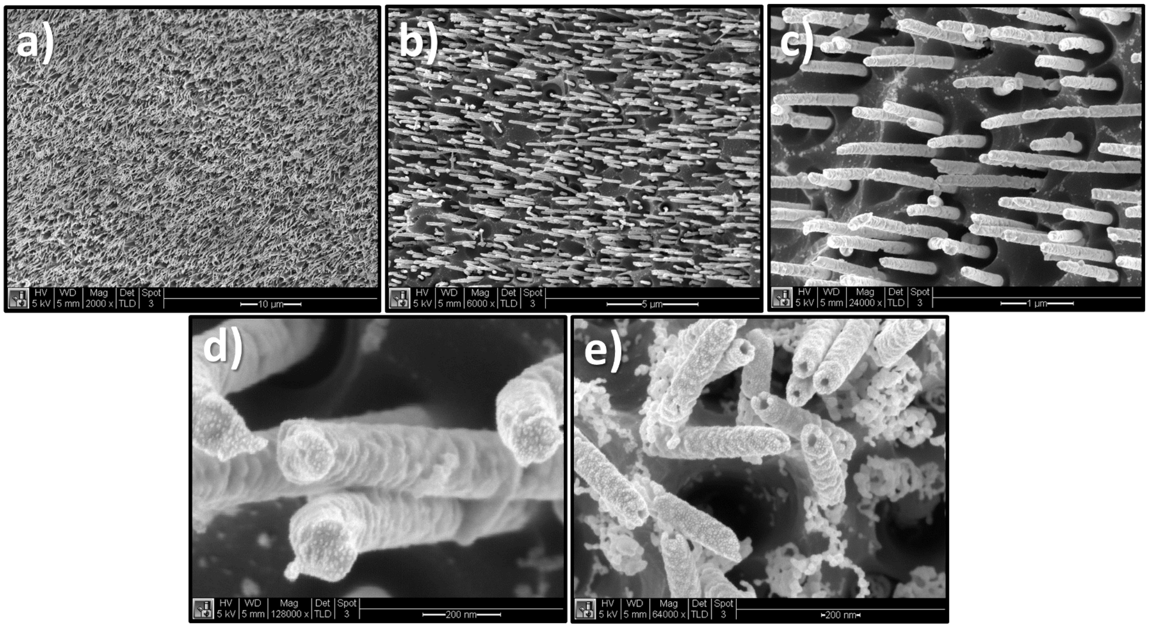

FIGURE 5-15: (a-d) SEM images of wires grown by direct chemical reduction of 50 mM$HAuCl_4$ by 0.25 M $NaBH_4$ (in water) for 1 h inside the 100-nm-diameter pores of a PC membrane. The surface layer was removed, and the membrane was etched for 20 min using oxygen plasma before imaging. e) SEM image of hollow nanowires produced by the same method using 0.5 M $NaBH_4$ instead.

wires, as noted by Wong and coworkers.[205] If the concentration of $NaBH_4$ is too high, there are too many nucleation sites, and growth proceeds quickly through the pores, producing porous nanowires like those shown in Figure 5-15e, for which 0.5 M $NaBH_4$ was used. We found that concentrations of 50 mM $HAuCl_4$ and 0.25 M $NaBH_4$ provide an appropriate ratio for solid nanowire growth. Deposition is allowed to proceed for $\sim$1 h, after which the membrane is removed from the cell and washed several times with water. Figure 5-14b shows a photograph of a completed nanowire array. A relatively homogeneous overgrowth of gold can be seen on the top surface, confirming the success of the deposition. This layer can easily be removed by wiping the surface with a Kimwipe.

SEM images of a gold nanowire array deposited for 1 h are shown in Figure 5-15a-d. After removing the overgrowth, the membrane was etched for 20 min using oxygen plasma to enable clear observation of the nanowire array. These images reveal a uniform array of closely-packed nanowires. Almost every pore is filled, and magnified images confirm that the wires are solid. Since the PC membrane pores are somewhat randomly distributed, this method would benefit from the use of a more ordered starting template. In addition, uniformity could likely be improved by applying an electric field during the growth process (as described in Chapter 2 for a single wire), which would provide greater control over the deposition rate by tuning mass transport. However, we have shown that this technique is fast, simple, and reproducible and is a good choice for array fabrication.

5.4 Conclusions

Controlling mass transport is essential for producing uniform nanowire arrays. Inhomogeneous electric fields caused by irregular working electrode surfaces or inadequate pore wetting can significantly affect the transport of metal ion precursors to the deposition site and require careful attention. We tested many different experimental parameters for gold electrodeposition in nanoporous templates. While some nanowires were produced by electrodeposition in both PC and AAO membranes, wire growth in both materials suffered from widespread inconsistency, likely due to asymmetries in the electric field associated with a nonuniform template and/or working electrode structure. Conversely, preparation of gold nanowire arrays by electroless deposition proved to be quite successful. We were able to produce uniform arrays with high fill percentages by employing a previously reported method in which solutions of a metal ion precursor ($HAuCl_4$) and a reducing agent ($NaBH_4$) are placed on opposite sides of a PC membrane and allowed to mix inside the pores, depositing gold by chemical reduction on contact. Improvements to the uniformity of the starting template and control over the deposition rate via application of an electric field during growth should yield gold nanowire arrays capable of measuring electrochemical processes with high spatial and temporal resolution for a variety of bipolar sensing applications.

CHAPTER 6

Conclusions

IN SUMMARY, the work presented in this dissertation has explored the interplay between electrochemistry and transport dynamics under confinement. As the characteristic length scale of electrochemical investigations decreases, transport behavior becomes increasingly important, necessitating a better fundamental understanding of the forces and properties that govern it. However, electrical, material, and hydrodynamic effects are intricately intertwined in these systems, presenting a considerable challenge for predicting, interpreting, and controlling nanoscale behavior. We have endeavored to both probe and control transport dynamics in cylindrical silica nanochannels and other confined spaces using electrochemical techniques.

We first described the development of a wireless method for dynamic *in situ* control of metal nanowire growth in a silica nanochannel template. Initial deposition occurs by direct chemical reduction of a metal precursor ion by a reducing agent until the pore is blocked, after which a bipolar mechanism enables continued growth through coupled oxidation and reduction reactions at either end of the growing wire. While the shape and dimensions of the template itself impose advantageous restrictions on mass transport, applying an electric field during the growth process provides the unique ability to tune this transport and the corresponding deposition rate as the wire grows. This method is highly reproducible and produces high-quality gold nanowires that can be used as bipolar nanoelectrodes or components for sensors and other devices.

Next, we reported the anomalous size- and material-dependent transport behavior of polystyrene and silica nanoparticles traveling through silica nanochannels. Interestingly, in a solution containing equal concentrations of two different particle sizes, small silica particles are detected far more frequently than large ones, as expected from geometric limitations, while large polystyrene particles show the opposite trend. We examined the roles of several different factors, including driving forces and charge effects, in order to better understand the mechanism of this observed selectivity, concluding that selection happens outside the channel and is not caused by simple driving forces. While we are uncertain as to the exact cause of this behavior, our results indicate that subtle charge effects likely play a role, perhaps as they relate to the interfacial structure surrounding the particle and the channel walls or the relative polarizability of the particles. These properties are quite different for silica particles, which are hydrophilic, and polystyrene particles, which possess a mixed hydrophilic/hydrophobic surface. Most importantly, this investigation demonstrates that nanoscale effects can have a significant influence on mesoscale transport behavior when the particle diameter is comparable to the channel diameter. This has significant implications for controlling transport in natural and synthetic nanoporous systems, which are important in many different fields, including biology, separation science, geochemistry, and energy materials.

We also summarized efforts to develop new methods for the fabrication of gold nanoelectrodes based on two reported techniques—nanoskiving and lithographically patterned nanowire electrodeposition (LPNE). These methods offer many practical advantages for both the synthesis and applications of gold nanoelectrodes, and we were successful in producing a few functional electrodes. However, the reproducibility was low and remains an issue. The last chapter discussed the preparation of uniform gold nanowire arrays for bipolar sensing applications, focusing on the challenges surrounding traditional electrodeposition techniques in polycarbonate and anodized aluminum oxide membranes and the success of using a published electroless deposition technique. We were able to achieve uniform arrays by placing solutions of $HAuCl_4$ and $NaBH_4$ on opposite sides of a polycarbonate template and allowing them to meet inside the pores, depositing gold on contact. Further improvements could be made by employing a more ordered template and using a potential to control the transport dynamics during growth (as we did for the single wire in Chapter 2).

Nanoscale transport dynamics involve the complex coordination of several different competing and cooperating forces, and much remains to be understood concerning these interactions. However, this work demonstrates the immense potential for leveraging these unique effects to precisely tune mass transport, with a dual purpose of gaining a deeper fundamental understanding of confined electrochemical behavior and developing exciting new methods for nanostructure synthesis and characterization.

Appendix A

Silica Nanochannel Fabrication

The majority of the work described in this dissertation (Chapters 2 & 3) was performed using cylindrical silica nanochannels. These channels are robust, reproducible, and can be controllably fabricated with a variety of dimensions. While the nanochannels used in our experiments typically had diameters between 200-700 nm and lengths between 6-40 μm, channels with diameters as small as 20 nm can be made using this method. These properties make them ideal for investigating nanoscale transport in confined spaces. Therefore, in this appendix, we provide a detailed description of the fabrication method used to produce these nanochannels.

A.1 Nanopipette Preparation

To simplify this section, we first state that the silica microcapillary was purchased from Polymicro, Inc., and all other capillaries and both micropipette pullers were obtained from Sutter Instrument Company. Figure A-1 illustrates the steps involved in nanochannel fabrication. To begin, the polymer coating is burned off of a section of silica microcapillary (o.d. = 0.35 mm, i.d.= 20 μm) by passing it through the flame of a Bunsen burner. A small piece of this microcapillary ($\sim$ 2 cm) is then inserted into the middle of a larger silica capillary (o.d. = 1.0 mm, i.d.= 0.3 mm) and placed in a laser-based P-2000 micropipette puller. The mechanical arms of the puller are prevented from moving using a homemade aluminum clamp, allowing the heat from the laser to melt the glass without pulling it. One end of the outer capillary is sealed using the following program: heat = 830 / filament = (blank) / velocity = 100 / delay = 255 / pull = (blank). Next, a hole is poked in a small rubber pipette bulb, which is attached to one end of the outer capillary and connected via a hose to a vacuum pump. Multiple heating and cooling cycles (typically 30 s on, 40 s off) are then performed under vacuum in order to seal the inner capillary and shrink its diameter using the following program: heat = 870 / filament = 5 / velocity = 100 / delay = 255 / pull = 255. The number of cycles required varies depending

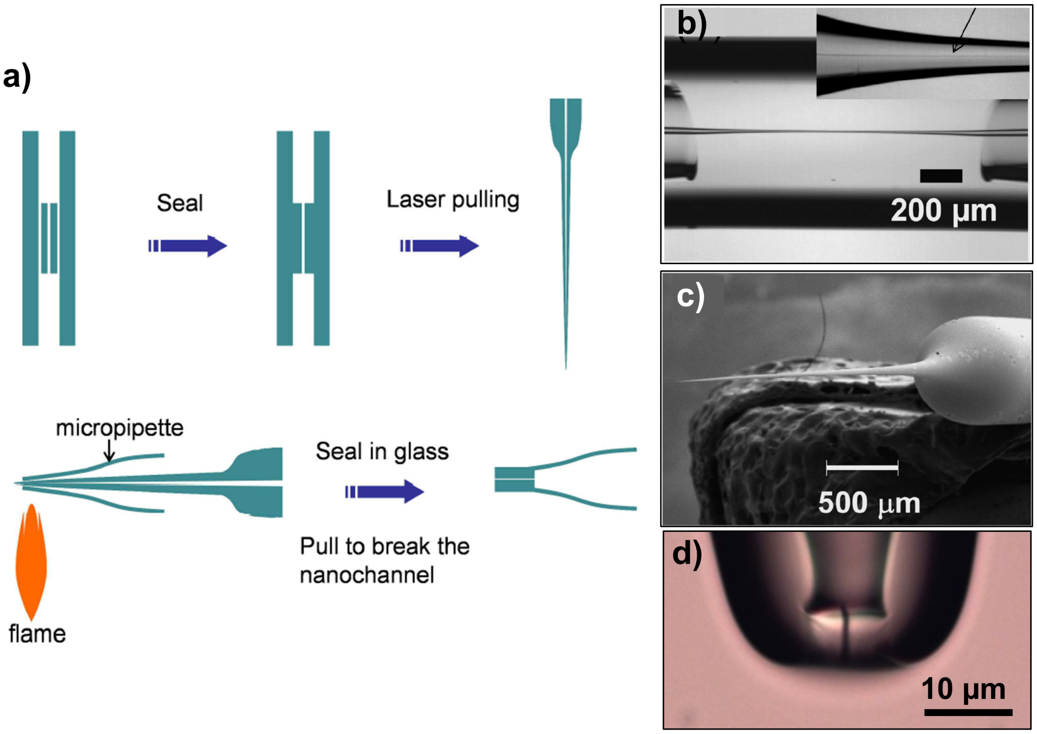

FIGURE A-1: a) Schematic of the silica nanochannel fabrication method. b) Optical microscope image of a microcapillary sealed inside a larger outer capillary before pulling. The inset shows an optical microscope image of the nanopipette after pulling. c) SEM image of a nanopipette tip. d) Optical microscope image of a completed nanochannel.

on the desired final diameter but is usually around four. The inner capillary diameter can be checked after several cycles using a portable microscope. When the diameter has decreased to about 5 μm (or smaller depending on the desired channel dimensions), the vacuum line and aluminum clamp are removed and the capillary ensemble is pulled into two sharp nanopipette tips using the following program: heat = 870 / filament = 3 / velocity = 80 / delay = 140 / pull = 220. A representative SEM image of one of these nanopipettes is shown in Figure A-1c.[208]

A.2 Nanochannel Fabrication

A portion of this nanopipette tip is next sealed inside an outer microcapillary for stability. This support capillary is created by pulling a larger borosilicate capillary (o.d. = 2.0 mm, i.d.= 1.16 mm) into a blunt tip using the filament-based P-97 micropipette puller according to the following program: heat = 520 / pull = 0 / velocity = 8 / delay = 225. A nanopipette tip is then carefully inserted into this larger support capillary under the microscope until it is seen protruding from the other end by about 5 μm. The whole ensemble is passed quickly through a Bunsen burner flame to seal a small piece of the inner nanopipette to the walls of the support capillary. The remainder of the nanopipette is then removed, leaving a short section containing the nanochannel sealed inside the larger outer capillary. The protruding end of the channel is easily removed by contacting it gently with a razor blade. Figure A-1d shows an optical microscope image of a finished nanochannel. While these steps require practice and a certain degree of finesse, nanochannels of different aspect ratios can be reliably produced using this method.

References

[1] A. J. BARD, F. R. F. FAN, J. KWAK, & O. LEV. Scanning electrochemical microscopy. introduction and principles. *Analytical Chemistry* **61 (2)**, 132–138 (1989).

[2] S. BERGNER, P. VATSYAYAN, & F.-M. MATYSIK. Recent advances in high resolution scanning electrochemical microscopy of living cells - a review. *Analytica Chimica Acta* **775**, 1–13 (2013).

[3] S. AMEMIYA, A. J. BARD, F.-R. F. FAN, M. V. MIRKIN, & P. R. UNWIN. Scanning electrochemical microscopy. *Annual Review of Analytical Chemistry* **1**, 95–131 (2008).

[4] A. SCHULTE, M. NEBEL, & W. SCHUHMANN. Scanning electrochemical microscopy in neuroscience. *Annual Review of Analytical Chemistry, Vol 3* **3**, 299–318 (2010).

[5] J. J. WATKINS, J. Y. CHEN, H. S. WHITE, H. D. ABRUNA, E. MAISONHAUTE, & C. AMATORE. Zeptomole voltammetric detection and electron-transfer rate measurements using platinum electrodes of nanometer dimensions. *Analytical Chemistry* **75 (16)**, 3962–3971 (2003).

[6] P. SUN & M. V. MIRKIN. Kinetics of electron-transfer reactions at nanoelectrodes. *Analytical Chemistry* **78 (18)**, 6526–6534 (2006).

[7] J. J. WATKINS & H. S. WHITE. The role of the electrical double layer and ion pairing on the electrochemical oxidation of hexachloroiridate (iii) pt electrodes of nanometer dimensions. *Langmuir* **20 (13)**, 5474–5483 (2004).

[8] J. L. CONYERS & H. S. WHITE. Electrochemical characterization of electrodes with submicrometer dimensions. *Analytical Chemistry* **72 (18)**, 4441–4446 (2000).

[9] K. ECKHARD, X. CHEN, F. TURCU, & W. SCHUHMANN. Redox competition mode of scanning electrochemical microscopy (rc-secm) for visualisation of local catalytic activity. *Physical Chemistry Chemical Physics* **8 (45)**, 5359–5365 (2006).

[10] J. L. FERNANDEZ, D. A. WALSH, & A. J. BARD. Thermodynamic guidelines for the design of bimetallic catalysts for oxygen electroreduction and rapid screening by scanning electrochemical microscopy. m-co (m : Pd, ag, au). *Journal of the American Chemical Society* **127 (1)**, 357–365 (2005).

[11] X. Y. XIAO & A. J. BARD. Observing single nanoparticle collisions at an ultramicroelectrode by electrocatalytic amplification. *Journal of the American Chemical Society* **129 (31)**, 9610 (2007).

[12] X. Y. XIAO, S. L. PAN, J. S. JANG, F. R. F. FAN, & A. J. BARD. Single nanoparticle electrocatalysis: Effect of monolayers on particle and electrode on electron transfer. *Journal of Physical Chemistry C* **113 (33)**, 14978–14982 (2009).

[13] Y. LI, J. T. COX, & B. ZHANG. Electrochemical responses and electrocatalysis at single au nanoparticles. *Journal of the American Chemical Society* **132 (9)**, 3047–3054 (2010).

[14] X. Y. XIAO, F. R. F. FAN, J. P. ZHOU, & A. J. BARD. Current transients in single nanoparticle collision events. *Journal of the American Chemical Society* **130 (49)**, 16669–16677 (2008).

[15] R. M. WIGHTMAN, J. A. JANKOWSKI, R. T. KENNEDY, K. T. KAWAGOE, T. J. SCHROEDER, D. J. LESZCZYSZYN, J. A. NEAR, E. J. DILIBERTO, & O. H. VIVEROS. Temporally resolved catecholamine spikes correspond to single vesicle release from individual chromaffin cells. *Proceedings of the National Academy of Sciences of the United States of America* **88 (23)**, 10754–10758 (1991).

[16] D. J. LESZCZYSZYN, J. A. JANKOWSKI, O. H. VIVEROS, E. J. DILIBERTO, J. A. NEAR, & R. M. WIGHTMAN. Nicotinic receptor-mediated catecholamine secretion from individual chromaffin cells - chemical evidence for exocytosis. *Journal of Biological Chemistry* **265 (25)**, 14736–14737 (1990).

[17] S. GE, S. KOSEOGLU, & C. L. HAYNES. Bioanalytical tools for single-cell study of exocytosis. *Analytical and Bioanalytical Chemistry* **397 (8)**, 3281–3304 (2010).

[18] W. WANG, S. H. ZHANG, L. M. LI, Z. L. WANG, J. K. CHENG, & W. H. HUANG. Monitoring of vesicular exocytosis from single cells using micrometer and nanometer-sized electrochemical sensors. *Analytical and Bioanalytical Chemistry* **394 (1)**, 17–32 (2009).

[19] M. ONGARO & P. UGO. Bioelectroanalysis with nanoelectrode ensembles and arrays. *Analytical and Bioanalytical Chemistry* **405 (11)**, 3715–3729 (2013).

[20] J. I. YEH & H. B. SHI. Nanoelectrodes for biological measurements. *Wiley Interdisciplinary Reviews-Nanomedicine and Nanobiotechnology* **2 (2)**, 176–188 (2010).

[21] M. Silvestrini, L. Fruk, & P. Ugo. Functionalized ensembles of nanoelectrodes as affinity biosensors for dna hybridization detection. *Biosensors & Bioelectronics* **40 (1)**, 265–270 (2013).

[22] L. Cao, P. Yan, K. Sun, & D. W. Kirk. Gold 3d brush nanoelectrode ensembles with enlarged active area for the direct voltammetry of daunorubicin. *Electroanalysis* **21 (10)**, 1183–1188 (2009).

[23] A. Mardegan, P. Scopece, F. Lamberti, M. Meneghetti, L. M. Moretto, & P. Ugo. Electroanalysis of trace inorganic arsenic with gold nanoelectrode ensembles. *Electroanalysis* **24 (4)**, 798–806 (2012).

[24] R. B. Morris, D. J. Franta, & H. S. White. Electrochemistry at pt band electrodes of width approaching molecular dimensions. breakdown of transport equations at very small electrodes. *Journal of Physical Chemistry* **91 (13)**, 3559–3564 (1987).

[25] S. L. Chen & A. Kucernak. Fabrication of carbon microelectrodes with an effective radius of 1 nm. *Electrochemistry Communications* **4 (1)**, 80–85 (2002).

[26] S. L. Chen & A. Kucernak. The voltammetric response of nanometer-sized carbon electrodes. *Journal of Physical Chemistry B* **106 (36)**, 9396–9404 (2002).

[27] D. Krapf, B. M. Quinn, M.-Y. Wu, H. W. Zandbergen, C. Dekker, & S. G. Lemay. Experimental observation of nonlinear ionic transport at the nanometer scale. *Nano Letters* **6 (11)**, 2531–2535 (2006).

[28] Y. Sun, Y. Liu, Z. Liang, L. Xiong, A. Wang, & S. Chen. On the applicability of conventional voltammetric theory to nanoscale electrochemical interfaces. *Journal of Physical Chemistry C* **113 (22)**, 9878–9883 (2009).

[29] C.-C. Chen, Y. Zhou, & L. A. Baker. Scanning ion conductance microscopy. *Annual Review of Analytical Chemistry, Vol 5* **5**, 207–228 (2012).

[30] P. Happel, D. Thatenhorst, & I. D. Dietzel. Scanning ion conductance microscopy for studying biological samples. *Sensors* **12 (11)**, 14983–15008 (2012).

[31] M. J. Lab, A. Bhargava, P. T. Wright, & J. Gorelik. The scanning ion conductance microscope for cellular physiology. *American Journal of Physiology-Heart and Circulatory Physiology* **304 (1)**, H1–H11 (2013).

[32] F. Anariba, J. H. Anh, G.-E. Jung, N.-J. Cho, & S.-J. Cho. Biophysical applications of scanning ion conductance microscopy (sicm). *Modern Physics Letters B* **26 (5)** (2012).

[33] M. DAVENPORT, K. HEALY, M. PEVARNIK, N. TESLICH, S. CABRINI, A. P. MORRISON, Z. S. SIWY, & S. E. LETANT. The role of pore geometry in single nanoparticle detection. *ACS Nano* **6 (9)**, 8366–8380 (2012).

[34] W. J. LAN, D. A. HOLDEN, B. ZHANG, & H. S. WHITE. Nanoparticle transport in conical-shaped nanopores. *Analytical Chemistry* **83 (10)**, 3840–3847 (2011).

[35] J.-L. FRAIKIN, T. TEESALU, C. M. MCKENNEY, E. RUOSLAHTI, & A. N. CLELAND. A high-throughput label-free nanoparticle analyser. *Nature Nanotechnology* **6 (5)**, 308–313 (2011).

[36] Y. X. WANG, K. KECECI, M. V. MIRKIN, V. MANI, N. SARDESAI, & J. F. RUSLING. Resistive-pulse measurements with nanopipettes: detection of au nanoparticles and nanoparticle-bound anti-peanut igy. *Chemical Science* **4 (2)**, 655–663 (2013).

[37] L. T. SEXTON, L. P. HORNE, S. A. SHERRILL, G. W. BISHOP, L. A. BAKER, & C. R. MARTIN. Resistive-pulse studies of proteins and protein/antibody complexes using a conical nanotube sensor. *Journal of the American Chemical Society* **129 (43)**, 13144–13152 (2007).

[38] S. R. GERMAN, L. LUO, H. S. WHITE, & T. L. MEGA. Controlling nanoparticle dynamics in conical nanopores. *Journal of Physical Chemistry C* **117 (1)**, 703–711 (2013).

[39] T. ITO, L. SUN, & R. M. CROOKS. Simultaneous determination of the size and surface charge of individual nanoparticles using a carbon nanotube-based coulter counter. *Analytical Chemistry* **75 (10)**, 2399–2406 (2003).

[40] T. ITO, L. SUN, M. A. BEVAN, & R. M. CROOKS. Comparison of nanoparticle size and electrophoretic mobility measurements using a carbon-nanotube-based coulter counter, dynamic light scattering, transmission electron microscopy, and phase analysis light scattering. *Langmuir* **20 (16)**, 6940–6945 (2004).

[41] L. J. STEINBOCK, G. STOBER, & U. F. KEYSER. Sensing dna-coatings of microparticles using micropipettes. *Biosensors & Bioelectronics* **24 (8)**, 2423–2427 (2009).

[42] L. BACRI, A. G. OUKHALED, B. SCHIEDT, G. PATRIARCHE, E. BOURHIS, J. GIERAK, J. PELTA, & L. AUVRAY. Dynamics of colloids in single solid-state nanopores. *Journal of Physical Chemistry B* **115 (12)**, 2890–2898 (2011).

[43] U. S. MOHANTY. Electrodeposition: a versatile and inexpensive tool for the synthesis of nanoparticles, nanorods, nanowires, and nanoclusters of metals. *Journal of Applied Electrochemistry* **41 (3)**, 257–270 (2011).

[44] M. L. TIAN, J. U. WANG, J. KURTZ, T. E. MALLOUK, & M. H. W. CHAN. Electrochemical growth of single-crystal metal nanowires via a two-dimensional nucleation and growth mechanism. *Nano Letters* **3 (7)**, 919–923 (2003).

[45] M. E. TOIMIL-MOLARES. Characterization and properties of micro- and nanowires of controlled size, composition, and geometry fabricated by electrodeposition and ion-track technology. *Beilstein Journal of Nanotechnology* **3**, 860–883 (2012).

[46] S. KARIM, M. E. TOIMIL-MOLARES, F. MAURER, G. MIEHE, W. ENSINGER, J. LIU, T. W. CORNELIUS, & R. NEUMANN. Synthesis of gold nanowires with controlled crystallographic characteristics. *Applied Physics a-Materials Science & Processing* **84 (4)**, 403–407 (2006).

[47] V. P. MENON & C. R. MARTIN. Fabrication and evaluation of nanoelectrode ensembles. *Analytical Chemistry* **67 (13)**, 1920–1928 (1995).

[48] M. DE LEO, F. C. PEREIRA, L. M. MORETTO, P. SCOPECE, S. POLIZZI, & P. UGO. Towards a better understanding of gold electroless deposition in track-etched templates. *Chemistry of Materials* **19 (24)**, 5955–5964 (2007).

[49] R. INGUANTA, S. PIAZZA, & C. SUNSERI. Novel procedure for the template synthesis of metal nanostructures. *Electrochemistry Communications* **10 (4)**, 506–509 (2008).

[50] K. KRISHNAMOORTHY & C. G. ZOSKI. Fabrication of 3d gold nanoelectrode ensembles by chemical etching. *Analytical Chemistry* **77 (15)**, 5068–5071 (2005).

[51] H. C. CHANG & G. YOSSIFON. Understanding electrokinetics at the nanoscale: A perspective. *Biomicrofluidics* **3 (1)** (2009).

[52] R. B. SCHOCH, J. HAN, & P. RENAUD. Transport phenomena in nanofluidics. *Reviews of Modern Physics* **80 (3)**, 839–883 (2008).

[53] D. BRATKO, C. D. DAUB, K. LEUNG, & A. LUZAR. Effect of field direction on electrowetting in a nanopore. *Journal of the American Chem ical Society* **129 (9)**, 2504–2510 (2007).

[54] J. K. HOLT, H. G. PARK, Y. M. WANG, M. STADERMANN, A. B. ARTYUKHIN, C. P. GRIGOROPOULOS, A. NOY, & O. BAKAJIN. Fast mass transport through sub-2-nanometer carbon nanotubes. *Science* **312 (5776)**, 1034–1037 (2006).

[55] R. CHOI, J. YANG, J. CHOI, E. K. LIM, E. KIM, J. S. SUH, Y. M. HUH, & S. HAAM. Thiolated dextran-coated gold nanorods for photothermal ablation of inflammatory macrophages. *Langmuir* **26 (22)**, 17520–17527 (2010).

[56] W. CHOI, Z. W. ULISSI, S. F. E. SHIMIZU, D. O. BELLISARIO, M. D. ELLISON, & M. S. STRANO. Diameter-dependent ion transport through the interior of isolated single-walled carbon nanotubes. *Nature Communications* **4** (2013).

[57] A. GRATTONI, D. FINE, E. ZABRE, A. ZIEMYS, J. GILL, Y. MACKEYEV, M. A. CHENEY, D. C. DANILA, S. HOSALI, L. J. WILSON, F. HUSSAIN, & M. FERRARI. Gated and near-surface diffusion of charged fullerenes in nanochannels. *ACS Nano* **5 (12)**, 9382–9391 (2011).

[58] F. FORNASIERO, H. G. PARK, J. K. HOLT, M. STADERMANN, C. P. GRIGOROPOULOS, A. NOY, & O. BAKAJIN. Ion exclusion by sub-2-nm carbon nanotube pores. *Proceedings of the National Academy of Sciences* **105 (45)**, 17250–17255 (2008).

[59] M. NISHIZAWA, V. P. MENON, & C. R. MARTIN. Metal nanotubule membranes with electrochemically switchable ion-transport selectivity. *Science* **268 (5211)**, 700–702 (1995).

[60] C. R. MARTIN, M. NISHIZAWA, K. JIRAGE, & M. KANG. Investigations of the transport properties of gold nanotubule membranes. *Journal of Physical Chemistry B* **105 (10)**, 1925–1934 (2001).

[61] P. ABGRALL & N. T. NGUYEN. *Nanofluidics*. Artech House, Boston (2009).

[62] Y. C. WANG, A. L. STEVENS, & J. Y. HAN. Million-fold preconcentration of proteins and peptides by nanofluidic filter. *Analytical Chemistry* **77 (14)**, 4293–4299 (2005).

[63] Y. ZHANG & A. T. TIMPERMAN. Integration of nanocapillary arrays into microfluidic devices for use as analyte concentrators. *Analyst* **128 (6)**, 537–542 (2003).

[64] D. HLUSHKOU, R. DHOPESHWARKAR, R. M. CROOKS, & U. TALLAREK. The influence of membrane ion-permselectivity on electrokinetic concentration enrichment in membrane-based preconcentration units. *Lab on a Chip* **8 (7)**, 1153–1162 (2008).

[65] R. DHOPESHWARKAR, R. M. CROOKS, D. HLUSHKOU, & U. TALLAREK. Transient effects on microchannel electrokinetic filtering with an ion-permselective membrane. *Analytical Chemistry* **80 (4)**, 1039–1048 (2008).

[66] S. J. KIM & J. Y. HAN. Self-sealed vertical polymeric nanoporous-junctions for high-throughput nanofluidic applications. *Analytical Chemistry* **80 (9)**, 3507–3511 (2008).

[67] T. C. KUO, D. M. CANNON, M. A. SHANNON, P. W. BOHN, & J. V. SWEEDLER. Hybrid three-dimensional nanofluidic/microfluidic devices using molecular gates. *Sensors and Actuators a-Physical* **102 (3)**, 223–233 (2003).

[68] T. C. KUO, D. M. CANNON, Y. N. CHEN, J. J. TULOCK, M. A. SHANNON, J. V. SWEEDLER, & P. W. BOHN. Gateable nanofluidic interconnects for multilayered microfluidic separation systems. *Analytical Chemistry* **75 (8)**, 1861–1867 (2003).

[69] J. P. GUERRETTE & B. ZHANG. Scan-rate-dependent current rectification of cone-shaped silica nanopores in quartz nanopipettes. *Journal of the American Chemical Society* **132 (48)**, 17088–17091 (2010).

[70] Z. SIWY & A. FULINSKI. Fabrication of a synthetic nanopore ion pump. *Physical Review Letters* **89 (19)** (2002).

[71] S. A. GAJAR & M. W. GEIS. An ionic liquid-channel field-effect transistor. *Journal of the Electrochemical Society* **139 (10)**, 2833–2840 (1992).

[72] R. KARNIK, R. FAN, M. YUE, D. Y. LI, P. D. YANG, & A. MAJUMDAR. Electrostatic control of ions and molecules in nanofluidic transistors. *Nano Letters* **5 (5)**, 943–948 (2005).

[73] R. FAN, M. YUE, R. KARNIK, A. MAJUMDAR, & P. D. YANG. Polarity switching and transient responses in single nanotube nanofluidic transistors. *Physical Review Letters* **95 (8)** (2005).

[74] K. VENTA, M. WANUNU, & M. DRNDIC. Electrically controlled nanoparticle synthesis inside nanopores. *Nano Letters* **13 (2)**, 423–429 (2013).

[75] E. D. GERMAN & M. SHEINTUCH. Kinetics of catalytic oh dissociation on metal surfaces. *Journal of Physical Chemistry C* **116 (9)**, 5700–5709 (2012).

[76] X. C. XUAN, S. RAGHIBIZADEH, & D. Q. LI. Wall effects on electrophoretic motion of spherical polystyrene particles in a rectangular poly (dimethylsiloxane) microchannel. *Journal of Colloid and Interface Science* **296 (2)**, 743–748 (2006).

[77] M. WIRTZ, S. F. YU, & C. R. MARTIN. Template synthesized gold nanotube membranes for chemical separations and sensing. *Analyst* **127 (7)**, 871–879 (2002).

[78] D. A. HOLDEN, G. HENDRICKSON, L. A. LYON, & H. S. WHITE. Resistive pulse analysis of microgel deformation during nanopore translocation. *Journal of Physical Chemistry C* **115 (7)**, 2999–3004 (2011).

[79] D. A. HOLDEN, G. R. HENDRICKSON, W. J. LAN, L. A. LYON, & H. S. WHITE. Electrical signature of the deformation and dehydration of microgels during translocation through nanopores. *Soft Matter* **7 (18)**, 8035–8040 (2011).

[80] G. R. WILLMOTT & B. E. T. PARRY. Resistive pulse asymmetry for nanospheres passing through tunable submicron pores. *Journal of Applied Physics* **109 (9)** (2011).

[81] G. S. ROBERTS, D. KOZAK, W. ANDERSON, M. F. BROOM, R. VOGEL, & M. TRAU. Tunable nano/micropores for particle detection and discrimination: Scanning ion occlusion spectroscopy. *Small* **6 (23)**, 2653–2658 (2010).

[82] T. S. MAHADEVAN, M. MILOSEVIC, M. KOJIC, F. HUSSAIN, N. KOJIC, R. SERDA, M. FERRARI, & A. ZIEMYS. Diffusion transport of nanoparticles at nanochannel boundaries. *Journal of Nanoparticle Research* **15 (3)** (2013).

[83] T. C. KUO, L. A. SLOAN, J. V. SWEEDLER, & P. W. BOHN. Manipulating molecular transport through nanoporous membranes by control of electrokinetic flow: Effect of surface charge density and debye length. *Langmuir* **17 (20)**, 6298–6303 (2001).

[84] T. D. LI, J. P. GAO, R. SZOSZKIEWICZ, U. LANDMAN, & E. RIEDO. Structured and viscous water in subnanometer gaps. *Physical Review B* **75 (11)** (2007).

[85] R. DUTZLER, Y. F. WANG, P. J. RIZKALLAH, J. P. ROSENBUSCH, & T. SCHIRMER. Crystal structures of various maltooligosaccharides bound to maltoporin reveal a specific sugar translocation pathway. *Structure* **4 (2)**, 127–134 (1996).

[86] W. SPARREBOOM, A. VAN DEN BERG, & J. C. T. EIJKEL. Principles and applications of nanofluidic transport. *Nature Nanotechnology* **4 (11)**, 713–720 (2009).

[87] C. I. BOUZIGUES, P. TABELING, & L. BOCQUET. Nanofluidics in the debye layer at hydrophilic and hydrophobic surfaces. *Physical Review Letters* **101 (11)** (2008).

[88] A. J. BARD & L. R. FAULKNER. *Electrochemical Methods: Fundamentals and Applications*. John Wiley & Sons, Inc., New York, 2nd edition (2001).

[89] K. S. BIRDI (Editor). *Introduction to Electrical Interfacial Phenomena*, book Appendix, 144–146. CRC Press, Boca Raton (2010).

[90] N. T. NGUYEN & S. T. WERELEY. *Fundamentals and Applications of Microfluidics*. Artech House, Inc., Boston, second edition edition (2006).

[91] C. AMATORE & E. MAISONHAUTE. When voltammetry reaches nanoseconds. *Analytical Chemistry* **77 (15)**, 303A–311A (2005).

[92] S. M. OJA, M. WOOD, & B. ZHANG. Nanoscale electrochemistry. *Analytical Chemistry* **85 (2)**, 473–486 (2013).

[93] X. S. ZHOU, L. LIU, P. FORTGANG, A. S. LEFEVRE, A. SERRA-MUNS, N. RAOUAFI, C. AMATORE, B. W. MAO, E. MAISONHAUTE, & B. SCHOLLHORN. Do molecular conductances correlate with electrochemical rate constants? experimental insights. *Journal of the American Chemical Society* **133 (19)**, 7509–7516 (2011).

[94] J. T. COX & B. ZHANG. Nanoelectrodes: Recent advances and new directions. *Annual Review of Analytical Chemistry, Vol 5* **5**, 253–272 (2012).

[95] K. L. ADAM, B. K. JENA, S. J. PERCIVAL, & B. ZHANG. Highly sensitive detection of exocytotic dopamine release using a gold-nanoparticle-network microelectrodes. *Analytical Chemistry* **83**, 920–927 (2010).

[96] R. R. HENRIQUEZ, T. ITO, L. SUN, & R. M. CROOKS. The resurgence of coulter counting for analyzing nanoscale objects. *Analyst* **129 (6)**, 478–482 (2004).

[97] H. BAYLEY & C. R. MARTIN. Resistive-pulse sensing - from microbes to molecules. *Chemical Reviews* **100 (7)**, 2575–2594 (2000).

[98] C. C. HARRELL, Y. CHOI, L. P. HORNE, L. A. BAKER, Z. S. SIWY, & C. R. MARTIN. Resistive-pulse dna detection with a conical nanopore sensor. *Langmuir* **22 (25)**, 10837–10843 (2006).

[99] T. M. SQUIRES & S. R. QUAKE. Microfluidics: Fluid physics at the nanoliter scale. *Reviews of Modern Physics* **77 (3)**, 977–1026 (2005).

[100] D. E. ANGELESCU. *Highly Integrated Microfluidics Design*. Artech House, Boston (2011).

[101] K. B. OLDHAM, J. C. MYLAND, & A. M. BOND. *Electrochemical Science and Technology: Fundamentals and Applications*. John Wiley & Sons, Ltd., Chichester (2012).

[102] A. M. STRIEGEL & A. K. BREWER. Hydrodynamic chromatography. *Annual Review of Analytical Chemistry, Vol 5* **5**, 15–34 (2012).

[103] R. TIJSSEN, J. BOS, & M. E. VANKREVELD. Hydrodynamic chromatography of macromolecules in open microcapillary tubes. *Analytical Chemistry* **58 (14)**, 3036–3044 (1986).

[104] A. A. KOROLEV, E. N. VIKTOROVA, V. A. OREKHOV, & A. A. KURGANOV. Unusually high efficiency of the separation of polymers by hydrodynamic chromatography on hollow capillary columns. *Russian Journal of Physical Chemistry A* **86 (7)**, 1161–1164 (2012).

[105] S. GHOSAL. Fluid mechanics of electroosmotic flow and its effect on band broadening in capillary electrophoresis. *Electrophoresis* **25 (2)**, 214–228 (2004).

[106] D. LI. Electro-viscous effects on pressure-driven liquid flow in microchannels. *Colloids and Surfaces A: Physicochemical and Engineering Aspects* **195 (1)**, 35–57 (2001).

[107] A. T. CARLSEN, O. K. ZAHID, J. RUZICKA, E. W. TAYLOR, & A. R. HALL. Interpreting the conductance blockades of dna translocations through solid-state nanopores. *ACS nano* (2014).

[108] R. PETHIG. Review article-dielectrophoresis: Status of the theory, technology, and applications. *Biomicrofluidics* **4 (2)** (2010).

[109] Y. AI & S. QIAN. Electrokinetic particle translocation through a nanopore. *Physical Chemistry Chemical Physics* **13 (9)**, 4060–4071 (2011).

[110] S. E. FOSDICK, K. N. KNUST, K. SCIDA, & R. M. CROOKS. Bipolar electrochemistry. *Angewandte Chemie-International Edition* **52 (40)**, 10438–10456 (2013).

[111] G. LOGET, D. ZIGAH, L. BOUFFIER, N. SOJIC, & A. KUHN. Bipolar electrochemistry: From materials science to motion and beyond. *Accounts of Chemical Research* **46 (11)**, 2513–2523 (2013).

[112] G. LOGET & A. KUHN. Shaping and exploring the micro- and nanoworld using bipolar electrochemistry. *Analytical and Bioanalytical Chemistry* **400 (6)**, 1691–1704 (2011).

[113] J. BACKHURST, E. GOODRIDGE, R. PLIMLEY, & M. FLEISCHMANN. Some aspects of a fluidized zinc/oxygen electrode system. *Nature* (1969).

[114] M. FLEISCHMANN & J. OLDFIELD. Fluidised bed electrodes: Part i. polarisation predicted by simplified models. *Journal of Electroanalytical Chemistry and Interfacial Electrochemistry* **29 (2)**, 211–230 (1971).

[115] F. GOODRIDGE, C. KING, & A. WRIGHT. The behaviour of bipolar packed-bed electrodes. *Electrochimica Acta* **22 (4)**, 347–352 (1977).

[116] R. PLIMLEY & A. WRIGHT. A bipolar mechanism for charge transferin a fluidised bed electrode. *Chemical engineering science* **39 (3)**, 395–405 (1984).

[117] E. SMOTKIN, A. J. BARD, A. CAMPION, M. A. FOX, T. MALLOUK, S. E. WEBBER, & J. WHITE. Bipolar titanium dioxide/platinum semiconductor photoelectrodes and multielectrode arrays for unassisted photolytic water splitting. *The Journal of Physical Chemistry* **90 (19)**, 4604–4607 (1986).

[118] K. WIESENER, D. OHMS, G. BENCZÚR-ÜRMÖSSY, M. BERTHOLD, & F. HASCHKA. High power metal hydride bipolar battery. *Journal of Power Sources* **84 (2)**, 248–258 (1999).

[119] B. C. STEELE & A. HEINZEL. Materials for fuel-cell technologies. *Nature* **414 (6861)**, 345–352 (2001).

[120] A. HERMANN, T. CHAUDHURI, & P. SPAGNOL. Bipolar plates for pem fuel cells: A review. *International Journal of Hydrogen Energy* **30 (12)**, 1297–1302 (2005).

[121] K.-F. CHOW, F. MAVRÉ, J. A. CROOKS, B.-Y. CHANG, & R. M. CROOKS. A large-scale, wireless electrochemical bipolar electrode microarray. *Journal of the American Chemical Society* **131 (24)**, 8364–8365 (2009).

[122] J.-C. BRADLEY, Z. MA, & S. G. STEPHENS. Electric field directed construction of diodes using free-standing three-dimensional component. *Advanced Materials* **11 (5)**, 374–378 (1999).

[123] J.-C. BRADLEY, J. CRAWFORD, K. ERNAZAROVA, M. MCGEE, & S. G. STEPHENS. Wire formation on circuit boards using spatially coupled bipolar electrochemistry. *Advanced Materials* **9 (15)**, 1168–1171 (1997).

[124] G. LOGET, J. ROCHE, E. GIANESSI, L. BOUFFIER, & A. KUHN. Indirect bipolar electrodeposition. *Journal of the American Chemical Society* **134 (49)**, 20033–20036 (2012).

[125] Z. FATTAH, P. GARRIGUE, V. LAPEYRE, A. KUHN, & L. BOUFFIER. Controlled orientation of asymmetric copper deposits on carbon microobjects by bipolar electrochemistry. *The Journal of Physical Chemistry C* **116 (41)**, 22021–22027 (2012).

[126] C. WARAKULWIT, T. NGUYEN, J. MAJIMEL, M.-H. DELVILLE, V. LAPEYRE, P. GARRIGUE, V. RAVAINE, J. LIMTRAKUL, & A. KUHN. Dissymmetric carbon nanotubes by bipolar electrochemistry. *Nano Letters* **8 (2)**, 500–504 (2008).

[127] M. SENTIC, G. LOGET, D. MANOJLOVIC, A. KUHN, & N. SOJIC. Light-emitting electrochemical swimmers. *Angewandte Chemie International Edition* **51 (45)**, 11284–11288 (2012).

[128] W. GAO, S. SATTAYASAMITSATHIT, K. M. MANESH, D. WEIHS, & J. WANG. Magnetically powered flexible metal nanowire motors. *Journal of the American Chemical Society* **132 (41)**, 14403–14405 (2010).

[129] D. R. LAWS, D. HLUSHKOU, R. K. PERDUE, U. TALLAREK, & R. M. CROOKS. Bipolar electrode focusing: Simultaneous concentration enrichment and separation in a microfluidic channel containing a bipolar electrode. *Analytical chemistry* **81 (21)**, 8923–8929 (2009).

[130] M.-S. WU, G.-S. QIAN, J.-J. XU, & H.-Y. CHEN. Sensitive electrochemiluminescence detection of c-myc mrna in breast cancer cells on a wireless bipolar electrode. *Analytical chemistry* **84 (12)**, 5407–5414 (2012).

[131] K.-F. CHOW, F. MAVRÉ, & R. M. CROOKS. Wireless electrochemical dna microarray sensor. *Journal of the American Chemical Society* **130 (24)**, 7544–7545 (2008).

[132] X. LIN, L. ZHENG, G. GAO, Y. CHI, & G. CHEN. Electrochemiluminescence imaging-based high-throughput screening platform for electrocatalysts used in fuel cells. *Analytical chemistry* **84 (18)**, 7700–7707 (2012).

[133] S. E. FOSDICK & R. M. CROOKS. Bipolar electrodes for rapid screening of electrocatalysts. *Journal of the American Chemical Society* **134 (2)**, 863–866 (2012).

[134] J. P. GUERRETTE, S. J. PERCIVAL, & B. ZHANG. Fluorescence coupling for direct imaging of electrocatalytic heterogeneity. *Journal of the American Chemical Society* **135 (2)**, 855–861 (2012).

[135] F. MAVRE, R. K. ANAND, D. R. LAWS, K. F. CHOW, B. Y. CHANG, J. A. CROOKS, & R. M. CROOKS. Bipolar electrodes: A useful tool for concentration, separation, and detection of analytes in microelectrochemical systems. *Analytical Chemistry* **82 (21)**, 8766–8774 (2010).

[136] J. T. COX, J. P. GUERRETTE, & B. ZHANG. Steady-state voltammetry of a microelectrode in a closed bipolar cell. *Analytical Chemistry* **84 (20)**, 8797–8804 (2012).

[137] J. P. GUERRETTE, S. M. OJA, & B. ZHANG. Coupled electrochemical reactions at bipolar microelectrodes and nanoelectrodes. *Analytical Chemistry* **84 (3)**, 1609–1616 (2012).

[138] K. R. WEHMEYER, M. R. DEAKIN, & R. M. WIGHTMAN. Electroanalytical properties of band electrodes of submicrometer width. *Analytical Chemistry* **57 (9)**, 1913–1916 (1985).

[139] M. MAEDA, H. S. WHITE, & D. J. MCCLURE. Electrochemical behavior and surface structure of pt thin-film electrodes deposited on molecularly smooth mica. *Journal of Electroanalytical Chemistry* **200 (1-2)**, 383–387 (1986).

[140] C. G. ZOSKI. Ultramicroelectrodes: Design, fabrication, and characterization. *Electroanalysis* **14 (15-16)**, 1041–1051 (2002).

[141] J. P. GUERRETTE, S. J. PERCIVAL, & B. ZHANG. Voltammetric behavior of gold nanotrench electrodes. *Langmuir* **27 (19)**, 12218–12225 (2011).

[142] S. L. CASTON & R. L. MCCARLEY. Characteristics of nanoscopic au band electrodes. *Journal of Electroanalytical Chemistry* **529 (2)**, 124–134 (2002).

[143] B. ZHANG, Y. H. ZHANG, & H. S. WHITE. The nanopore electrode. *Analytical Chemistry* **76 (21)**, 6229–6238 (2004).

[144] B. ZHANG, J. GALUSHA, P. G. SHIOZAWA, G. L. WANG, A. J. BERGREN, R. M. JONES, R. J. WHITE, E. N. ERVIN, C. C. CAULEY, & H. S. WHITE. Bench-top method for fabricating glass-sealed nanodisk electrodes, glass nanopore electrodes, and glass nanopore membranes of controlled size. *Analytical Chemistry* **79 (13)**, 4778–4787 (2007).

[145] P. SUN & M. V. MIRKIN. Scanning electrochemical microscopy with slightly recessed nanotips. *Analytical Chemistry* **79 (15)**, 5809–5816 (2007).

[146] Y. T. KIM, D. M. SCARNULIS, & A. G. EWING. Carbon-ring electrodes with 1-mu-m tip diameter. *Analytical Chemistry* **58 (8)**, 1782–1786 (1986).

[147] G. ZHAO, D. M. GIOLANDO, & J. R. KIRCHHOFF. Carbon ring disk ultramicroelectrodes. *Analytical Chemistry* **67 (8)**, 1491–1495 (1995).

[148] Y. ZHANG, W. CHU, A. D. FOROUSHANI, H. WANG, D. LI, J. LIU, C. J. BARROW, X. WANG, & W. YANG. New gold nanostructures for sensor applications: A review. *Materials* **7 (7)**, 5169–5201 (2014). URL `http://www.mdpi.com/1996-1944/7/7/5169`.

[149] D. R. MACFARLANE & D. K. Y. WONG. Thin-ring ultra-microelectrodes. *Journal of Electroanalytical Chemistry* **185 (1)**, 197–202 (1985).

[150] P. LILJEROTH, C. JOHANS, C. J. SLEVIN, B. M. QUINN, & K. KONTTURI. Micro ring-disk electrode probes for scanning electrochemical microscopy. *Electrochemistry Communications* **4 (1)**, 67–71 (2002).

[151] J. GOLAS, Z. GALUS, & J. OSTERYOUNG. Iridium-based small mercury-electrodes. *Analytical Chemistry* **59 (3)**, 389–392 (1987).

[152] Y. SELZER & D. MANDLER. Scanning electrochemical microscopy. theory of the feedback mode for hemispherical ultramicroelectrodes: Steady-state and transient behavior. *Analytical Chemistry* **72 (11)**, 2383–2390 (2000).

[153] W. H. HUANG, D. W. PANG, H. TONG, Z. L. WANG, & J. K. CHENG. A method for the fabrication of low-noise carbon fiber nanoelectrodes. *Analytical Chemistry* **73 (5)**, 1048–1052 (2001).

[154] P. S. CAHILL, Q. D. WALKER, J. M. FINNEGAN, G. E. MICKELSON, E. R. TRAVIS, & R. M. WIGHTMAN. Microelectrodes for the measurement of catecholamines in biological systems. *Analytical Chemistry* **68 (18)**, 3180–3186 (1996).

[155] D. H. CHEN & C. J. CHEN. Formation and characterization of au-ag bimetallic nanoparticles in water-in-oil microemulsions. *Journal of Materials Chemistry* **12 (5)**, 1557–1562 (2002).

[156] P. SUN, Z. Q. ZHANG, J. D. GUO, & Y. H. SHAO. Fabrication of nanometer-sized electrodes and tips for scanning electrochemical microscopy. *Analytical Chemistry* **73 (21)**, 5346–5351 (2001).

[157] B. B. KATEMANN & T. SCHUHMANN. Fabrication and characterization of needle-type pt-disk nanoelectrodes. *Electroanalysis* **14 (1)**, 22–28 (2002).

[158] Y. LI, D. BERGMAN, & B. ZHANG. Preparation and electrochemical response of 1-3 nm pt disk electrodes. *Analytical Chemistry* **81 (13)**, 5496–5502 (2009).

[159] J. VELMURUGAN, P. SUN, & M. V. MIRKIN. Scanning electrochemical microscopy with gold nanotips: The effect of electrode material on electron transfer rates. *Journal of Physical Chemistry C* **113 (1)**, 459–464 (2009).

[160] Y. H. SHAO, M. V. MIRKIN, G. FISH, S. KOKOTOV, D. PALANKER, & A. LEWIS. Nanometer-sized electrochemical sensors. *Analytical Chemistry* **69 (8)**, 1627–1634 (1997).

[161] L. A. NAGAHARA, T. THUNDAT, & S. M. LINDSAY. Preparation and characterization of stm tips for electrochemical studies. *Review of Scientific Instruments* **60 (10)**, 3128–3130 (1989).

[162] A. WAHL, S. BARRY, K. DAWSON, J. MACHALE, A. J. QUINN, & A. O'RIORDAN. Electroanalysis at ultramicro and nanoscale electrodes: A comparative study. *Journal of the Electrochemical Society* **161 (2)**, B3055–B3060 (2014).

[163] P. ELSAMADISI, Y. WANG, J. VELMURUGAN, & M. V. MIRKIN. Polished nanopipets: New probes for high-resolution scanning electrochemical microscopy. *Analytical chemistry* **83 (3)**, 671–673 (2010).

[164] P. SUN, F. LI, C. YANG, T. SUN, I. KADY, B. HUNT, & J. ZHUANG. Formation of a single gold nanoparticle on a nanometer-sized electrode and its electrochemical behaviors. *Journal of Physical Chemistry C* **117 (12)**, 6120–6125 (2013).

[165] X. ZHU, Y. QIAO, X. ZHANG, S. ZHANG, X. YIN, J. GU, Y. CHEN, Z. ZHU, M. LI, & Y. SHAO. Fabrication of metal nanoelectrodes by interfacial reactions. *Analytical Chemistry* **86 (14)**, 7001–7008 (2014).

[166] B. LIU, J. P. ROLLAND, J. M. DESIMONE, & A. J. BARD. Fabrication of ultramicroelectrodes using a "teflon-like" coating material. *Analytical Chemistry* **77 (9)**, 3013–3017 (2005).

[167] A. SCHULTE & R. H. CHOW. A simple method for insulating carbon fiber microelectrodes using anodic electrophoretic deposition of paint. *Analytical Chemistry* **68 (17)**, 3054–3058 (1996).

[168] C. J. SLEVIN, N. J. GRAY, J. V. MACPHERSON, M. A. WEBB, & P. R. UNWIN. Fabrication and characterisation of nanometre-sized platinum electrodes for voltammetric analysis and imaging. *Electrochemistry Communications* **1 (7)**, 282–288 (1999).

[169] D. A. ZHANG, E. RAND, M. MARSH, R. J. ANDREWS, K. H. LEE, M. MEYYAPPAN, & J. E. KOEHNE. Carbon nanofiber electrode for neurochemical monitoring. *Molecular Neurobiology* **48 (2)**, 380–385 (2013).

[170] S. Viswanathan, C. Rani, & C. Delerue-Matos. Ultrasensitive detection of ovarian cancer marker using immunoliposomes and gold nanoelectrodes. *Analytica Chimica Acta* **726**, 79–84 (2012).

[171] Y. Y. Liu, Y. C. Zhu, Y. Zeng, & F. F. Xu. An effective amperometric biosensor based on gold nanoelectrode arrays. *Nanoscale Research Letters* **4 (3)**, 210–215 (2009).

[172] K. Dawson, J. Strutwolf, K. P. Rodgers, G. Herzog, D. W. M. Arrigan, A. J. Quinn, & A. O'Riordan. Single nanoskived nanowires for electrochemical applications. *Analytical Chemistry* **83 (14)**, 5535–5540 (2011).

[173] J. B. Sambur & P. Chen. Approaches to single-nanoparticle catalysis. *Annual Review of Physical Chemistry, Vol 65* **65**, 395–422 (2014).

[174] M. A. Rahman, J. I. Son, M.-S. Won, & Y.-B. Shim. Gold nanoparticles doped conducting polymer nanorod electrodes: ferrocene catalyzed aptamer-based thrombin immunosensor. *Analytical chemistry* **81 (16)**, 6604–6611 (2009).

[175] B. K. Jena, S. J. Percival, & B. Zhang. Au disk nanoelectrode by electrochemical deposition in a nanopore. *Analytical Chemistry* **82 (15)**, 6737–6743 (2010).

[176] Q. Xu, R. M. Rioux, M. D. Dickey, & G. M. Whitesides. Nanoskiving: A new method to produce arrays of nanostructures. *Accounts of Chemical Research* **41 (12)**, 1566–1577 (2008).

[177] E. J. Menke, M. A. Thompson, C. Xiang, L. C. Yang, & R. M. Penner. Lithographically patterned nanowire electrodeposition. *Nature Materials* **5 (11)**, 914–919 (2006).

[178] C. Xiang, S.-C. Kung, D. K. Taggart, F. Yang, M. A. Thompson, A. G. Gueell, Y. Yang, & R. M. Penner. Lithographically patterned nanowire electrodeposition: A method for patterning electrically continuous metal nanowires on dielectrics. *ACS Nano* **2 (9)**, 1939–1949 (2008).

[179] W. Lu & C. M. Lieber. Nanoelectronics from the bottom up. *Nature Materials* **6 (11)**, 841–850 (2007).

[180] M. Kwiat, S. Cohen, A. Pevzner, & F. Patolsky. Large-scale ordered 1d-nanomaterials arrays: Assembly or not? *Nano Today* **8 (6)**, 677–694 (2013).

[181] N. I. Kovtyukhova & T. E. Mallouk. Nanowires as building blocks for self-assembling logic and memory circuits. *Chemistry-a European Journal* **8 (19)**, 4355–4363 (2002).

[182] M. SCHVARTZMAN, D. TSIVION, D. MAHALU, O. RASLIN, & E. JOSELEVICH. Self-integration of nanowires into circuits via guided growth. *Proceedings of the National Academy of Sciences of the United States of America* **110 (38)**, 15195–15200 (2013).

[183] T. J. MORROW, M. W. LI, J. KIM, T. S. MAYER, & C. D. KEATING. Programmed assembly of dna-coated nanowire devices. *Science* **323 (5912)**, 352–352 (2009).

[184] S. LAL, J. H. HAFNER, N. J. HALAS, S. LINK, & P. NORDLANDER. Noble metal nanowires: From plasmon waveguides to passive and active devices. *Accounts of Chemical Research* **45 (11)**, 1887–1895 (2012).

[185] X. GUO, Y. YING, & L. TONG. Photonic nanowires: From subwavelength waveguides to optical sensors. *Accounts of Chemical Research* **47 (2)**, 656–666 (2014).

[186] H. WEI & H. XU. Nanowire-based plasmonic waveguides and devices for integrated nanophotonic circuits. *Nanophotonics* **1 (2)**, 155–169 (2012).

[187] X. HOU, X. ZHANG, S. CHEN, Y. FANG, N. LI, X. ZHAI, & Y. LIU. Size-controlled synthesis of au nanoparticles and nanowires and their application as sers substrates. *Colloids and Surfaces a-Physicochemical and Engineering Aspects* **384 (1-3)**, 345–351 (2011).

[188] R. W. MURRAY. Nanoelectrochemistry: Metal nanoparticles, nanoelectrodes, and nanopores. *Chemical Reviews* **108 (7)**, 2688–2720 (2008).

[189] N. LI, P. ZHAO, & D. ASTRUC. Anisotropic gold nanopa rticles: Synthe sis, proper ties, applications, and toxicity. *Ange wandte Chemie-International Edition* **53 (7)**, 1756–1789 (2014).

[190] L. VIGDERMAN, B. P. KHANAL, & E. R. ZUBAREV. Functional gold nanorods: Synthesis, self-assembly, and sensing applications. *Advanced Materials* **24 (36)**, 4811–4841 (2012).

[191] F. KIM, K. SOHN, J. WU, & J. HUANG. Chemical synthesis of gold nanowires in acidic solutions. *Journal of the American Chemical Society* **130 (44)**, 14442–+ (2008).

[192] S. J. HURST, E. K. PAYNE, L. D. QIN, & C. A. MIRKIN. Multisegmented one-dimensional nanorods prepared by hard-template synthetic methods. *Angewandte Chemie-International Edition* **45 (17)**, 2672–2692 (2006).

[193] M. WIRTZ & C. R. MARTIN. Template-fabricated gold nanowires and nanotubes. *Advanced Materials* **15 (5)**, 455–458 (2003).

[194] Y. PIAO & H. KIM. Fabrication of nanostructured materials using porous alumina template and their applications for sensing and electrocatalysis. *Journal of Nanoscience and Nanotechnology* **9 (4)**, 2215–2233 (2009).

[195] R. M. PENNER & C. R. MARTIN. Preparation and electrochemical characterization of ultramicroelectrode ensembles. *Analytical Chemistry* **59 (21)**, 2625–2630 (1987).

[196] J. LIU, J. L. DUAN, E. TOIMIL-MOLARES, S. KARIM, T. W. CORNELIUS, D. DOBREV, H. J. YAO, Y. M. SUN, M. D. HOU, D. MO, Z. G. WANG, & R. NEUMANN. Electrochemical fabrication of single-crystalline and polycrystalline au nanowires: the influence of deposition parameters. *Nanotechnology* **17 (8)**, 1922–1926 (2006).

[197] Z. WU, Y. ZHANG, & K. DU. A simple and efficient combined ac-dc electrodeposition method for fabrication of highly ordered au nanowires in aao template. *Applied Surface Science* **265**, 149–156 (2013).

[198] C. X. KAN, W. P. CAI, Z. S. LI, G. H. FU, & L. D. ZHANG. Reduction effect of pore wall and formation of au nanowires inside monolithic mesoporous silica. *Chemical Physics Letters* **382 (3-4)**, 318–324 (2003).

[199] L. T. QU & L. M. DAI. Substrate-enhanced electroless deposition of metal nanoparticles on carbon nanotubes. *Journal of the American Chemical Society* **127 (31)**, 10806–10807 (2005).

[200] Q. XU, G. MENG, X. WU, Q. WEI, M. KONG, X. ZHU, & Z. CHU. A generic approach to desired metallic nanowires inside native porous alumina template via redox reaction. *Chemistry of Materials* **21 (12)**, 2397–2402 (2009).

[201] J.-C. BRADLEY, H.-M. CHEN, J. CRAWFORD, J. ECKERT, K. ERNAZAROVA, T. KURZEJA, M. LIN, M. MCGEE, W. NADLER, & S. G. STEPHENS. Creating electrical contacts between metal particles using directed electrochemical growth. *Nature* **389 (6648)**, 268–271 (1997).

[202] J.-C. BRADLEY, S. BABU, B. CARROLL, & A. MITTAL. A study of spatially coupled bipolar electrochemistry on the sub-micrometer scale: colloidal particles on surfaces and cylinders in nuclear-track etched membranes. *Journal of Electroanalytical Chemistry* **522 (1)**, 75–85 (2002).

[203] G. LOGET, J. ROCHE, & A. KUHN. True bulk synthesis of janus objects by bipolar electrochemistry. *Advanced Materials* **24 (37)**, 5111–5116 (2012).

[204] H. ZHOU, W.-P. ZHOU, R. R. ADZIC, & S. S. WONG. Enhanced electrocatalytic performance of one-dimensional metal nanowires and arrays generated via an ambient, surfactantless synthesis. *Journal of Physical Chemistry C* **113 (14)**, 5460–5466 (2009).

[205] C. KOENIGSMANN, A. C. SANTULLI, E. SUTTER, & S. S. WONG. Ambient surfactant less synthesis, growth mechanism, and size-dependent electrocatalytic behavior of high-quality, single crystalline palladium nanowires. *ACS Nano* **5 (9)** (2011).

[206] C. KOENIGSMANN, Z. TAN, H. PENG, E. SUTTER, J. JACOBSKIND, & S. S. WONG. Multifunctional nanochemistry: Ambient, electroless, template-based synthesis and characterization of segmented bimetallic pd/au and pd/pt nanowires as high-performance electrocatalysts and nanomotors. *Israel Journal of Chemistry* **52 (11-12)**, 1090–1103 (2012).

[207] R. SHARABANI, S. REUVENI, G. NOY, E. SHAPIRA, S. SADEH, & Y. SELZER. Fabrication of very high aspect ratio metal nanowires by a self-propulsion mechanism. *Nano Letters* **8 (4)**, 1169–1173 (2008).

[208] B. ZHANG, M. WOOD, & H. LEE. A silica nanochannel and its applications in sensing and molecular transport. *Analytical Chemistry* **81 (13)**, 5541–5548 (2009).

[209] S. E. SALAMIFAR & R. Y. LAI. Fabrication of electrochemical dna sensors on gold-modified recessed platinum nanoelectrodes. *Analytical chemistry* **86 (6)**, 2849–2852 (2014).

[210] K. L. ADAMS, B. K. JENA, S. J. PERCIVAL, & B. ZHANG. Highly sensitive detection of exocytotic dopamine release using a gold-nanoparticle-network microelectrode. *Analytical Chemistry* **83 (3)**, 920–927 (2011).

[211] J. H. PARK, S. N. THORGAARD, B. ZHANG, & A. J. BARD. Single particle detection by area amplification: single wall carbon nanotube attachment to a nanoelectrode. *Journal of the American Chemical Society* **135 (14)**, 5258–5261 (2013).

[212] K. DAWSON, A. WAHL, S. BARRY, C. BARRETT, N. SASSIAT, A. J. QUINN, & A. ORIORDAN. Fully integrated on-chip nano-electrochemical devices for electroanalytical applications. *Electrochimica Acta* **115**, 239–246 (2014).

[213] A. CHEN, M.-J. TSAO, J.-F. CHUANG, & C.-H. LIN. Electrochemical determination of verapamil with a microchip embedded with gold nanoelectrode ensemble electrodes. *Electrochimica Acta* **89**, 700–707 (2013).

[214] S. BARTH, F. HERNANDEZ-RAMIREZ, J. D. HOLMES, & A. ROMANO-RODRIGUEZ. Synthesis and applications of one-dimensional semiconductors. *Progress in Materials Science* **55 (6)**, 563–627 (2010).

[215] C. C. STRIEMER, T. R. GABORSKI, J. L. MCGRATH, & P. M. FAUCHET. Charge- and size-based separation of macromolecules using ultrathin silicon membranes. *Nature* **445 (7129)**, 749–753 (2007).

[216] P. HONG, S. KOZA, & E. S. BOUVIER. A review size-exclusion chromatography for the analysis of protein biotherapeutics and their aggregates. *Journal of liquid chromatography & related technologies* **35 (20)**, 2923–2950 (2012).

[217] A. S. PRABHU, T. Z. N. JUBERY, K. J. FREEDMAN, R. MULERO, P. DUTTA, & M. J. KIM. Chemically modified solid state nanopores for high throughput nanoparticle separation. *Journal of Physics-Condensed Matter* **22 (45)** (2010).

[218] M. NAPOLI, P. ATZBERGER, & S. PENNATHUR. Experimental study of the separation behavior of nanoparticles in micro- and nanochannels. *Microfluidics and Nanofluidics* **10 (1)**, 69–80 (2011).

[219] R. WEI, V. GATTERDAM, R. WIENEKE, R. TAMPE, & U. RANT. Stochastic sensing of proteins with receptor-modified solid-state nanopores. *Nature Nanotechnology* **7 (4)** (2012).

[220] T. JOVANOVIC-TALISMAN, J. TETENBAUM-NOVATT, A. S. MCKENNEY, A. ZILMAN, R. PETERS, M. P. ROUT, & B. T. CHAIT. Artificial nanopores that mimic the transport selectivity of the nuclear pore complex. *Nature* **457 (7232)** (2009).

[221] N. SA, Y. FU, & L. A. BAKER. Reversible cobalt ion binding to imidazole-modified nanopipettes. *Analytical Chemistry* **82 (24)**, 9963–9966 (2010).

[222] K. Y. CHUN & P. STROEVE. Protein transport in nanoporous membranes modified with self-assembled monolayers of functionalized thiols. *Langmuir* **18 (12)**, 4653–4658 (2002).

[223] W. H. COULTER. Means for counting particles suspended in a fluid (1953).

[224] M. TSUTSUI, S. HONGO, Y. HE, M. TANIGUCHI, N. GEMMA, & T. KAWAI. Single-nanoparticle detection using a low-aspect-ratio pore. *ACS Nano* **6 (4)**, 3499–3505 (2012).

[225] S. F. BUCHSBAUM, N. MITCHELL, H. MARTIN, M. WIGGIN, A. MARZIALI, P. V. COVENEY, Z. SIWY, & S. HOWORKA. Disentangling steric and electrostatic factors in nanoscale transport through confined space. *Nano Letters* **13 (8)**, 3890–3896 (2013).

[226] G. R. WILLMOTT, R. VOGEL, S. S. C. YU, L. G. GROENEWEGEN, G. S. ROBERTS, D. KOZAK, W. ANDERSON, & M. TRAU. Use of tunable nanopore blockade rates to investigate colloidal dispersions. *Journal of Physics-Condensed Matter* **22 (45)** (2010).

[227] W. J. LAN, D. A. HOLDEN, J. LIU, & H. S. WHITE. Pressure-driven nanoparticle transport across glass membranes containing a conical-shaped nanopore. *Journal of Physical Chemistry C* **115 (38)**, 18445–18452 (2011).

[228] O. BECKSTEIN, K. TAI, & M. S. P. SANSOM. Not ions alone: Barriers to ion permeation in nanopores and channels. *Journal of the American Chemical Society* **126 (45)**, 14694–14695 (2004).

[229] R. B. SCHOCH & P. RENAUD. Ion transport through nanoslits dominated by the effective surface charge. *Applied Physics Letters* **86 (25)** (2005).

[230] C. Y. LEE, W. CHOI, J. H. HAN, & M. S. STRANO. Coherence resonance in a single-walled carbon nanotube ion channel. *Science* **329 (5997)**, 1320–1324 (2010).

[231] F. H. J. VAN DER HEYDEN, D. J. BONTHUIS, D. STEIN, C. MEYER, & C. DEKKER. Power generation by pressure-driven transport of ions in nanofluidic channels. *Nano Letters* **7 (4)**, 1022–1025 (2007).

[232] L. LIU, W. LEE, Z. HUANG, R. SCHOLZ, & U. GOSELE. Fabrication and characterization of a flow-through nanoporous gold nanowire/aao composite membrane. *Nanotechnology* **19 (33)** (2008).

[233] M. MAJUMDER, N. CHOPRA, R. ANDREWS, & B. J. HINDS. Nanoscale hydrodynamics - enhanced flow in carbon nanotubes. *Nature* **438 (7064)**, 44–44 (2005).

[234] M. Z. BAZANT, K. THORNTON, & A. AJDARI. Diffuse-charge dynamics in electrochemical systems. *Physical Review E* **70 (2)** (2004).

[235] A. HÖLTZEL & U. TALLAREK. Ionic conductance of nanopores in microscale analysis systems: Where microfluidics meets nanofluidics. *Journal of separation science* **30 (10)**, 1398–1419 (2007).

[236] B. R. SHRESTHA, T. BAIMPOS, S. RAMAN, & M. VALTINER. Angstrom-resolved real-time dissection of electrochemically active noble metal interfaces. *ACS Nano* **8 (6)**, 5979–5987 (2014).

[237] J. C. GIDDINGS. *Unified Separation Science*. John Wiley & Sons, Inc., New York (1991).

[238] D. GILLESPIE & S. PENNATHUR. Separation of ions in nanofluidic channels with combined pressure-driven and electro-osmotic flow. *Analytical Chemistry* **85 (5)**, 2991–2998 (2013).

[239] P. DUTTA & A. BESKOK. Analytical solution of combined eloectoossmotic/pressure driven flows in two-dimensional straight channels: Finite debye layer effects. *Analytical Chemistry* **73 (9)**, 1979–1986 (2001).

[240] S. W. ONG, X. L. ZHAO, & K. B. EISENTHAL. Polarization of water-molecules at a charged interface - 2nd harmonic studies of the silica water interface. *Chemical Physics Letters* **191 (3-4)**, 327–335 (1992).

[241] V. OSTROVERKHOV, G. A. WAYCHUNAS, & Y. R. SHEN. New information on water interfacial structure revealed by phase-sensitive surface spectroscopy. *Physical Review Letters* **94 (4)** (2005).

[242] K. Leung, I. M. B. Nielsen, & L. J. Criscenti. Elucidating the bimodal acid-base behavior of the water-silica interface from first principles. *Journal of the American Chemical Society* **131 (51)**, 18358–18365 (2009).

[243] A. T. Bell. The impact of nanoscience on heterogeneous catalysis. *Science* **299 (5613)**, 1688–1691 (2003).

[244] Q. B. Xu, B. D. Gates, & G. M. Whitesides. Fabrication of metal structures with nanometer-scale lateral dimensions by sectioning using a microtome. *Journal of the American Chemical Society* **126 (5)**, 1332–1333 (2004).

[245] Q. Xu, R. Perez-Castillejos, Z. Li, & G. M. Whitesides. Fabrication of high-aspect-ratio metallic nanostructures using nanoskiving. *Nano Letters* **6 (9)**, 2163–2165 (2006).

[246] D. J. Lipomi, F. Ilievski, B. J. Wiley, P. B. Deotare, M. Loncar, & G. M. Whitesides. Integrated fabrication and magnetic positioning of metallic and polymeric nanowires embedded in thin epoxy slabs. *ACS Nano* **3 (10)**, 3315–3325 (2009).

[247] Q. Xu, R. M. Rioux, & G. M. Whitesides. Fabrication of complex metallic nanostructures by nanoskiving. *ACS Nano* **1 (3)**, 215–227 (2007).

[248] K. Dawson, A. Wahl, R. Murphy, & A. O'Riordan. Electroanalysis at single gold nanowire electrodes. *Journal of Physical Chemistry C* **116 (27)**, 14665–14673 (2012).

[249] C. Xiang, Y. Yang, & R. M. Penner. Cheating the diffraction limit: electrodeposited nanowires patterned by photolithography. *Chemical Communications* **8**, 859–873 (2009).

[250] J. Kim, C.-Y. Lin, W. Xing, M. L. Mecartney, E. O. Potma, & R. M. Penner. Laser annealing of nanocrystalline gold nanowires. *Acs Applied Materials & Interfaces* **5 (15)**, 6808–6814 (2013).

[251] Y. Yang, S. C. Kung, D. K. Taggart, C. Xiang, F. Yang, M. A. Brown, A. G. Guell, T. J. Kruse, J. C. Hemminger, & R. M. Penner. Synthesis of pbte nanowire arrays using lithographically patterned nanowire electrodeposition. *Nano Letters* **8 (8)**, 2447–2451 (2008).

[252] C. Schonenberger, B. M. I. vanderZande, L. G. J. Fokkink, M. Henny, C. Schmid, M. Kruger, A. Bachtold, R. Huber, H. Birk, & U. Staufer. Template synthesis of nanowires in porous polycarbonate membranes: Electrochemistry and morphology. *Journal of Physical Chemistry B* **101 (28)**, 5497–5505 (1997).

[253] J. Gamby, J. P. Abid, M. Abid, J. P. Ansermet, & H. H. Girault. Nanowires network for biomolecular detection using contactless impedance tomoscopy technique. *Analytical Chemistry* **78 (15)**, 5289–5295 (2006).

[254] S. VALIZADEH, L. HULTMAN, J. M. GEORGE, & P. LEISNER. Template synthesis of au/co multilayered nanowires by electrochemical deposition. *Advanced Functional Materials* **12 (11-12)**, 766–772 (2002).

[255] L. SOLEIMANY, A. DOLATI, & M. GHORBANI. A study on the kinetics of gold nanowire electrodeposition in polycarbonate templates. *Journal of Electroanalytical Chemistry* **645 (1)**, 28–34 (2010).

[256] Y. LEPRINCE-WANG, A. YACOUBI-OUSLIM, & G. Y. WANG. Structure study of electrodeposited zno nanowires. *Microelectronics Journal* **36 (7)**, 625–628 (2005).

[257] F. KELLER, M. S. HUNTER, & D. L. ROBINSON. Structural features of oxide coatings on aluminium. *Journal of the Electrochemical Society* **100 (9)**, 411–419 (1953).

[258] H. MASUDA & K. FUKUDA. Ordered metal nanohole arrays made by a 2-step replication of honeycomb structures of anodic alumina. *Science* **268 (5216)**, 1466–1468 (1995).

[259] G. D. SULKA. *Highly Ordered Anodic Porous Alumina Formation by Self-Organized Anodizing*, book section 1, 1–116. WILEY-VCH, Weinheim (2008).

[260] D. ROUTKEVITCH, T. BIGIONI, M. MOSKOVITS, & J. M. XU. Electrochemical fabrication of cds nanowire arrays in porous anodic aluminum oxide templates. *Journal of Physical Chemistry* **100 (33)**, 14037–14047 (1996).

[261] X. ZHAO, S.-K. SEO, U.-J. LEE, & K.-H. LEEZ. Controlled electrochemical dissolution of anodic aluminum oxide for preparation of open-through pore structures. *Journal of the Electrochemical Society* **154 (10)**, C553–C557 (2007).

[262] G. Q. DING, M. J. ZHENG, W. L. XU, & W. Z. SHEN. Fabrication of controllable free-standing ultrathin porous alumina membranes. *Nanotechnology* **16 (8)**, 1285–1289 (2005).

[263] H. Y. JUNG, S. M. JUNG, G. H. GU, & J. S. SUH. Anodic aluminum oxide membrane bonded on a silicon wafer for carbon nanotube field emitter arrays. *Applied Physics Letters* **89 (1)** (2006).

[264] M. SHABAN, H. HAMDY, F. SHAHIN, J. PARK, & S.-W. RYU. Uniform and reproducible barrier layer removal of porous anodic alumina membrane. *Journal of Nanoscience and Nanotechnology* **10 (5)**, 3380–3384 (2010).

[265] O. RABIN, P. R. HERZ, Y. M. LIN, A. I. AKINWANDE, S. B. CRONIN, & M. S. DRESSELHAUS. Formation of thick porous anodic alumina films and nanowire arrays on silicon wafers and glass. *Advanced Functional Materials* **13 (8)**, 631–638 (2003).

[266] J. M. MOON & A. WEI. Uniform gold nanorod arrays from polyethylenimine-coated alumina templates. *Journal of Physical Chemistry B* **109 (49)**, 23336–23341 (2005).

[267] N. J. Gerein & J. A. Haber. Effect of ac electrodeposition conditions on the growth of high aspect ratio copper nanowires in porous aluminum oxide templates. *Journal of Physical Chemistry B* **109 (37)**, 17372–17385 (2005).

[268] A. Jagminiene, G. Valincius, A. Riaukaite, & A. Jagminas. The influence of the alumina barrier-layer thickness on the subsequent ac growth of copper nanowires. *Journal of Crystal Growth* **274 (3-4)**, 622–631 (2005).

[269] L. Zhang & E. T. Samulski. In-situ electrochemical synthesis of 1-d alumina nanostructures. *Abstracts of Papers of the American Chemical Society* **230**, U2044–U2044 (2005).

[270] C. T. Sousa, D. C. Leitao, M. P. Proenca, A. Apolinario, J. G. Correia, J. Ventura, & J. P. Araujo. Tunning pore filling of anodic alumina templates by accurate control of the bottom barrier layer thickness. *Nanotechnology* **22 (31)** (2011).

[271] J. Burdick, E. Alonas, H.-C. Huang, K. Rege, & J. Wang. High-throughput templated multisegment synthesis of gold nanowires and nanorods. *Nanotechnology* **20 (6)** (2009).

[272] R. M. Hernandez, L. Richter, S. Semancik, S. Stranick, & T. E. Mallouk. Template fabrication of protein-functionalized gold-polypyrrole-gold segmented nanowires. *Chemistry of Materials* **16 (18)**, 3431–3438 (2004).

[273] H. S. Virk, K. Kishore, & V. Balouria. Fabrication of copper nanowires by electrodeposition using anodic alumina and polymer templates. *Journal of Nano Research* **10**, 63–67 (2010).

[274] M. L. Tian, S. Y. Xu, J. G. Wang, N. Kumar, E. Wertz, Q. Li, P. M. Campbell, M. H. W. Chan, & T. E. Mallouk. Penetrating the oxide barrier in situ and separating freestanding porous anodic alumina films in one step. *Nano Letters* **5 (4)**, 697–703 (2005).

[275] P. Evans, W. R. Hendren, R. Atkinson, G. A. Wurtz, W. Dickson, A. V. Zayats, & R. J. Pollard. Growth and properties of gold and nickel nanorods in thin film alumina. *Nanotechnology* **17 (23)**, 5746–5753 (2006).

[276] M. J. Banholzer, L. Qin, J. E. Millstone, K. D. Osberg, & C. A. Mirkin. On-wire lithography: synthesis, encoding and biological applications. *Nature Protocols* **4 (6)**, 838–848 (2009).

[277] J. Silverberg, S. Saha, D. O'Malley, & L. Menon. Development of au nanowires for recording electrical activity in neural cells. In *Symposium E Nanofunctional Materials, Nanostructures and Novel Devices for Biological and Chemical Detection*, volume 951 of *MRS Online Proceedings Library* (1 2006).

[278] M. J. TIERNEY & C. R. MARTIN. Transparent metal microstructures. *Journal of Physical Chemistry* **93 (8)**, 2878–2880 (1989).

[279] Z. WANG, Y. K. SU, & H. L. LI. Afm study of gold nanowire array electrodeposited within anodic aluminum oxide template. *Applied Physics a-Materials Science & Processing* **74 (4)**, 563–565 (2002).